Diagrammatic Monte Carlo study of polaron systems

Jonas Vlietinck

Promotoren: Prof. Dr. Kris Van Houcke
Prof. Dr. Jan Ryckebusch

Proefschrift ingediend tot het behalen van de academische graad van
Doctor in de Wetenschappen: Fysica

Universiteit Gent
Faculteit Wetenschappen
Vakgroep Fysica en Sterrenkunde
Academiejaar 2014-2015

Contents

CHAPTER 1

Introduction

1.1 The Fermi gas as a model for strongly interacting Fermi systems

The simplest quantum many-body systems that one can imagine are the free Bose and Fermi gas. Their thermodynamic quantities can easily be calculated within the framework of statistical physics. If the particles of the many-body system are weakly interacting one typically relies on perturbation theory to calculate the properties. In many realistic systems, however, the interaction between the particles is far from weak and perturbation-theory calculations mostly fail. This failure can be illustrated by considering the perturbation series for the energy of an electron gas in a metal. Consider the following Hamiltonian:

$$\hat{H} = \sum_{i=1}^{N} \frac{\hat{\mathbf{p}}_i^2}{2m} + \frac{e^2}{4\pi\varepsilon_0}\frac{1}{2}\sum_{\substack{i,j=1 \\ (i\neq j)}}^{N} \frac{1}{\|\hat{\mathbf{r}}_i - \hat{\mathbf{r}}_j\|} \,, \tag{1.1}$$

with ε_0 the vacuum permittivity, e the electron charge, m the electron mass, $\hat{\mathbf{r}}_i$ the position operator and $\hat{\mathbf{p}}_i$ the momentum operator for the i-th electron. We neglect three-particle interactions and assume that there are no external forces present. Upon calculating the ground-state energy E_0 of this system with the Coulomb interaction as a perturbation, we get:

$$E_0 = E_0^{(0)} + E_0^{(1)} + \infty + \infty + \dots \,. \tag{1.2}$$

Calculating higher orders in perturbation theory gives divergences and perturbation theory seems to fail in this case [1].

Some strongly interacting systems can be described by Landau Fermi liquid theory [2]. The theory constructs a model for the energies of the weakly excited states of the system.

Landau argued that numerous many-body systems of strongly interacting particles can be mapped onto a system of weakly interacting elementary excitations above the ground state [3](for example particle-hole excitations). Consider a Hamiltonian which is the sum of a one-body operator $\hat{T}$ and a two-body interaction operator $\hat{V}$. In standard second quantisation notation, the Hamiltonian is written as (see, e.g., Ref. [4])

$$\begin{aligned}\hat{H} &= \hat{T} + \hat{V} \\ &= \sum_{\alpha,\beta} \langle \alpha|T|\beta\rangle \hat{c}^\dagger_\alpha \hat{c}_\beta + \frac{1}{2}\sum_{\alpha\beta\rho\nu} \langle \alpha\beta|V|\nu\rho\rangle \hat{c}^\dagger_\alpha \hat{c}^\dagger_\beta \hat{c}_\rho \hat{c}_\nu \ .\end{aligned} \tag{1.3}$$

The operators $\hat{c}^\dagger_\alpha$ and $\hat{c}_\alpha$ denote the creation and annihilation of a fermion in the quantum single-particle state $|\alpha\rangle$ characterised by the quantum number(s) α. The Hamiltonian $\hat{H}$ in Eq. (1.3) describes a system of strongly 'real' interacting particles, that usually cannot be solved by perturbation theory. In most many-body systems it turns out that a canonical transformation (with canonical we mean that the commutation relations are preserved) can be used to transform $\hat{H}$ into a Hamiltonian of the following form:

$$\hat{H} = E_0 + \sum_\gamma \epsilon'_\gamma \hat{a}^\dagger_\gamma \hat{a}_\gamma + f(\ldots \hat{a}_\gamma \ldots \hat{a}^\dagger_\gamma \ldots) \ , \tag{1.4}$$

now written in terms of weakly interacting 'fictitious' particles or elementary excitations [1]. The operators $\hat{a}^\dagger_\gamma$ and $\hat{a}_\gamma$ denote the creation and annihilation for these elementary excitations characterised by the quantum number γ above a ground-state energy E_0. The term $f(\ldots \hat{a}_\gamma \ldots \hat{a}^\dagger_\gamma \ldots)$ describes the interactions between elementary excitations and is assumed to be small. The dispersion of the elementary excitations is given by ϵ'_γ. These excitations are the result of collective interactions in the system and give important information about the macroscopic behavior of the system. The residual interaction term $f(\ldots \hat{a}_\gamma \ldots \hat{a}^\dagger_\gamma \ldots)$ will give rise to a broadening $\Delta\epsilon'_\gamma$ of the energy levels ϵ'_γ. By the uncertainty principle we know that the elementary excitations will have a lifetime $\tau_\gamma \sim \hbar(\Delta\epsilon'_\gamma)^{-1}$. In the Landau Fermi liquid theory the decay rate of these excitations should be much less than their energy, or $\Delta\epsilon'_\gamma \ll \epsilon'_\gamma$. For $f(\ldots \hat{a}_\gamma \ldots \hat{a}^\dagger_\gamma \ldots) \to 0$ the elementary excitations have a well-defined energy and correspondingly an infinite lifetime. It should be noticed that the properties of these elementary excitations can be totally different from those of the 'real' particles.

We illustrate the ideas of Landau Fermi liquid theory with two examples. The first example deals with electrons in a metal at a temperature $T \ll T_F$, with T_F the Fermi temperature. For a large class of metals the elementary excitations are particle-hole excitations. The question arises whether the particle-hole excitations will be long-lived and have a narrow width in energy. Landau realized that there is only a small phase space for scattering of an electron just above the Fermi sea (FS) with an electron in the sea. This is a direct consequence of the Pauli exclusion principle and leads to long-lived particle-hole excitations if we consider scattering close to the Fermi surface. An electron above the Fermi sea can thus be described as a free electron dressed with particle-hole excitations. These ideas show that electrons in a metal often can be seen as freely moving particles. This free electron model has also been verified experimentally in metals. The average distance between conduction

electrons in metals is about 2Å. The mean free paths are however longer than 10^4 Å at room temperature and longer than 10 cm at 1K [5].

As a second example of a Landau Fermi liquid we consider an interacting Fermi gas at $T = 0$ composed out of spin-up fermions and spin-down fermions. An attractive interaction is considered, acting only between spin-up and spin-down fermions. The concentration of $\downarrow$ atoms is assumed to be small, so that the ratio of densities $x = n_\downarrow/n_\uparrow \ll 1$, with $n_\downarrow$ ($n_\uparrow$) the density of spin-down (spin-up) particles. A Fermi liquid model can be constructed and the energy of the system becomes approximately [6, 7]:

$$\frac{E(x)}{N_\uparrow} = \frac{3}{5}\epsilon_F \left(1 - Ax + \frac{m}{m_*}x^{5/3}\right) , \tag{1.5}$$

with ϵ_F the Fermi energy of the spin-up Fermi sea. The parameter A is related to the binding energy of one spin-down atom to the Fermi gas of spin-up atoms and m_* is the effective mass of one spin-down impurity (quasiparticle). To find the parameters A and m_* we need to solve the problem of one spin-down fermion interacting with a spin-up sea. We will discuss the Hamiltonian of this impurity system in more detail in Sec. 1.3.2.

1.2 The polaron: an impurity moving through a medium

In the last section we mentioned the problem of a single spin-down particle in a spin-up Fermi sea. The problem of an impurity moving through a medium of identical particles has been studied for decades. One of the first examples of the impurity system was studied by Landau in 1933: an electron in an ionic lattice. Landau realized that an electron, by its Coulomb interaction with the ions of the lattice, produces a polarization. The electron could be seen as a rigid charge moving through the lattice carrying its polarization potential with it, and hence Landau called it a polaron. In the case the lattice-deformation size (caused by the electron) is larger than the lattice parameter, the lattice can be treated as a continuum. In 1952, Fröhlich derived a Hamiltonian $\hat{H}_{pol}$ for such a system [8]:

$$\hat{H}_{pol} = \underbrace{\sum_{\mathbf{k}} \frac{\hbar^2\mathbf{k}^2}{2m}\hat{c}^\dagger_{\mathbf{k}}\hat{c}_{\mathbf{k}}}_{\hat{H}^I_{pol}} + \underbrace{\sum_{\mathbf{q}} \hbar\omega(\mathbf{q})\hat{b}^\dagger_{\mathbf{q}}\hat{b}_{\mathbf{q}}}_{\hat{H}^B_{pol}} + \underbrace{\sum_{\mathbf{k},\mathbf{q}} V(\mathbf{q})\hat{c}^\dagger_{\mathbf{k}+\mathbf{q}}\hat{c}_{\mathbf{k}}\left(\hat{b}^\dagger_{-\mathbf{q}} + \hat{b}_{\mathbf{q}}\right)}_{\hat{H}^{IB}_{pol}} . \tag{1.6}$$

Here, the $\hat{c}^\dagger_{\mathbf{k}}$ ($\hat{c}_{\mathbf{k}}$) are the creation (annihilation) operators of the electron with mass m and wave vector $\mathbf{k}$. The kinetic energy of the electron is represented by the term $\hat{H}^I_{pol}$ and $\hat{H}^B_{pol}$ gives the energy of the phonons which carry the polarization. Thereby, the operator $\hat{b}^\dagger_{\mathbf{q}}$ ($\hat{b}_{\mathbf{q}}$) creates (annihilates) a phonon with wave vector $\mathbf{q}$ and energy $\hbar\omega(\mathbf{q})$. The term $\hat{H}^{IB}_{pol}$ denotes the interaction between the charge carrier and the phonons with interaction strength $V(\mathbf{q})$. In the remainder of this work we take $\hbar = 1$. A plethora of physical phenomena can be described by the above Fröhlich type of Hamiltonian by varying the dispersion $\omega(\mathbf{q})$ and the interaction strength $V(\mathbf{q})$, see for example [9]. Despite the importance of polarons in semiconductor physics and in other branches of physics, studying polarons in solids has some

limitations. For example, the interaction strength will depend on the type of material and exploring strongly interacting regimes can be difficult. The realization of a crystal at $T = 0$ poses also difficulties and the transformation of such a crystal to a gas of non-interacting phonons is also an idealization of reality. One could include an interaction term for the phonons, yet the price we pay is a more complicated model that is difficult to solve. In the next section, a more controllable and clean medium will be presented which will allow us to make a better mapping for this experimental system on a theoretical polaron model.

1.3 Polarons in ultracold gases

Since the first experimental realization of Bose Einstein condensation (BEC) in 1995 [10–12], ultracold gases have become very important in the study of quantum many-body physics. Within the last decade, fundamental phenomena like coherence, superfluidity, quantum phase transitions, ... were studied in these systems. It was soon realized that ultracold gases offer a unique test system that could be used as a quantum simulator of strongly interacting many-body physics [13]. For example, an impurity immersed in a BEC (the BEC polaron) can be represented, under certain conditions (see Sec. 1.3.3), by a Hamiltonian which has the same structure as $\hat{H}_{pol}$.

In ultracold gases we have the ability to tune the s-wave scattering length to arbitrary values by means of Feshbach resonances [14], which offers the possibility to study weakly and strongly interacting systems. Consider for example the case of a two-component Fermi gas (with spin-down and spin-up fermions). If we start from a weakly interacting Fermi gas and increase the attraction between the fermions we will end up with a gas of bosonic molecules that form a BEC at sufficiently low temperature. What happens is the so-called BEC-BCS crossover [15], which smoothly converts a gas of fermions into a gas of bosons. The extremely imbalanced case with one spin-down fermion and N spin-up fermions is called the Fermi polaron [16].

Before we start discussing polaron systems in ultracold gases, we will first take a brief look at two-body scattering at low energy in Sec. 1.3.1. In Sec. 1.3.2 the Fermi polaron Hamiltonian in three dimensions (3D) will be introduced and in Sec. 1.3.3 we will set up a Hamiltonian for the 3D BEC polaron.

1.3.1 Two-body scattering at low energies

Since we are dealing with dilute gases, the following relation between the interaction range R of the potential and the density ρ is valid:

$$R\rho^{1/3} \ll 1 \,. \tag{1.7}$$

This means that the average distance between two particles is much larger than the range of the interaction, which allows us to restrict ourselves to binary scattering.

We consider an ultracold collision that involves two distinguishable particles in the center-of-mass (c.m.) frame. The relative wave function in 3D at a distance r far beyond the

interatomic potential is given by:

$$\psi = e^{ikz} + f(k,\theta)\frac{e^{ikr}}{r} \ , \tag{1.8}$$

where e^{ikz} represents the incoming plane wave with wave vector k along the z-axis. We assume the interaction between the atoms to be spherically symmetric. The scattering amplitude can be written as an expansion in partial waves:

$$f(k,\theta) = \sum_{l=0}^{\infty} f_l(k,\theta) = \frac{1}{2ik}\sum_{l=0}^{\infty}(2l+1)(e^{i2\delta_l}-1)P_l(\cos\theta) \ , \tag{1.9}$$

with δ_l the phase shift of the scattered wave and $P_l(\cos\theta)$ the Legendre polynomials. Since we are interested in scattering at low momenta, s-wave ($l = 0$) scattering will be dominant over all other partial waves. So, the scattering amplitude becomes [17]:

$$f(k,\theta) \approx f_0(k,\theta) = \frac{1}{2ik}(e^{2i\delta_s}-1) = \frac{1}{k\cot\delta_s - ik} \ . \tag{1.10}$$

In this expression $k\cot\delta_s$ can be further expanded:

$$k\cot\delta_s \approx -\frac{1}{a_s} + \frac{r_{\text{eff}}}{2}k^2 + \dots \ , \tag{1.11}$$

where a_s is the s-wave scattering length and r_{eff} the effective range of the interaction potential. The "..." represent higher order terms in k^2. Since we consider low-energy scattering in a dilute gas, we can write that $R \ll \lambda$, with λ the de Broglie wavelength. This means that the fine details of the potential are not required and any potential that reproduces the desired set of scattering parameters $(a, r_{\text{eff}}, \dots)$ is a good one. This 'fictitious' potential is also called an effective potential. Of course we want to choose a potential that makes our calculations as simple as possible. An obvious candidate is given by $V(\mathbf{r}) = g_0\delta(\mathbf{r})$, with g_0 the coupling constant. We regularise the Dirac-delta interaction potential by putting the particles on a lattice. The following relation between g_0 and a_s can be obtained [18]:

$$\frac{1}{g_0} = \frac{m}{4\pi a_s} - \frac{1}{(2\pi)^3}\int_{\mathcal{B}} d\mathbf{q}\frac{m}{q^2} \ , \tag{1.12}$$

where the integral is over the first Brillouin zone $\mathcal{B} =]-\pi/b, \pi/b]^3$ of the reciprocal lattice, with b the lattice spacing. In Sec. 2.3 the continuum limit will be taken ($b \to 0$ and $g_0 \to 0^-$).

In two dimensions (2D) we wish to write a relation between the bare coupling constant g_0 and the two-body binding energy ε_B in vacuum. Such a bound state always exists in two dimensions, as long as the interaction potential is attractive. The relation between ε_B and g_0 can be established by considering the bound state $|\psi_{\mathbf{p}}\rangle$:

$$|\psi_{\mathbf{p}}\rangle = \sum_{\mathbf{q}} \phi_{\mathbf{q}}|\mathbf{p}-\mathbf{q},\mathbf{q}\rangle \ , \tag{1.13}$$

with $\mathbf{p}-\mathbf{q}$ and $\mathbf{q}$ the momenta of the non-identical particles and $\phi_{\mathbf{q}}$ the Fourier representation of the wave function for the relative motion of the two bound particles. Let us denote the

two particles by spin-↑ and spin-↓. The Hamiltonian reads:

$$\hat{H} = \sum_{\mathbf{q}\in\mathcal{B},\sigma=\uparrow\downarrow} \epsilon_{\mathbf{q}\sigma}\hat{c}^\dagger_{\mathbf{q}\sigma}\hat{c}_{\mathbf{q}\sigma} + \frac{g_0}{\mathcal{V}} \sum_{\mathbf{p},\mathbf{q},\mathbf{q}'\in\mathcal{B}} \hat{c}^\dagger_{\mathbf{p}-\mathbf{q}\uparrow}\hat{c}^\dagger_{\mathbf{q}'+\mathbf{q}\downarrow}\hat{c}_{\mathbf{q}'\downarrow}\hat{c}_{\mathbf{p}\uparrow} \,, \tag{1.14}$$

with the dispersion $\epsilon_{\mathbf{q}\sigma} = \frac{\mathbf{q}^2}{2m_\sigma}$ and m_σ the mass of the spin-σ fermion, and $\mathcal{V}$ the area of the system. (In Sec. 3.1 the thermodynamic limit, $\mathcal{V}\to\infty$ will be taken). Wave vectors are summed over the first Brillouin zone $\mathcal{B} =]-\pi/b, \pi/b]^2$ in two dimensions. The operators $\hat{c}^\dagger_{\mathbf{q}\sigma}$ ($\hat{c}_{\mathbf{q}\sigma}$) create (annihilate) particles with momentum $\mathbf{q}$ and spin σ. The energy of the state $|\psi_\mathbf{p}\rangle$ is given by

$$\langle\psi_\mathbf{p}|\hat{H}|\psi_\mathbf{p}\rangle = \sum_{\mathbf{q}\in\mathcal{B}} |\phi_\mathbf{q}|^2(\epsilon_{\mathbf{q}\downarrow} + \epsilon_{\mathbf{p}-\mathbf{q}\uparrow}) + \frac{g_0}{\mathcal{V}} \sum_{\mathbf{q},\mathbf{q}'\in\mathcal{B}} \phi_\mathbf{q}\phi^*_{\mathbf{q}'} \,, \tag{1.15}$$

To minimize $\langle\psi_\mathbf{p}|\hat{H}|\psi_\mathbf{p}\rangle$ with the constraint $\langle\psi_\mathbf{p}|\psi_\mathbf{p}\rangle = 1$ we consider the function Λ:

$$\Lambda = \langle\psi_\mathbf{p}|\hat{H}|\psi_\mathbf{p}\rangle - \varepsilon_B \left(\sum_{\mathbf{q}\in\mathcal{B}} |\phi_\mathbf{q}|^2 - 1 \right) \,, \tag{1.16}$$

where ε_B can also be interpreted as the Lagrange multiplier associated to the normalization of $|\psi_\mathbf{p}\rangle$. The minimization of Λ with respect to $\phi_\mathbf{q}$ gives:

$$\begin{aligned} \frac{\partial\Lambda}{\partial\phi_\mathbf{q}} &= 0 \,, \\ (\epsilon_{\mathbf{q}\downarrow} + \epsilon_{\mathbf{p}-\mathbf{q}\uparrow})\,\phi_\mathbf{q} + \frac{g_0}{\mathcal{V}} \sum_{\mathbf{q}'\in\mathcal{B}} \phi_{\mathbf{q}'} &= \varepsilon_B\phi_\mathbf{q} \,, \end{aligned} \tag{1.17}$$

$$\phi_\mathbf{q} = -\frac{g_0}{\mathcal{V}} \frac{\sum\limits_{\mathbf{q}'\in\mathcal{B}} \phi_{\mathbf{q}'}}{\epsilon_{\mathbf{p}-\mathbf{q}\uparrow} + \epsilon_{\mathbf{q}\downarrow} - \varepsilon_B} \,. \tag{1.18}$$

From Eq. (1.18) if follows that for large $|\mathbf{q}|$ the following relation holds

$$\phi_\mathbf{q} \propto \frac{1}{q^2} \,. \tag{1.19}$$

By applying the summation $\sum_\mathbf{q}$ on both sides of Eq. (1.18) and taking the c.m. momentum $\mathbf{p} = \mathbf{0}$, we get a relation between g_0 and ε_B:

$$\frac{-1}{g_0} = \frac{1}{\mathcal{V}} \sum_{\mathbf{q}\in\mathcal{B}} \frac{1}{\epsilon_{\mathbf{q}\uparrow} + \epsilon_{\mathbf{q}\downarrow} - \varepsilon_B} \,. \tag{1.20}$$

1.3.2 The Fermi polaron Hamiltonian

Before we set up a Hamiltonian for the Fermi polaron we first take at look at the interactions among the spin-up fermions and the interaction between the spin-down fermion (the impurity) and the spin-up sea. The scattering of two indentical spin-up fermions in the c.m. frame at distances larger than the range of the interatomic potential is determined

by the antisymmetrized form of the wave function of Eq. (1.8). The interchange of two particle coordinates corresponds to changing the sign of the relative coordinate $\mathbf{r} \to -\mathbf{r}$, or, in spherical coordinates, $r \to r$, $\phi \to \phi + \pi$, $\theta \to \pi - \theta$ and the antisymmetrized wave function is [19]:

$$\psi = e^{ikz} - e^{-ikz} + [f(\theta) - f(\pi - \theta)] \frac{e^{ikr}}{r} . \tag{1.21}$$

The differential cross section is given by

$$\frac{d\sigma}{d\Omega} = |f(\theta) - f(\pi - \theta)|^2 , \tag{1.22}$$

with σ the cross section and Ω the solid angle. For s-wave scattering there is no θ dependence in $f(\theta)$ (see Eq. (1.10)) and consequently the cross section vanishes for fermions in the same state. As shown in Ref. [20] p-wave scattering is strongly suppressed if we consider low-energy scattering and therefore scattering between identical fermions will be neglected. The matrix element of the interaction between the impurity and a spin-up fermion in position space is denoted by $V_{\downarrow\uparrow}(\mathbf{r} - \mathbf{r}')$.

The Hamiltonian $\hat{H}_{FP}$ of the Fermi polaron is

$$\hat{H}_{FP} = \hat{H}_0 + \hat{H}_{\downarrow\uparrow} , \tag{1.23}$$

with

$$\hat{H}_0 = \sum_{\mathbf{k},\sigma=\uparrow\downarrow} \epsilon_{\mathbf{k}\sigma}\ \hat{c}^\dagger_{\mathbf{k}\sigma}\hat{c}_{\mathbf{k}\sigma} , \tag{1.24}$$

$$\hat{H}_{\downarrow\uparrow} = \frac{1}{\mathcal{V}} \sum_{\mathbf{k},\mathbf{k}',\mathbf{q}} V_{\downarrow\uparrow}(\mathbf{q}) \hat{c}^\dagger_{\mathbf{k}+\mathbf{q}\uparrow}\hat{c}^\dagger_{\mathbf{k}'-\mathbf{q}\downarrow}\hat{c}_{\mathbf{k}'\downarrow}\hat{c}_{\mathbf{k}\uparrow} . \tag{1.25}$$

The operators $\hat{c}^\dagger_{\mathbf{k}\sigma}$ ($\hat{c}_{\mathbf{k}\sigma}$) create (annihilate) fermions with momentum $\mathbf{k}$ and spin σ. The volume is denoted by $\mathcal{V}$. The spin-σ fermions have mass m_σ and dispersion $\epsilon_{\mathbf{k}\sigma} = k^2/2m_\sigma$. For the interaction between the spin-down impurity and a spin-up fermion we adopt a Dirac delta potential, $V_{\downarrow\uparrow}(\mathbf{r} - \mathbf{r}') = g_0\delta(\mathbf{r} - \mathbf{r}')$ with g_0 the coupling constant, and in momentum space $V_{\downarrow\uparrow}(\mathbf{k}) = g_0$. To regularise the ultraviolet divergences that appear because of this choice, we will put the fermions again on the lattice, which naturally truncates the momentum integration.

1.3.3 The BEC polaron Hamiltonian

The following Hamiltonian can be used to describe an impurity in a bath of interacting bosonic particles:

$$\begin{aligned}\hat{H} = &\sum_{\mathbf{p}} \frac{p^2}{2m_I}\hat{c}^\dagger_{\mathbf{p}}\hat{c}_{\mathbf{p}} + \sum_{\mathbf{k}} \epsilon_{\mathbf{k}}\hat{a}^\dagger_{\mathbf{k}}\hat{a}_{\mathbf{k}} + \frac{1}{2\mathcal{V}} \sum_{\mathbf{k},\mathbf{k}',\mathbf{q}} V_{BB}(\mathbf{q})\hat{a}^\dagger_{\mathbf{k}'-\mathbf{q}}\hat{a}^\dagger_{\mathbf{k}+\mathbf{q}}\hat{a}_{\mathbf{k}}\hat{a}_{\mathbf{k}'} \\ &+ \frac{1}{\mathcal{V}} \sum_{\mathbf{k},\mathbf{k}',\mathbf{q}} V_{IB}(\mathbf{q})\hat{c}^\dagger_{\mathbf{k}+\mathbf{q}}\hat{c}_{\mathbf{k}}\hat{a}^\dagger_{\mathbf{k}'-\mathbf{q}}\hat{a}_{\mathbf{k}'} ,\end{aligned} \tag{1.26}$$

with the dispersion given by $\epsilon_{\mathbf{k}} = k^2/2m_B$, and $\mathcal{V}$ the volume of the system. The operators $\hat{a}^\dagger_{\mathbf{k}}(\hat{a}_{\mathbf{k}})$ create (annihilate) bosons with momentum $\mathbf{k}$ and mass m_B. The operators $\hat{c}^\dagger_{\mathbf{p}}(\hat{c}_{\mathbf{p}})$ create (annihilate) the impurity with momentum $\mathbf{p}$ and mass m_I. The interaction potential in momentum space between bosons of the bath is given by $V_{BB}(\mathbf{q})$, and $V_{IB}(\mathbf{q})$ represents the interaction potential of the impurity with a boson of the bath. At sufficiently low temperatures the bosons will form a Bose-Einstein condensate. If $N - N_0 \ll N_0$ is valid, with N_0 the number of bosons in the condensate and $N = \langle \hat{N} \rangle$ the average total particle number, the Bogoliubov approximation can be applied [4, 21]:

$$\hat{a}^\dagger_0 \approx \hat{a}_0 \approx \sqrt{N_0}\,, \tag{1.27}$$

and the operators can be treated as real numbers. As a consequence the Hamiltonian $\hat{H}$ will no longer conserve particle number. The number operator $\hat{N}$ is given by:

$$\hat{N} = N_0 + \sum_{|\mathbf{k}|\neq 0} \hat{a}^\dagger_{\mathbf{k}} \hat{a}_{\mathbf{k}}\,. \tag{1.28}$$

By applying the Bogoliubov approximation on Eq. (1.26), we get :

$$\begin{aligned}
\hat{H} \approx & \sum_{\mathbf{p}} \frac{p^2}{2m_I} \hat{c}^\dagger_{\mathbf{p}} \hat{c}_{\mathbf{p}} + \frac{N_0}{\mathcal{V}} V_{IB}(0) + \frac{1}{2\mathcal{V}} N_0^2 V_{BB}(0) + \sum_{|\mathbf{k}|\neq 0} \epsilon_{\mathbf{k}} \hat{a}^\dagger_{\mathbf{k}} \hat{a}_{\mathbf{k}} \\
& + \frac{N_0}{2\mathcal{V}} \sum_{|\mathbf{k}|\neq 0} V_{BB}(\mathbf{k}) (\hat{a}^\dagger_{\mathbf{k}} \hat{a}^\dagger_{-\mathbf{k}} + \hat{a}_{\mathbf{k}} \hat{a}_{-\mathbf{k}}) + 2 \frac{N_0}{\mathcal{V}} \sum_{|\mathbf{k}|\neq 0} V_{BB}(\mathbf{k}) \hat{a}^\dagger_{\mathbf{k}} \hat{a}_{\mathbf{k}} \\
& + \frac{\sqrt{N_0}}{\mathcal{V}} \sum_{|\mathbf{k}|\neq 0, \mathbf{p}} V_{IB}(\mathbf{k}) \hat{c}^\dagger_{\mathbf{p}+\mathbf{k}} \hat{c}_{\mathbf{p}} (\hat{a}^\dagger_{-\mathbf{k}} + \hat{a}_{\mathbf{k}}) \\
:= & \hat{H}_{BP}\,.
\end{aligned} \tag{1.29}$$

We ignore terms with more than three non-condensate operators, which is a good approximation if $N - N_0 \ll N_0$.

We replace the actual interaction potentials with pseudo-potentials, $V_{IB}(\mathbf{k}) = g_{IB}$ and $V_{BB}(\mathbf{k}) = g_{BB}$. The momentum independent matrix elements g_{IB} and g_{BB} can again be chosen such that the two-body scattering properties in vacuum are correctly reproduced. Like in Sec. 1.3.1, we have a relation between g_{BB} and the boson-boson scattering length a_{BB} (and a similar relation for g_{IB} and the impurity-boson scattering length a_{IB}):

$$\frac{4\pi a_{BB}}{m_B} = g_{BB} - m_B g_{BB}^2 \int \frac{d\mathbf{q}}{(2\pi)^3} \frac{1}{q^2} + \dots\,. \tag{1.30}$$

We keep only the first-order Born result:

$$g_{BB} = \frac{4\pi a_{BB}}{m_B}\,. \tag{1.31}$$

Similarly, we have

$$g_{IB} = \frac{2\pi a_{IB}}{m_r}\,, \tag{1.32}$$

with the reduced mass $m_r = \frac{m_I m_B}{m_I + m_B}$. The second order contribution in Eq. (1.30) diverges for high momenta. This divergence stems from our particular choice with regard to the momentum dependence of the pseudo-potential. To regularise this ultraviolet divergence we introduce a global momentum cut-off in the sums (or integrals) over momenta. We will see in Sec. 4.3 that the divergence of the second order Born term cancels with another divergence which appears in the ground-state energy of the interacting Bose gas.

A canonical transformation can be applied to Eq. (1.29) (see appendix A for the derivation), which leads to a Fröhlich type of Hamiltonian:

$$\begin{aligned}\hat{H}_{BP} =& E_0 + n_0 g_{IB} + \sum_{\mathbf{p}} \frac{p^2}{2m_I}\, \hat{c}^\dagger_{\mathbf{p}} \hat{c}_{\mathbf{p}} + \sum_{|\mathbf{k}|\neq 0} \omega(\mathbf{k}) \hat{b}^\dagger_{\mathbf{k}} \hat{b}_{\mathbf{k}} \\ &+ \sum_{|\mathbf{k}|\neq 0, \mathbf{p}} V_{BP}(\mathbf{k})\, \hat{c}^\dagger_{\mathbf{p}+\mathbf{k}} \hat{c}_{\mathbf{p}} \big(\hat{b}^\dagger_{-\mathbf{k}} + \hat{b}_{\mathbf{k}}\big)\ .\end{aligned} \tag{1.33}$$

The creation (annihilation) operator $\hat{b}^\dagger_{\mathbf{k}}$ ($\hat{b}_{\mathbf{k}}$) represent now the creation (annihilation) of a Bogoliubov excitation. The quasiparticle vacuum energy is

$$E_0 = \frac{\mathcal{V}}{2} n^2 g_{BB} + \frac{1}{2} \sum_{\mathbf{k}} \left(\omega(\mathbf{k}) - \epsilon_{\mathbf{k}} - n_0 g_{BB}\right)\ , \tag{1.34}$$

with the dispersion relation $\omega(\mathbf{k})$ given by

$$\omega(\mathbf{k}) = ck \sqrt{1 + \frac{(\xi \mathbf{k})^2}{2}}\ , \tag{1.35}$$

the healing length of the condensate $\xi = \frac{1}{\sqrt{8\pi n_0 a_{BB}}}$, the speed of sound in the condensate $c = \frac{\sqrt{4\pi n_0 a_{BB}}}{m_B}$ and the density of the condensed bosons $n_0 = N_0/\mathcal{V}$ and the average total density $n = \langle \hat{N} \rangle / \mathcal{V}$. The interaction matrix element $V_{BP}(\mathbf{k})$ between a Bogoliubov excitation and the impurity is given by

$$V_{BP}(\mathbf{k}) = \frac{\sqrt{N_0} g_{IB}}{\mathcal{V}} \left(\frac{(\xi \mathbf{k})^2}{(\xi \mathbf{k})^2 + 2} \right)^{1/4}\ . \tag{1.36}$$

CHAPTER 2

The Fermi polaron and its Green's function

To calculate the properties of the Fermi polaron, we will use the Green's function formalism (see for example [3, 4, 21]). From the knowledge of the Green's function all relevant properties can be extracted. We will calculate the Green's function of the Fermi polaron by means of a Feynman-Dyson series expansion. The terms in this series can be identified with Feynman diagrams. We will argue that the diagrammatic Monte Carlo (DiagMC) method, an importance sampling Monte Carlo (MC) method, is a very powerful method to sample over a large number of diagrams. This technique will allow us to evaluate the Green's function to a high precision.

2.1 The Green's function and the Feynman-Dyson perturbation series

The polaron's quasiparticle properties can be extracted from the impurity's Green's function defined as

$$G_\downarrow(\mathbf{p},\tau) = -\theta(\tau)\langle\Phi_0^{N_\uparrow}|\hat{c}_{\mathbf{p}\downarrow}(\tau)\hat{c}^\dagger_{\mathbf{p}\downarrow}(0)\ |\Phi_0^{N_\uparrow}\rangle\ , \tag{2.1}$$

with $\hat{c}_{\mathbf{p}\downarrow}(\tau)$ the annihilation operator of the 'spin-$\downarrow$' impurity in the Heisenberg picture,

$$\hat{c}_{\mathbf{p}\downarrow}(\tau) = e^{(\hat{H}_{FP}-\mu\hat{N}_\downarrow-\mu_\uparrow\hat{N}_\uparrow)\tau}\hat{c}_{\mathbf{p}\downarrow}e^{-(\hat{H}_{FP}-\mu\hat{N}_\downarrow-\mu_\uparrow\hat{N}_\uparrow)\tau}\ , \tag{2.2}$$

and θ the Heaviside function. The propagator $G_\downarrow(\mathbf{p},\tau)$ is written in the momentum imaginary-time representation, μ is a free parameter, $\hat{N}_\sigma$ is the number operator for spin-σ particles, and $\mu_\uparrow$ is the chemical potential of the spin-up sea. The state

$$|\Phi_0^{N_\uparrow}\rangle = |\rangle_\downarrow|FS(N_\uparrow)\rangle\ , \tag{2.3}$$

consists of the spin-down vacuum and the non-interacting spin-up Fermi sea. Since we are dealing with an impurity spin-down atom, $G_\downarrow$ is only non-zero for times $\tau > 0$. The ground-state energy and Z-factor can be extracted from the Green's function of Eq. (2.1). Inserting a complete set of eigenstates $|\Psi_n^{N_\uparrow}\rangle$ of the full Hamiltonian $\hat{H}_{FP}$ for one spin-down particle and $N_\uparrow$ spin-up particles into Eq. (2.1) gives

$$\begin{aligned} G_\downarrow(\mathbf{p},\tau) &= -\theta(\tau)\sum_n |\langle\Psi_n^{N_\uparrow}|\hat{c}^\dagger_{\mathbf{p}\downarrow}|\Phi_0^{N_\uparrow}\rangle|^2 e^{-(E_n(N_\uparrow)-E_{FS}-\mu)\tau} \\ &\overset{\tau\to\pm\infty}{=} -Z_{pol}(\mathbf{p})\; e^{-(E_{pol}(\mathbf{p})-\mu)\tau}\;, \end{aligned} \tag{2.4}$$

with $E_{pol}(\mathbf{p})$ the energy of the polaron at momentum $\mathbf{p}$ for the impurity and $E_n(N_\uparrow)$ the energy eigenvalues of the Hamiltonian $\hat{H}_{FP}$ of Eq. (1.23). The energy of the ideal spin-up Fermi gas is $E_{FS} = 3\;\epsilon_F N_\uparrow/5$, with $\epsilon_F = k_F^2/(2m_\uparrow)$ the Fermi energy and k_F the Fermi momentum. This asymptotic behavior implies a pole singularity for the Green's function in imaginary-frequency representation

$$\begin{aligned} G_\downarrow(\mathbf{p},\omega) &= \int_0^{+\infty} d\tau\; e^{i\omega\tau} G_\downarrow(\mathbf{p},\tau) \\ &= \frac{Z_{pol}(\mathbf{p})}{i\omega + \mu - E_{pol}(\mathbf{p})} + \text{ regular part }. \end{aligned} \tag{2.5}$$

The Feynman-Dyson perturbation series for the one-particle Green's function in imaginary time τ and momentum $\mathbf{p}$ is given by

$$\begin{aligned} G_\downarrow(\mathbf{p},\tau) = -\sum_{n=0}^{\infty}(-1)^n \frac{1}{n!}\int_0^\infty d\tau_1 \ldots \int_0^\infty d\tau_n \\ \langle\Phi_0^{N_\uparrow}|T\left[\hat{H}_{\downarrow\uparrow I}(\tau_1)\ldots\hat{H}_{\downarrow\uparrow I}(\tau_{i+1})\ldots\hat{H}_{\downarrow\uparrow I}(\tau_n)\hat{c}_{\mathbf{p}\downarrow I}(\tau)\hat{c}^\dagger_{\mathbf{p}\downarrow I}(0)\right]|\Phi_0^{N_\uparrow}\rangle_{\text{connected}}\;, \end{aligned} \tag{2.6}$$

with T the time-ordered product and the operators with subscript I are given in the interaction picture. Each term in this series can be visualized by Feynman diagrams, whereby only the connected diagrams have to be taken into account. The operator $\hat{c}_{\mathbf{p}\sigma I}(\tau)$ in the interaction picture is defined as:

$$\hat{c}_{\mathbf{p}\sigma I}(\tau) \equiv e^{\hat{K}_0\tau}\hat{c}_{\mathbf{p}\sigma}e^{-\hat{K}_0\tau}\;, \tag{2.7}$$

with

$$\hat{K}_0 \;=\; \sum_{\mathbf{k}\sigma}(\epsilon_{\mathbf{k}\sigma}-\mu_\sigma)\hat{c}^\dagger_{\mathbf{k}\sigma}\hat{c}_{\mathbf{k}\sigma} \equiv \hat{H}_0 - \sum_\sigma \mu_\sigma \hat{N}_\sigma\;, \tag{2.8}$$

where we introduce the notation $\mu_\downarrow = \mu$ for convenience. The time dependence of the creation (annihilation) operators $\hat{c}^\dagger_{\mathbf{p}\sigma I}(\tau)$ ($\hat{c}_{\mathbf{p}\sigma I}(\tau)$) in the interaction picture is the solution of the differential equation [4]:

$$\begin{aligned} -\frac{\partial\hat{c}_{\mathbf{p}\sigma I}(\tau)}{\partial\tau} &= \left[\hat{c}_{\mathbf{p}\sigma I}(\tau), \hat{K}_0\right] \\ &= e^{\hat{K}_0\tau}\left(\epsilon_{\mathbf{p}\sigma}-\mu_\sigma\right)\left[\hat{c}_{\mathbf{p}\sigma}, \hat{c}^\dagger_{\mathbf{p}\sigma}\hat{c}_{\mathbf{p}\sigma}\right]e^{-\hat{K}_0\tau} \\ &= (\epsilon_{\mathbf{p}\sigma}-\mu_\sigma)\hat{c}_{\mathbf{p}\sigma I}(\tau)\;. \end{aligned} \tag{2.9}$$

Thus,

$$\hat{c}_{\mathbf{p}\sigma I}(\tau) = \hat{c}_{\mathbf{p}\sigma} e^{-(\epsilon_{\mathbf{p}\sigma}-\mu_\sigma)\tau} , \tag{2.10}$$

$$\hat{c}^\dagger_{\mathbf{p}\sigma I}(\tau) = \hat{c}^\dagger_{\mathbf{p}\sigma} e^{(\epsilon_{\mathbf{p}\sigma}-\mu_\sigma)\tau} . \tag{2.11}$$

For an operator $\hat{O}_S$ in the Schrödinger picture the time-dependence of the operator $\hat{O}_I(\tau)$ in the interaction picture is given by

$$\hat{O}_I(\tau) = e^{\hat{K}_0\tau}\hat{O}_S e^{-\hat{K}_0\tau} . \tag{2.12}$$

2.2 Feynman diagrams for the Fermi polaron

To calculate $G_\downarrow(\mathbf{p},\tau)$ with the use of Eq. (2.6) we need to evaluate the matrix elements in this expression. In this section we will calculate some low order contributions ($n = 1$ and $n = 2$). In the end of this section, we will show how to create higher order diagrams for the Fermi polaron. First we give the expressions of the free Green's function. The free Green's function for the impurity with momentum $\mathbf{p}$ is given by

$$G^0_\downarrow(\mathbf{p},\tau) = -\theta(\tau)\langle\Phi_0^{N_\uparrow}|T\left[\hat{c}_{\mathbf{p}\downarrow I}(\tau)\hat{c}^\dagger_{\mathbf{p}\downarrow I}(0)\right]|\Phi_0^{N_\uparrow}\rangle = -\theta(\tau)e^{-(\epsilon_{\mathbf{p}\downarrow}-\mu)\tau} , \tag{2.13}$$

with $\epsilon_{\mathbf{p}\downarrow} = \frac{p^2}{2m_\downarrow}$ the impurity dispersion. From now on, we drop the subscript I, since in the following all time-dependent operators will be in the interaction picture, unless stated otherwise. The free Green's function for the spin-up particles in the Fermi sea with momentum $\mathbf{k}$ is given by

$$\begin{aligned} G^0_\uparrow(\mathbf{k},\tau) &= -\langle\Phi_0^{N_\uparrow}|T\left[\hat{c}_{\mathbf{k}\uparrow}(\tau)\hat{c}^\dagger_{\mathbf{k}\uparrow}(0)\right]|\Phi_0^{N_\uparrow}\rangle \\ &= -\theta(k-k_F)e^{-(\epsilon_{\mathbf{k}\uparrow}-\epsilon_F)\tau}\theta(\tau) + \theta(k_F-k)e^{-(\epsilon_{\mathbf{k}\uparrow}-\epsilon_F)\tau}\theta(-\tau) , \end{aligned} \tag{2.14}$$

with the dispersion given by $\epsilon_{\mathbf{k}\uparrow} = \frac{k^2}{2m_\uparrow}$. The contribution $\mathcal{D}_1$ in Eq. (2.6) for $n = 1$ is

$$\begin{aligned} \mathcal{D}_1 &= \int_0^\infty d\tau_1 \langle\Phi_0^{N_\uparrow}|T\left[\hat{H}_{\downarrow\uparrow}(\tau_1)\hat{c}_{\mathbf{p}\downarrow}(\tau)\hat{c}^\dagger_{\mathbf{p}\downarrow}(0)\right]|\Phi_0^{N_\uparrow}\rangle \\ &= \frac{g_0}{(2\pi)^3}\int_0^\infty d\tau_1 \int_{\mathcal{B},|\mathbf{q}_h|<k_F} d\mathbf{q}_h \langle\Phi_0^{N_\uparrow}|T\left[\hat{c}^\dagger_{\mathbf{p}\downarrow}(\tau_1)\hat{c}_{\mathbf{p}\downarrow}(\tau_1)\hat{c}^\dagger_{\mathbf{q}_h\uparrow}(\tau_1)\hat{c}_{\mathbf{q}_h\uparrow}(\tau_1)\hat{c}_{\mathbf{p}\downarrow}(\tau)\hat{c}^\dagger_{\mathbf{p}\downarrow}(0)\right]|\Phi_0^{N_\uparrow}\rangle \\ &= \frac{g_0}{(2\pi)^3}\int_0^\tau d\tau_1 \int_{\mathcal{B},|\mathbf{q}_h|<k_F} d\mathbf{q}_h \sum_{n,n'} \langle\Phi_0^{N_\uparrow}|\hat{c}_{\mathbf{p}\downarrow}(\tau)\hat{c}^\dagger_{\mathbf{p}\downarrow}(\tau_1)|\Phi_n^{N_\uparrow}\rangle\langle\Phi_n^{N_\uparrow}|\hat{c}^\dagger_{\mathbf{q}_h\uparrow}(\tau_1)\hat{c}_{\mathbf{q}_h\uparrow}(\tau_1)|\Phi_{n'}^{N_\uparrow}\rangle \\ &\qquad \langle\Phi_{n'}^{N_\uparrow}|\hat{c}_{\mathbf{p}\downarrow}(\tau_1)\hat{c}^\dagger_{\mathbf{p}\downarrow}(0)|\Phi_0^{N_\uparrow}\rangle \\ &= g_0\int_0^\tau d\tau_1 G^0_\downarrow(\mathbf{p},\tau-\tau_1)G^0_\downarrow(\mathbf{p},\tau_1)\; n_\uparrow , \end{aligned} \tag{2.15}$$

with $|\Phi_n^{N_\uparrow}\rangle$ a complete set of eigenstates of the Hamiltonian $\hat{H}_0$. Note that we have taken the thermodynamic limit, and $n_\uparrow$ is the density of spin-$\uparrow$ fermions. The contribution $\mathcal{D}_2$ for

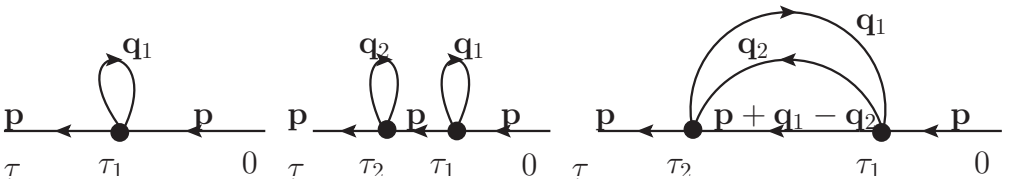

Figure 2.1 – First and second order diagrams. Imaginary times run from right to left. The straight line represents the propagation of the impurity. The forward oriented arc represents a particle of the Fermi sea, a backward propagating arc a hole in the Fermi sea. The interaction vertices are denoted by dots.

$n = 2$ in Eq. (2.6) is

$$\begin{aligned}\mathcal{D}_2 &= -\int_0^\infty d\tau_2 \int_0^{\tau_2} d\tau_1 \langle \Phi_0^{N_\uparrow} | T\left[\hat{H}_{\downarrow\uparrow}(\tau_1)\hat{H}_{\downarrow\uparrow}(\tau_2)\hat{c}_{\mathbf{p}\downarrow}(\tau)\hat{c}^\dagger_{\mathbf{p}\downarrow}(0)\right] |\Phi_0^{N_\uparrow}\rangle \\ &= \frac{-g_0^2}{(2\pi)^6}\int_0^\tau d\tau_2 \int_0^{\tau_2} d\tau_1 \Bigg(\int_{\mathcal{B},|\mathbf{q_1}|<k_F,|\mathbf{q_2}|>k_F} d\mathbf{q_1}d\mathbf{q_2}\ \ \hat{c}^\dagger_{\mathbf{p}+\mathbf{q}_1-\mathbf{q}_2\downarrow}(\tau_1)\,❶\,\hat{c}_{\mathbf{p}\downarrow}(\tau_1)\,❺ \\ &\quad \times \hat{c}^\dagger_{\mathbf{q}_2\uparrow}(\tau_1)\,❸\,\hat{c}_{\mathbf{q}_1\uparrow}(\tau_1)\,❹\,\hat{c}^\dagger_{\mathbf{p}\downarrow}(\tau_2)\,❷\,\hat{c}_{\mathbf{p}+\mathbf{q}_1-\mathbf{q}_2\downarrow}(\tau_2)\,❶\,\hat{c}^\dagger_{\mathbf{q}_1\uparrow}(\tau_2)\,❹\,\hat{c}_{\mathbf{q}_2\uparrow}(\tau_2)\,❸\,\hat{c}_{\mathbf{p}\downarrow}(\tau)\,❷\,\hat{c}^\dagger_{\mathbf{p}\downarrow}(0)\,❺ \\ &\quad + \int_{\mathcal{B},|\mathbf{q_1}|<k_F,|\mathbf{q_2}|<k_F} d\mathbf{q_1}d\mathbf{q_2}\ \ \hat{c}^\dagger_{\mathbf{p}\downarrow}(\tau_1)\,❶\,\hat{c}_{\mathbf{p}\downarrow}(\tau_1)\,❺\,\hat{c}^\dagger_{\mathbf{q}_1\uparrow}(\tau_1)\,❸\,\hat{c}_{\mathbf{q}_1\uparrow}(\tau_1)\,❸\,\hat{c}^\dagger_{\mathbf{p}\downarrow}(\tau_2)\,❷ \\ &\quad \times\ \ \hat{c}_{\mathbf{p}\downarrow}(\tau_2)\,❶\,\hat{c}^\dagger_{\mathbf{q}_2\uparrow}(\tau_2)\,❹\,\hat{c}_{\mathbf{q}_2\uparrow}(\tau_2)\,❹\,\hat{c}_{\mathbf{p}\downarrow}(\tau)\,❷\,\hat{c}^\dagger_{\mathbf{p}\downarrow}(0)\,❺ \Bigg)\,.\end{aligned} \tag{2.16}$$

We use Wick's theorem in the last line, with the contraction between a creation and an annihilation operator given by:

$$\begin{aligned}\hat{c}^\dagger_{\mathbf{p}\sigma}(\tau_1)\,❶\,\hat{c}_{\mathbf{p}'\sigma'}(\tau_2)\,❶ &= T\left(\hat{c}^\dagger_{\mathbf{p}\sigma}(\tau_1)\hat{c}_{\mathbf{p}'\sigma'}(\tau_2)\right) - N\left(\hat{c}^\dagger_{\mathbf{p}\sigma}(\tau_1)\hat{c}_{\mathbf{p}'\sigma'}(\tau_2)\right) \\ &= G^0_\sigma(\mathbf{p},\tau_2-\tau_1)\delta_{\sigma,\sigma'}\delta(\mathbf{p}-\mathbf{p}')\,.\end{aligned} \tag{2.17}$$

with $T(\ldots)$ the time ordered product and $N(\ldots)$ the normal ordered product. The contribution $\mathcal{D}_2$ can now be written in terms of Green's functions:

$$\begin{aligned}\mathcal{D}_2 = \frac{-g_0^2}{(2\pi)^6}\int_0^\tau d\tau_2 \int_0^{\tau_2} d\tau_1 \Bigg(&\int_{\mathcal{B},|\mathbf{q_1}|<k_F,|\mathbf{q_2}|>k_F} d\mathbf{q_1}d\mathbf{q_2}\ \ G^0_\downarrow(\mathbf{p}+\mathbf{q}_1-\mathbf{q}_2,\tau_2-\tau_1) \\ &\times G^0_\downarrow(\mathbf{p},\tau_1)G^0_\uparrow(\mathbf{q}_2,\tau_2-\tau_1)G^0_\uparrow(\mathbf{q}_1,\tau_1-\tau_2)G^0_\downarrow(\mathbf{p},\tau-\tau_2) \\ &- \int_{\mathcal{B},|\mathbf{q_1}|<k_F,|\mathbf{q_2}|<k_F} d\mathbf{q_1}d\mathbf{q_2}\ \ G^0_\downarrow(\mathbf{p},\tau_2-\tau_1)G^0_\downarrow(\mathbf{p},\tau-\tau_2)G^0_\downarrow(\mathbf{p},\tau_1) \\ &\times\ G^0_\uparrow(\mathbf{q}_1,0^-)\ G^0_\uparrow(\mathbf{q}_2,0^-)\Bigg)\,.\end{aligned} \tag{2.18}$$

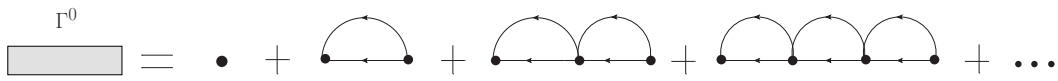

Figure 2.2 – Graphical representation of ladder diagrams. Imaginary times runs from right to left.

From the previous examples we can already deduce some characteristics of the diagrams. Since we only have one spin-down particle, there is only one possibility for the contractions of the operators of the spin-down particle. To construct a diagram, the propagation in (imaginary) time of the impurity can be depicted with a straight line, which we will call the backbone line (BBL) of the diagram. Another property that can be seen from the examples is that no time can become larger than τ. So, the upper limits $+\infty$ in Eq. (2.6) can be replaced by τ. A third property is that only the impurity can create particles and holes in the Fermi sea, and as a consequence we have no disonnected diagrams.

In Fig. 2.1 we show the diagrams which correspond to the first and second order contributions. Creating higher order diagrams can be done easily in the following way. First, draw a BBL which goes from 0 to τ. Then, add vertices on the BBL that represent the bare interaction matrix element g_0, and the number of vertices equals the order n. Next, draw particles and hole lines onto the BBL in a way that each vertex has two incoming lines and two outgoing lines. Since the impurity is propagating forward and the particle number should be conserved at each time, the number of the particles and holes in the Fermi sea should always be equal at each time. Each diagram acquires a sign $(-1)^{n+\mathcal{L}}$, with n the order and $\mathcal{L}$ the number of loops. Each hole line acquires a momentum $|\mathbf{q}| < k_F$, a particle line will have a momentum $|\mathbf{q}| > k_F$. The momentum of the impurity is then fixed by the conservation of momentum at each vertex.

2.3 Renormalization of the contact interaction

As explained in Sec. 1.3.1, we have the freedom to choose any effective potential $V_{\downarrow\uparrow}(\mathbf{k})$ as long as it reproduces the desired scattering length a_s. Because we have set $V_{\downarrow\uparrow}(\mathbf{k}) = g_0$, however, ultraviolet divergences arise. Those were regularised by considering fermions that move on a lattice. The continuum limit cannot be taken directly. For example: Eq. (2.18) will diverge if the lattice spacing $l \to 0$ (and keeping g_0 fixed). To overcome this problem we will show in this section that the continuum limit can be taken after a suitable renormalization of the bare contact interaction. To this end we evaluate an infinite series of so-called ladder diagrams (see Fig. 2.2) $\Gamma^0(\mathbf{p}, \tau)$ given by:

$$\Gamma^0(\mathbf{p},\tau) = g_0 - g_0 \int_0^\tau d\tau_1 \frac{1}{(2\pi)^3} \int_{\mathcal{B},|\mathbf{q}|>\mathbf{k}_F} d\mathbf{q}\;\; G^0_\downarrow(\mathbf{p}-\mathbf{q},\tau_1) G^0_\uparrow(\mathbf{q},\tau_1)\Gamma^0(\mathbf{p},\tau-\tau_1)\;. \quad (2.19)$$

Beside the time, $\Gamma^0(\mathbf{p}, \tau)$ only depends on the total incoming momentum $\mathbf{p}$. This is a consequence of the fact that the interaction potential $V_{\downarrow\uparrow}(\mathbf{k})$ is a Dirac delta-function, so that $V_{\downarrow\uparrow}(\mathbf{k})$ does not depend on the momentum transfer. This can be written in imaginary

frequency domain,

$$\frac{1}{\Gamma^0(\mathbf{p},\Omega)} = \frac{1}{g_0} + \frac{1}{(2\pi)^4}\int_{-\infty}^{+\infty} d\omega \int_{\mathcal{B},|\mathbf{q}|>\mathbf{k_F}} d\mathbf{q}\;\; G^0_\downarrow(\mathbf{p}-\mathbf{q},\Omega-\omega)G^0_\uparrow(\mathbf{q},\omega)\;, \tag{2.20}$$

with Ω and ω imaginary frequencies. The free propagators $G^0_\downarrow(\mathbf{p}-\mathbf{q},\Omega-\omega)$ and $G^0_\uparrow(\mathbf{q},\omega)$ in imaginary frequency domain are given by

$$\begin{cases} G^0_\downarrow(\mathbf{p}-\mathbf{q},\Omega-\omega) = \frac{1}{i(\Omega-\omega)-\frac{(\mathbf{p}-\mathbf{q})^2}{2m_\downarrow}+\mu}\;; \\ G^0_\uparrow(\mathbf{q},\omega) = \frac{1}{i\omega-\frac{q^2}{2m_\uparrow}+\epsilon_F}\;. \end{cases} \tag{2.21}$$

By making use of the residue theorem the integral over frequencies can be calculated. Identifying the poles ω_1 and ω_2 gives

$$\begin{cases} \omega_1 = \Omega + i\left(\frac{(\mathbf{p}-\mathbf{q})^2}{2m_\downarrow}-\mu\right)\;; \\ \omega_2 = -i(\frac{q^2}{2m_\uparrow}-\epsilon_F)\;. \end{cases} \tag{2.22}$$

By closing the contour in the lower half of the complex plane, and choosing $\mu<0$, one gets:

$$\frac{1}{\Gamma^0(\mathbf{p},\Omega)} = \frac{1}{g_0} - \frac{1}{(2\pi)^3}\int_{\mathcal{B},|\mathbf{q}|>k_F} d\mathbf{q}\;\; \frac{1}{i\Omega-\frac{(\mathbf{p}-\mathbf{q})^2}{2m_\downarrow}+\mu-\frac{q^2}{2m_\uparrow}+\epsilon_F}\;. \tag{2.23}$$

With the use of Eq. (1.12) the interaction strength parameter g_0 can be removed in favour of the scattering length a_s in Eq. (2.23),

$$\frac{1}{\Gamma^0(\mathbf{p},\Omega)} = \frac{m_r}{2\pi a_s} - \frac{1}{(2\pi)^3}\int_{\mathcal{B},|\mathbf{q}|>k_F} d\mathbf{q}\;\; \frac{1}{i\Omega-\frac{(\mathbf{p}-\mathbf{q})^2}{2m_\downarrow}+\mu-\frac{\mathbf{q}^2}{2m_\uparrow}+\epsilon_F} - \frac{1}{(2\pi)^3}\int_{\mathcal{B}} d\mathbf{q}\;\; \frac{2m_r}{q^2}\;. \tag{2.24}$$

By grouping the two integrands together, this expression is well-defined in the zero-range limit. We can take the continuum limit $l\to 0$ and $g_0\to 0^-$ such that a_s is fixed. To evaluate Eq. (2.24) we write ${\Gamma^0}^{-1}(\mathbf{p},\Omega)$ as

$${\Gamma^0}^{-1}(\mathbf{p},\Omega) = {\tilde{\Gamma}^0}^{-1}(\mathbf{p},\Omega) - \bar{\Pi}(\mathbf{p},\Omega)\;, \tag{2.25}$$

with

$$\frac{1}{\tilde{\Gamma}^0(\mathbf{p},\Omega)} = \frac{m_r}{2\pi a_s} - \int \frac{d\mathbf{q}}{(2\pi)^3}\left(\frac{1}{i\Omega-\frac{(\mathbf{p}-\mathbf{q})^2}{2m_\downarrow}+\mu-\frac{q^2}{2m_\uparrow}+\epsilon_F}+\frac{2m_r}{q^2}\right)\;, \tag{2.26}$$

and $\bar{\Pi}(\mathbf{p},\Omega)$:

$$\bar{\Pi}(\mathbf{p},\Omega) = -\int \frac{d\mathbf{q}}{(2\pi)^3}\frac{\theta(k_F-|\mathbf{q}|)}{i\Omega-\frac{q^2}{2m_\uparrow}-\frac{(\mathbf{p}-\mathbf{q})^2}{2m_\downarrow}+\mu+\epsilon_F}\;. \tag{2.27}$$

The function ${\tilde{\Gamma}^0}^{-1}(\mathbf{p},\Omega)$ can be calculated analytically, for $\Omega\neq 0$ or $\mu<-\epsilon_F$:

$$\frac{1}{\tilde{\Gamma}^0(\mathbf{p},\Omega)} = \frac{m_r}{2\pi a_s} - \frac{1}{\sqrt{2}\pi}m_r^{3/2}\sqrt{-i\Omega-\mu+\frac{p^2}{2(m_\uparrow+m_\downarrow)}-\epsilon_F}\;, \tag{2.28}$$

with $m_r = \frac{m_\uparrow m_\downarrow}{m_\uparrow + m_\downarrow}$. To construct Feynman diagrams (see Sec. 2.6) we will use $\Gamma^0(\mathbf{p}, \tau)$ in the momentum-imaginary-time representation as a renormalized interaction or dressed interaction. We get $\Gamma^0(\mathbf{p}, \tau)$ by calculating the following Fourier transform:

$$\Gamma^0(\mathbf{p}, \tau) = \frac{1}{2\pi} \int_{-\infty}^{+\infty} d\Omega \;\; \Gamma^0(\mathbf{p}, \Omega) e^{-i\tau\Omega} \; . \tag{2.29}$$

We obtain for $\tilde{\Gamma}^0(\mathbf{p}, \tau)$, if $\mu < -\epsilon_F - \frac{1}{2m_r a_s^2}$ (see appendix B):

$$\tilde{\Gamma}^0(\mathbf{p}, \tau) = -\frac{4\pi}{(2m_r)^{3/2}} e^{(\mu + \epsilon_F - \frac{p^2}{2(m_\downarrow + m_\uparrow)})\tau} \left(\frac{1}{\sqrt{\pi\tau}} + \frac{1}{a_s\sqrt{2m_r}} e^{\frac{\tau}{2m_r a_s^2}} \operatorname{erfc}\left(-\sqrt{\frac{\tau}{2m_r}} \frac{1}{a_s} \right) \right) \; , \tag{2.30}$$

with erfc the complementary error function. Consider now the function $(\Gamma^0 - \tilde{\Gamma}^0)(\mathbf{p}, \tau)$:

$$\Gamma^0(\mathbf{p}, \tau) - \tilde{\Gamma}^0(\mathbf{p}, \tau) = \frac{1}{2\pi} \int_{-\infty}^{+\infty} d\Omega \left(\Gamma^0(\mathbf{p}, \Omega) - \tilde{\Gamma}^0(\mathbf{p}, \Omega) \right) e^{-i\tau\Omega} \; . \tag{2.31}$$

The function $\left(\Gamma^0(\mathbf{p}, \tau) - \tilde{\Gamma}^0(\mathbf{p}, \tau) \right)$ can be computed numerically and is a well-behaved and bounded function, and therefore it can be tabulated very accurately in a $(|\mathbf{p}|, \tau)$ grid. Whenever $\Gamma^0(\mathbf{p}, \tau)$ is needed, we calculate it as a sum of the analytically obtained function $\tilde{\Gamma}^0(\mathbf{p}, \tau)$ and the tabulated function $\left(\Gamma^0(\mathbf{p}, \tau) - \tilde{\Gamma}^0(\mathbf{p}, \tau) \right)$.

2.4 The one-body self-energy $\Sigma(\mathbf{p}, \Omega)$

In this section we introduce the one-body self-energy $\Sigma(\mathbf{p}, \Omega)$, with $\mathbf{p}$ the momentum of the impurity and Ω the imaginary frequency, and show its relation with the polaron ground-state energy $E_{pol}(\mathbf{p})$ and the Z-factor $Z_{pol}(\mathbf{p})$. The one-body self-energy $\Sigma(\mathbf{p}, \Omega)$ is related to the Green's function $G_\downarrow(\mathbf{p}, \Omega)$ by means of the Dyson equation:

$$G_\downarrow(\mathbf{p}, \Omega) = G_\downarrow^0(\mathbf{p}, \Omega) + G_\downarrow^0(\mathbf{p}, \Omega) \Sigma(\mathbf{p}, \Omega) G_\downarrow(\mathbf{p}, \Omega) \; . \tag{2.32}$$

To emphasise the dependence of $G_\downarrow(\mathbf{p}, \tau)$ and $\Sigma(\mathbf{p}, \tau)$ on the free parameter μ, we use the notation:

$$\begin{aligned} G_\downarrow(\mathbf{p}, \tau) \equiv G_\downarrow(\mathbf{p}, \tau, \mu) &= G_\downarrow(\mathbf{p}, \tau, 0) \; e^{\mu\tau} \; , \\ \Sigma(\mathbf{p}, \tau) \equiv \Sigma(\mathbf{p}, \tau, \mu) &= \Sigma(\mathbf{p}, \tau, 0) \; e^{\mu\tau} \; . \end{aligned} \tag{2.33}$$

The simple exponential dependence on μ follows from the fact that there is a backbone line. To obtain a relation between the one-body self-energy and $E_{pol}(\mathbf{p})$ [22], consider the poles for $G_\downarrow(\mathbf{p}, \tau)$ given in Eqs. (2.32) and (2.5):

$$\begin{aligned} \frac{i\Omega + \mu - E_{pol}(\mathbf{p})}{Z_{pol}(\mathbf{p})} &= G_\downarrow^{0\,-1}(\mathbf{p}, \Omega, \mu) - \Sigma(\mathbf{p}, \Omega, \mu) \\ &= i\Omega - \frac{p^2}{2m_\downarrow} + \mu - \Sigma(\mathbf{p}, \Omega, \mu) \; . \end{aligned} \tag{2.34}$$

For small values of Ω we can use the following Taylor expansion:

$$\Sigma(\mathbf{p},\Omega,\mu) = \Sigma(\mathbf{p},\Omega=0,\mu) + \Omega \left.\frac{\partial\Sigma(\mathbf{p},\Omega,\mu)}{\partial\Omega}\right|_{\Omega=0} + \dots \ . \tag{2.35}$$

By differentiating Eq. (2.33) with respect to μ and integrating over τ we obtain that $\left.\frac{\partial\Sigma(\mathbf{p},\Omega,\mu)}{\partial\Omega}\right|_{\Omega=0} = i\,\frac{\partial\Sigma(\mathbf{p},\Omega=0,\mu)}{\partial\mu}$. Since μ is a free parameter it is allowed to set it equal to $E_{pol}(\mathbf{p})$. With the aid of Eq. (2.35), we can rewrite Eq. (2.34) for small values of Ω as

$$\frac{i\Omega}{Z_{pol}(\mathbf{p})} = i\Omega - \frac{p^2}{2m_\downarrow} + E_{pol}(\mathbf{p}) - \Sigma(\mathbf{p},\Omega=0,\mu=E_{pol}(\mathbf{p})) - i\Omega \left.\frac{\partial\Sigma(\mathbf{p},\Omega=0,\mu)}{\partial\mu}\right|_{\mu=E_{pol}(\mathbf{p})} . \tag{2.36}$$

Identifying the real and imaginary parts in Eq. (2.36) gives the following relations for $E_{pol}(\mathbf{p})$ and $Z_{pol}(\mathbf{p})$:

$$E_{pol}(\mathbf{p}) = \frac{p^2}{2m_\downarrow} + \Sigma\left(\mathbf{p},\Omega=0,\mu=E_{pol}(\mathbf{p})\right) \ , \tag{2.37}$$

$$Z_{pol}(\mathbf{p}) = \frac{1}{1 - \left.\frac{\partial\Sigma(\mathbf{p},\Omega=0,\mu)}{\partial\mu}\right|_{\mu=E_{pol}(\mathbf{p})}} \ . \tag{2.38}$$

In the previous section we have summed an infinite subclass of diagrams, which resulted in a renormalized or dressed interaction Γ^0. We are now able to draw Feynman diagrams that are well-defined in the continuum limit. Let us evaluate the one-body self-energy $\Sigma^{(1)}(\mathbf{p},\Omega)$ built from one renormalized interaction Γ^0 and one spin-$\uparrow$ hole propagator $G^0_\uparrow$, as shown in Fig. 2.3. In the next section we will see that $\Sigma^{(1)}(\mathbf{p},\Omega)$ includes all the 1 p-h excitations of the polaron system. By making use of the Feynman rules (see for example [4, 21]) the self-energy $\Sigma^{(1)}(\mathbf{p},\Omega)$ is given by:

$$\Sigma^{(1)}(\mathbf{p},\Omega) = \int_{|\mathbf{q}|<k_F} \frac{d\mathbf{q}}{(2\pi)^3} \int \frac{d\omega}{2\pi} \Gamma^0(\mathbf{p}+\mathbf{q},\Omega+\omega) G^0_\uparrow(\mathbf{q},\omega) \ , \tag{2.39}$$

with ω the imaginary frequency and $\mathbf{q}$ the momentum of the spin-up propagator. In Sec. 2.6 the diagram of Fig. 2.3 will be called the first order diagram.

2.5 A variational calculation with 1 p-h excitations

In this section we calculate the ground-state energy of the Fermi polaron by using a variational method with a related wave function that includes 1p-h excitations [23].

One proposes a state $|\psi\rangle$

$$|\psi\rangle = \phi_0|\mathbf{0},FS\rangle + \sum_{\mathbf{k},\mathbf{q}\in\mathcal{B}} \phi_{\mathbf{k},\mathbf{q}}|\mathbf{k},\mathbf{q}\rangle \ . \tag{2.40}$$

The state $|\mathbf{0},FS\rangle$ is the spin-up FS with the spin-down impurity with momentum $\mathbf{0}$ and $|\mathbf{k},\mathbf{q}\rangle$ represents the FS with a particle-hole excitation where the particle has momentum $\mathbf{k}$

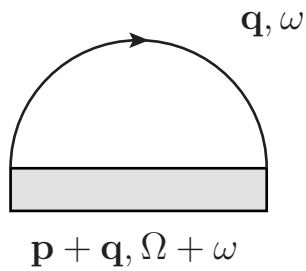

Figure 2.3 – Graphical presentation of a diagram with one hole propagator for the one-body self-energy. The grey box is the renormalized interaction $\Gamma^0(\mathbf{p}+\mathbf{q}, \Omega+\omega)$ and the arc represents the hole propagator $G^0_\uparrow(\mathbf{q}, \omega)$, with $|\mathbf{q}| < k_F$.

($k = |\mathbf{k}| > k_F$) and the hole has momentum $\mathbf{q}$ ($q = |\mathbf{q}| < k_F$). The state $|\mathbf{k}, \mathbf{q}\rangle$ also includes the impurity with momentum $\mathbf{q} - \mathbf{k}$. The energy of this state is given by $\langle\psi|\hat{H}_{\mathrm{FP}}|\psi\rangle$:

$$\begin{aligned}\langle\psi|\hat{H}_{\mathrm{FP}}|\psi\rangle = &\left(|\phi_0|^2 E_{FS} + \sum_{\mathbf{k},\mathbf{q}\in\mathcal{B}} |\phi_{\mathbf{k},\mathbf{q}}|^2 \; E_{FS}\right) \\ &+ \sum_{\mathbf{k},\mathbf{q}\in\mathcal{B}} |\phi_{\mathbf{k},\mathbf{q}}|^2 (\epsilon_{\mathbf{k}\uparrow} + \epsilon_{\mathbf{q}-\mathbf{k}\downarrow} - \epsilon_{\mathbf{q}\uparrow}) + \frac{g_0}{\mathcal{V}} \left(\sum_{\mathbf{q}\in\mathcal{B}} |\phi_0|^2 + \sum_{\mathbf{k},\mathbf{k}',\mathbf{q}\in\mathcal{B}} \phi_{\mathbf{k}',\mathbf{q}} \phi^*_{\mathbf{k},\mathbf{q}}\right. \\ &\left. + \sum_{\mathbf{k},\mathbf{q},\mathbf{q}'\in\mathcal{B}} \phi_{\mathbf{k},\mathbf{q}} \phi^*_{\mathbf{k},\mathbf{q}'} + \sum_{\mathbf{k},\mathbf{q}\in\mathcal{B}} (\phi_0^* \phi_{\mathbf{k},\mathbf{q}} + \phi_0 \phi^*_{\mathbf{k},\mathbf{q}})\right) ,\end{aligned} \tag{2.41}$$

with E_{FS} the energy of the ideal spin-up Fermi gas. The sums on $\mathbf{q}$ and $\mathbf{k}$ are implicitly limited to $q < k_F$ and $k > k_F$. Since $|\psi\rangle$ should be normalized, it is valid that

$$\left(|\phi_0|^2 E_{FS} + \sum_{\mathbf{k},\mathbf{q}\in\mathcal{B}} |\phi_{\mathbf{k},\mathbf{q}}|^2 E_{FS}\right) = E_{FS} \, . \tag{2.42}$$

In the following we will drop this term and consider the energy with respect to E_{FS}. We will see in Eq. (2.46) that for large momenta k the following relation is valid: $\phi_{\mathbf{k},\mathbf{q}} \sim 1/k^2$. Most of the sums over momenta in Eq. (2.41) will diverge in the continuum limit for large momenta. This singular behavior is regularized by the fact that $g_0 \to 0^-$ if $l \to 0$. The term $\sum_{\mathbf{k},\mathbf{q},\mathbf{q}'\in\mathcal{B}} \phi_{\mathbf{k},\mathbf{q}} \phi^*_{\mathbf{k},\mathbf{q}'}$, however, is convergent and gives a zero contribution when multiplied by g_0.

We have to minimize the function $\langle\psi|\hat{H}_{\mathrm{FP}}|\psi\rangle$ under the constraint that $\langle\psi|\psi\rangle = 1$, therefore we introduce the function Λ:

$$\Lambda = \langle\psi|\hat{H}_{\mathrm{FP}}|\psi\rangle - E \left(|\phi_0|^2 + \sum_{\mathbf{k},\mathbf{q}\in\mathcal{B}} |\phi_{\mathbf{k},\mathbf{q}}|^2 - 1\right) , \tag{2.43}$$

where E is a Langrange multiplier. Differentiating Λ with respect to ϕ_0^* and $\phi_{\mathbf{k},\mathbf{q}}^*$ gives

$$\frac{\partial \Lambda}{\partial \phi_0^*} = \frac{g_0}{\mathcal{V}} \sum_{\mathbf{q}\in\mathcal{B}} \phi_0 + \frac{g_0}{\mathcal{V}} \sum_{\mathbf{k},\mathbf{q}\in\mathcal{B}} \phi_{\mathbf{k},\mathbf{q}} - E\phi_0 = 0 \,, \tag{2.44}$$

$$\frac{\partial \Lambda}{\partial \phi_{\mathbf{k},\mathbf{q}}^*} = (\epsilon_{\mathbf{k}\uparrow} + \epsilon_{\mathbf{q}-\mathbf{k}\downarrow} - \epsilon_{\mathbf{q}\uparrow})\phi_{\mathbf{k},\mathbf{q}} + \frac{g_0}{\mathcal{V}} \sum_{\mathbf{k}'\in\mathcal{B}} \phi_{\mathbf{k}',\mathbf{q}} + \frac{g_0}{\mathcal{V}}\phi_0 - E\phi_{\mathbf{k},\mathbf{q}} = 0 \,. \tag{2.45}$$

From Eq. (2.45) we can write

$$\phi_{\mathbf{k},\mathbf{q}} = -\frac{g_0}{\mathcal{V}} \frac{\phi_0 + \sum\limits_{\mathbf{k}'\in\mathcal{B}} \phi_{\mathbf{k}',\mathbf{q}}}{\epsilon_{\mathbf{k}\uparrow} + \epsilon_{\mathbf{q}-\mathbf{k}\downarrow} - \epsilon_{\mathbf{q}\uparrow} - E} \,, \tag{2.46}$$

and we observe that $\lim\limits_{k\to\infty} \phi_{\mathbf{k},\mathbf{q}} \sim \frac{1}{k^2}$. By applying the summation $\sum\limits_{\mathbf{k}\in\mathcal{B}}$ on both sides of Eq. (2.46), one can rewrite the previous equation as follows:

$$\phi_0 + \sum_{\mathbf{k}\in\mathcal{B}} \phi_{\mathbf{k},\mathbf{q}} = \frac{\phi_0/g_0}{\frac{1}{g_0} + \frac{1}{\mathcal{V}} \sum\limits_{\mathbf{k}\in\mathcal{B}} \frac{1}{\epsilon_{\mathbf{k}\uparrow} + \epsilon_{\mathbf{q}-\mathbf{k}\downarrow} - \epsilon_{\mathbf{q}\uparrow} - E}} \,. \tag{2.47}$$

With the use of Eq. (2.44) we can write

$$E = \frac{1}{\mathcal{V}} \sum_{\mathbf{q}\in\mathcal{B}} \frac{1}{\frac{1}{g_0} + \frac{1}{\mathcal{V}} \sum\limits_{\mathbf{k}\in\mathcal{B}} \frac{1}{\epsilon_{\mathbf{k}\uparrow} + \epsilon_{\mathbf{q}-\mathbf{k}\downarrow} - \epsilon_{\mathbf{q}\uparrow} - E}} \,. \tag{2.48}$$

With Eq. (1.12) the coupling constant g_0 can be substituted in favour of the scattering length a_s and Eq. (2.48) becomes

$$E = \frac{1}{\mathcal{V}} \sum_{\mathbf{q}\in\mathcal{B}} \frac{1}{\frac{m_r}{2\pi a_s} + \frac{1}{\mathcal{V}} \sum\limits_{\mathbf{k}\in\mathcal{B}} \frac{1}{\epsilon_{\mathbf{k}\uparrow} + \epsilon_{\mathbf{q}-\mathbf{k}\downarrow} - \epsilon_{\mathbf{q}\uparrow} - E} - \frac{1}{\mathcal{V}} \sum\limits_{\mathbf{k}\in\mathcal{B}} \frac{2m_r}{k^2}} \,. \tag{2.49}$$

This last expression is well-defined in the continuum limit ($l \to 0$ and $g_0 \to 0^-$ with a_s fixed) and thermodynamic limit. With the use of Eqs. (2.37) and (2.39) we observed that the energy E obtained within the variational approach is identical to the energy $E_{pol}(\mathbf{0})$ obtained from the one-body self-energy $\Sigma^{(1)}(\mathbf{p},\Omega)$. It is also pointed out in [24] that for the Fermi polaron, the energy obtained from the first order of the one-body self-energy in the real-frequency representation equals the energy E. Moreover, we will see in Sec. 3.3 how to construct a one-body self-energy that produces an energy that agrees with the energy obtained with a n p-h variational treatment.

2.6 Constructing higher-order diagrams

We calculated in Sec. 2.4 the one-body self-energy that includes all 1 p-h excitations of the Fermi sea. In this section we consider diagrams with more than one hole propagator. First we

will discuss how the diagrams can be constructed graphically, and second, we will illustrate how an algebraic expression is obtained for each diagram through the Feynman rules.

To construct a diagram for the one-body self-energy at order N, we draw a BBL, which consists out of N grey boxes and $N-1$ straight lines between the boxes (see upper figure in Fig. 2.4). The imaginary time runs from right to left. The left end of each grey box is connected with a directed (forward or backward in time) line which goes to the right end of a grey box (see lower figure in Fig. 2.4). Each directed line covers a part of the BBL. In the end the whole BBL must be covered by such lines. An uncovered piece of the BBL would lead to a one-particle reducible diagram (i.e., a diagram that falls apart if one cuts a single propagator), and we wish to consider only the irreducible diagrams. In the lower figure of Fig. 2.4 we see three of these lines covering the BBL. We identify the different graphical elements:

- The lines above the BBL running from a time τ_1 to a time τ_2 represent the propagators $G^0_\uparrow(\mathbf{q},\tau)$ with $\tau = \tau_2 - \tau_1$. Each line carries a momentum $\mathbf{q}$. If the direction of the line goes forward in time ($\tau > 0$), then $|\mathbf{q}| > k_F$, if the line goes backward in time ($\tau < 0$), then $|\mathbf{q}| < k_F$.

- The grey boxes correspond to dressed interactions $\Gamma^0(\mathbf{k},\tau)$, with momentum $\mathbf{k}$:

$$\mathbf{k} = \mathbf{p} - \sum_i \mathbf{q}_i + \sum_j \mathbf{q}_j \ , \tag{2.50}$$

  with $\mathbf{p}$ the externally incoming momentum of the diagram. The index i runs over all lines that lie above the BBL with momentum $|\mathbf{q}| > k_F$, the index j runs over all above lying lines with momentum $|\mathbf{q}| < k_F$.

- The straight lines of the BBL correspond to a free spin-down propagator $G^0_\downarrow(\mathbf{k},\tau)$ with momentum $\mathbf{k}$ given in Eq. (2.50) and τ the imaginary time during which it propagates.

Since we have one forward propagating impurity, each diagram will have just one BBL. Only the impurity can create p-h excitations, and thus all the $G^0_\uparrow$-propagators will start and end in a Γ^0-interaction of the BBL.

The algebraic value of a particular diagram with fixed internal and external variables corresponds to a product of each of these elements, i.e. a product of free $G^0_\uparrow$ and $G^0_\downarrow$-propagators and dressed interactions Γ^0. The diagram acquires an extra sign $(-1)^{\mathcal{L}}(-1)^N$, with $\mathcal{L}$ the number of fermion loops and N the order of the diagram. As an example, we give the algebraic contribution $\mathcal{D}(\mathcal{T}_A, \mathbf{p}, \tau, \tau_1, \tau_2, \tau_3, \tau_4, \mathbf{q}_1, \mathbf{q}_2, \mathbf{q}_3)$ for the diagram A with topology $\mathcal{T}_A$ (see Fig. 2.4):

$$\begin{aligned}\mathcal{D}(\mathcal{T}_A, \mathbf{p}, \tau, \tau_1, \tau_2, \tau_3, \tau_4, \mathbf{q}_1, \mathbf{q}_2, \mathbf{q}_3) = (-1)^N(-1)^{\mathcal{L}}\frac{1}{(2\pi)^9}\Gamma^0(\mathbf{p}+\mathbf{q}_1, \tau-\tau_4)\\ \times G^0_\downarrow(\mathbf{p}-\mathbf{q}_2+\mathbf{q}_1, \tau_4-\tau_3)\Gamma^0(\mathbf{p}-\mathbf{q}_2+\mathbf{q}_1+\mathbf{q}_3, \tau_3-\tau_2)G^0_\downarrow(\mathbf{p}-\mathbf{q}_2+\mathbf{q}_3, \tau_2-\tau_1)\\ \times\Gamma^0(\mathbf{p}+\mathbf{q}_3, \tau_1)G^0_\uparrow(\mathbf{q}_1, \tau_2-\tau)G^0_\uparrow(\mathbf{q}_2, \tau_4-\tau_1)G^0_\uparrow(\mathbf{q}_3, -\tau_3)\ ,\end{aligned} \tag{2.51}$$

with $N = 3$ and $\mathcal{L} = 1$. Note that we also include a factor $1/(2\pi)^{3N}$ into the definition of $\mathcal{D}$. The algebraic expression for diagram B in Fig. 2.4 reads:

$$\begin{aligned}\mathcal{D}(\mathcal{T}_B, \mathbf{p}, \tau, \tau_1, \tau_2, \tau_3, \tau_4, \mathbf{q}_1, \mathbf{q}_2, \mathbf{q}_3) = (-1)^N (-1)^{\mathcal{L}} \frac{1}{(2\pi)^9} \Gamma^0(\mathbf{p}+\mathbf{q}_1, \tau-\tau_4) \\ \times G^0_\downarrow(\mathbf{p}-\mathbf{q}_2+\mathbf{q}_1, \tau_4-\tau_3)\Gamma^0(\mathbf{p}-\mathbf{q}_2+\mathbf{q}_1+\mathbf{q}_3, \tau_3-\tau_2)G^0_\downarrow(\mathbf{p}-\mathbf{q}_2+\mathbf{q}_1, \tau_2-\tau_1) \\ \times\Gamma^0(\mathbf{p}+\mathbf{q}_1, \tau_1)G^0_\uparrow(\mathbf{q}_1, -\tau)G^0_\uparrow(\mathbf{q}_2, \tau_4-\tau_1)G^0_\uparrow(\mathbf{q}_3, \tau_2-\tau_3)\ ,\end{aligned} \tag{2.52}$$

with $N = 3$ and $\mathcal{L} = 2$. It is clear that the diagrams A and B have an opposite sign due to the different number of loops. These two diagrams are the only possible diagrams at order 3. Diagrams that include ladders (a ladder arises if two subsequent grey boxes are connected with a forward $G^0_\uparrow$-propagator) are not allowed, since all ladder diagrams are already included in Γ^0. According to the Feynman rules [4, 21], we still have to integrate over all internal variables. These variables are the momenta of the $G^0_\uparrow$-propagators and all the internal imaginary times. A schematic representation of the diagrammatic series for the one-body self-energy $\Sigma(\mathbf{p}, \tau)$ looks as follows:

$$\begin{aligned}\Sigma(\mathbf{p}, \tau) = \sum_{N=1}^{\infty} \sum_{\mathcal{T}_N} \int d\mathbf{q_1} \dots d\mathbf{q_i} \dots d\mathbf{q_N} \int d\tau_1 \dots d\tau_i \dots d\tau_{2(N-1)} \\ \times\ \mathcal{D}(\mathcal{T}_N, \mathbf{p}, \tau, \tau_1, \dots, \tau_i, \dots, \tau_{2(N-1)}, \mathbf{q_1}, \dots, \mathbf{q_i}, \dots, \mathbf{q_N})\ ,\end{aligned} \tag{2.53}$$

with $\mathcal{T}_N$ the topology of the diagram of order N. If $N = 1$ there are no internal times.

A similar series expansion can be written down for the two-body self-energy $\Pi(\mathbf{p}, \tau)$. We will see in Sec. 2.8 that this self-energy gives us information about possible bound states of the impurity with a spin-up particle (this composite particle will be called a molecule). The two third-order diagrams for $\Pi(\mathbf{p}, \tau)$ are shown in Fig. 2.5. The diagram order N is here defined as the number of dressed interactions plus one or the number of $G^0_\downarrow$-propagators.

To evaluate $\Sigma(\mathbf{p}, \tau)$ or $\Pi(\mathbf{p}, \tau)$ we need a numerical method that can deal with computing the highly-dimensional integrals (the dimension depends on the diagram order) and summing topologically different diagrams for large diagram orders. Such a method is presented in the next section.

2.7 Summing diagrams with diagrammatic Monte Carlo (DiagMC)

It is known that in many cases a stochastic evaluation of a high-dimensional integral is much more efficient than more systematic methods [25]. Therefore we will evaluate $\Sigma(\mathbf{p}, \tau)$ in a stochastic way with the DiagMC algorithm[22, 26], a method which is designed to evaluate and sum a large number of Feynman diagrams stochastically.

Let us start by introducing the Metropolis algorithm, an importance sampling method [25, 27], which is used in the DiagMC algorithm. Assume one wishes to average a quantity over a large number of configurations. The Monte Carlo method tries to select the most relevant configurations. Typically this finite set of relevant configurations is generated in

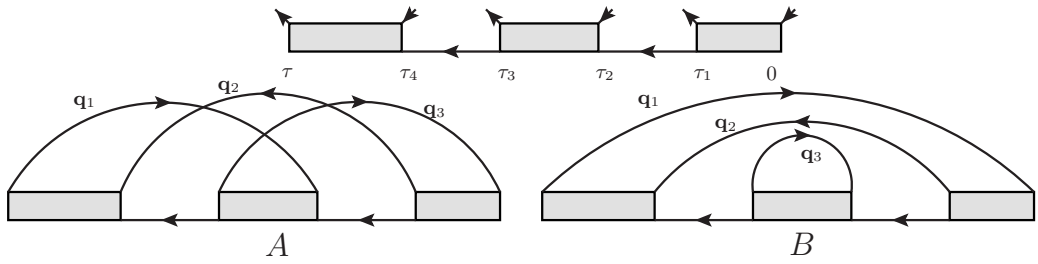

Figure 2.4 – The upper figure shows the backbone of a one-body self-energy diagram at $N = 3$. The imaginary times are ranked as follows: $0 < \tau_1 < \tau_2 < \tau_3 < \tau_4 < \tau$. The lower diagram shows the two different topologies for this order. For both diagrams in the lower figure we have two backward $G^0_\uparrow$-propagator (with momenta $|\mathbf{q}_1| < k_F$ and $|\mathbf{q}_3| < k_F$) and one forward $G^0_\uparrow$-propagator (with momentum $|\mathbf{q}_2| > k_F$).

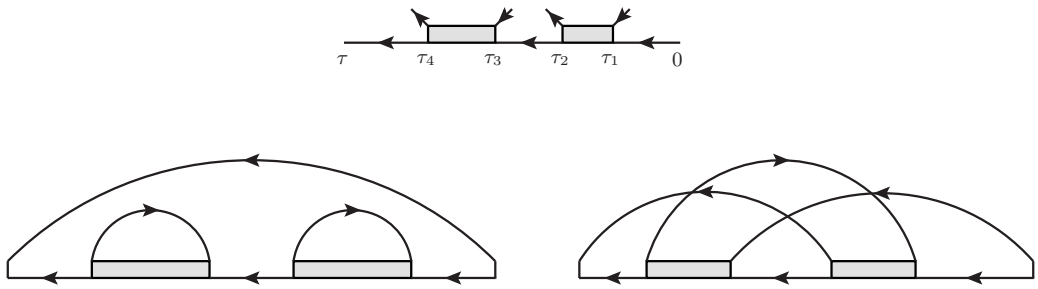

Figure 2.5 – The upper figure shows the backbone of a diagram for the two-body self-energy at $N = 3$. The lower diagram shows the two different topologies for this order. The imaginary times are ranked as follows: $0 < \tau_1 < \tau_2 < \tau_3 < \tau_4 < \tau$.

the form of a Markov chain, in which each new configuration is chosen with a probability depending on the previous one. The detailed balance condition ensures that a certain target distribution will be sampled in the Markov chain. The detailed balance equation for going from a configuration A to a configuration B is written as [25]:

$$\mathcal{P}(A)T_{A\to B} = T_{B\to A}\mathcal{P}(B)\ , \tag{2.54}$$

with $T_{A\to B}$ ($T_{B\to A}$) the transition probability for going from state A to B (B to A). The weight of configuration A (B) is given by $\mathcal{P}(A)$ ($\mathcal{P}(B)$). For practical purposes we write the transition probabilities as

$$T_{A\to B} = W_A(B)P_{A\to B} \tag{2.55}$$

$$T_{B\to A} = W_B(A)P_{B\to A}\ , \tag{2.56}$$

with $W_A(B)$ the proposal distribution that generates a new state B given a state A. The acceptance probability $P_{A\to B}$ in the Metropolis algorithm is given by:

$$P_{A\to B} = \min\left(1, \frac{\mathcal{P}(B)W_B(A)}{\mathcal{P}(A)W_A(B)}\right)\ . \tag{2.57}$$

The new state B, generated from $W_A(B)$, will thus be accepted with a probability $P_{A\to B}$ and rejected with probability $1 - P_{A\to B}$. For $P_{B\to A}$ we get:

$$P_{B\to A} = \min\left(1, \frac{\mathcal{P}(A)W_A(B)}{\mathcal{P}(B)W_B(A)}\right) . \tag{2.58}$$

In the case that $W_A(B) \neq W_B(A)$ one speaks of the generalised Metropolis algorithm [25]. We will define the acceptance ratio q_{acc} for the transition $A \to B$ as

$$q_{acc} = \frac{\mathcal{P}(B)W_B(A)}{\mathcal{P}(A)W_A(B)} . \tag{2.59}$$

The efficiency of a particular algorithm depends on the choice of the proposal probability distributions W, which can be chosen freely. However, it is clear that the efficiency will depend on the overlap of W with $\mathcal{P}$.

In the DiagMC method, the 'configurations' A and B represent the diagram variables of the Feynman diagrams, with an algebraic expression given by $\mathcal{D}(A)$, respectively $\mathcal{D}(B)$ (see Sec. 2.6). The function $\mathcal{D}$ is however not positive definite, since its sign depends, e.g., on the number of fermion loops. Therefore, we choose the weight of 'diagram' A (by diagram we mean a certain topology, order and fixed values of internal and external variables) to be given by $|\mathcal{D}(A)|$. The sign of the diagram is only taken into account when collecting the statistics.

The DiagMC method is designed to evaluate expressions as given in Eq. (2.53). This is done by constructing a set of updates that allow one to sample over all diagram variables. Each update changes one or more diagram variables by using the Metropolis algorithm. For example, we will have updates that perform a change of an imaginary time, the order, the topology, ... One has a lot of freedom to construct a set of updates, as long as each diagram can be reached in a finite time.

To construct a set of updates that allow us to sample diagrams for $\Sigma(\mathbf{p}, \tau)$ and $\Pi(\mathbf{p}, \tau)$ in an efficient way, we extend the space of diagrams with extra, non-physical diagrams. We group different types of diagrams in sectors and in Sec. 2.7.1 it will become clear why these sectors are useful. A schematic overview of the different sectors is given in Fig. 2.6 where we give an example of a diagram for each sector. The $G^0_\downarrow\Sigma$-sector contains diagrams that appear in the series for $\Sigma(\mathbf{p}, \tau)$ with an extra $G^0_\downarrow$-propagator attached. The $\Gamma^0\Pi$-sector contains diagrams that appears in the series for $\Pi(\mathbf{p}, \tau)$ with an extra Γ^0-interaction attached. By removing a $G^0_\uparrow$-propagator from a diagram in the $G^0_\downarrow\Sigma$ or $\Gamma^0\Pi$-sector we obtain a worm diagram. The two ends of the missing $G^0_\uparrow$-propagators are called worm ends. The worm end that is situated on the left side of a Γ^0-interaction is called the outgoing worm end (O), while the other worm end is called the incoming worm end (I). In the Σ and Π-sector we collect statistics for the one and two-body self-energies. The order N of a diagram in the Σ or Π-sector is defined in Sec. 2.6. In the worm, $G^0_\downarrow\Sigma$ and $\Gamma^0\Pi$-sector, a diagram of order N has N $G^0_\downarrow$-propagators and N Γ^0-interactions.

Within each sector we introduce artificial weighting factors $\xi^{(\text{'order'})}_{(\text{'sector'})}$ that depend on the order of the diagrams and on the relevant sectors. These extra factors are used in the DiagMC simulation to control how much simulation time is spent sampling certain sectors or specific orders. For example, good statistics for $\Sigma(\mathbf{p}, \tau)$ and $\Pi(\mathbf{p}, \tau)$ at each order can be accomplished by tuning the weighting factors.

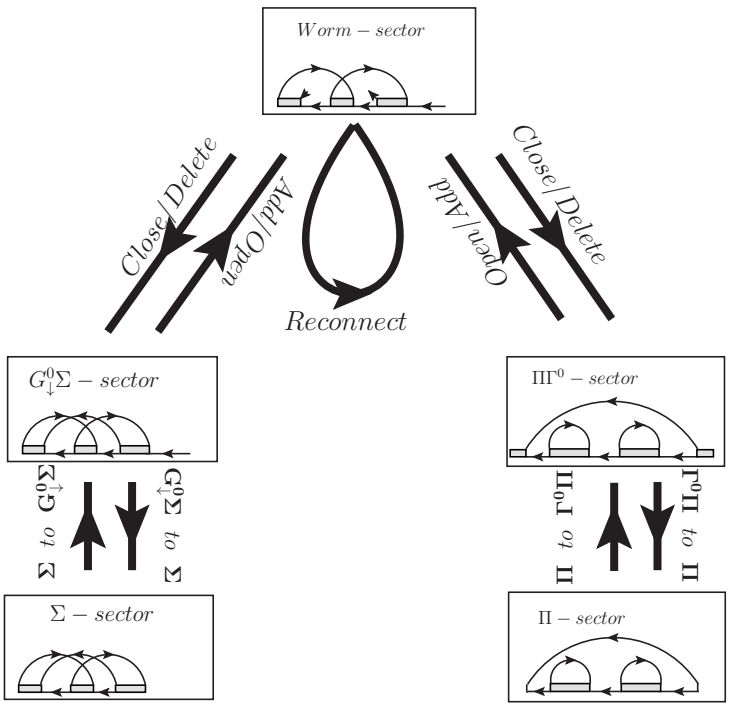

Figure 2.6 – A scheme of the different sectors with an example of a diagram in each sector. The arrows indicate which sectors are connected with each other by means of Monte Carlo updates.

In the following subsections we present the set of updates that we used in the DiagMC simulation. All the updates together meet the requirement of detailed balance and ergodicity. In the presented updates, we will use a cyclic representation for the diagrams. A cyclic diagram can be imagined as a diagram that lies on a circle. This is possible because only time differences are relevant. The total time of the diagram is used when collecting statistics for $\Sigma(\mathbf{p}, \tau)$ or $\Pi(\mathbf{p}, \tau)$.

2.7.1 Updates of the DiagMC algorithm

In the updates we use the convention that imaginary times are always positive for both the particle and the hole propagators. This will simplify our notation. This means that we adopt the following definition of $G^0_\uparrow(\mathbf{k}, \tau)$:

$$\tilde{G}^0_\uparrow(\mathbf{k}, \tau) = -\theta(k - k_F)e^{-(\epsilon_{\mathbf{k}\uparrow} - \epsilon_F)\tau} + \theta(k_F - k)e^{(\epsilon_{\mathbf{k}\uparrow} - \epsilon_F)\tau} \,, \tag{2.60}$$

with always $\tau > 0$. In the remainder of this section, we will denote $\tilde{G}^0_\uparrow(\mathbf{k}, \tau)$ by $G^0_\uparrow(\mathbf{k}, \tau)$.

Time shift

In this update we change the time of a randomly chosen propagator or interaction on the BBL, and the $G^0_\uparrow$-propagators that lie above the chosen line. Let us consider the case where we change the time τ_A of a renormalized interaction $\Gamma^0(\mathbf{p}, \tau_A)$ with momentum $\mathbf{p}$. The acceptance ratio q_{acc} is given by

$$\begin{aligned} q_{acc} &= \frac{|\mathcal{D}(\tau_B)|}{|\mathcal{D}(\tau_A)|} \frac{W_\Gamma(\tau_A)}{W_\Gamma(\tau_B)} \\ &= \left| \frac{\Gamma^0(\mathbf{p}, \tau_B) \prod_i G^0_\uparrow(\mathbf{q}_i, \tau_i + (\tau_B - \tau_A))}{\Gamma^0(\mathbf{p}, \tau_A) \prod_i G^0_\uparrow(\mathbf{q}_i, \tau_i)} \right| \frac{W_\Gamma(\tau_A)}{W_\Gamma(\tau_B)} , \end{aligned} \tag{2.61}$$

where the index i runs over all the above lying $G^0_\uparrow$-propagators with time τ_i and momentum $\mathbf{q}_i$. In the argument of $\mathcal{D}$ we only show the variables relevant for this update. The new time τ_B is chosen according to the probability distribution $W_\Gamma(\tau)$. We have the freedom to choose $W_\Gamma(\tau)$. We want a good overlap with $\mathcal{D}$ such that many proposed times are accepted. In the MC-simulation we keep track of the number of accepted and rejected proposals. This allows us to test the efficiency of different distibutions $W_\Gamma(\tau)$. We found that the following combination of distributions was very efficient: one that resembles Γ^0 supplemented with a uniform distibution. Therefore we write $W_\Gamma(\tau)$ as a linear combination of two different distributions $W_1(\tau)$ and $W_2(\tau)$:

$$W_\Gamma(\tau) = w_1 W_1(\tau) + w_2 W_2(\tau) , \tag{2.62}$$

with w_1 and w_2 the probabilities that a value τ is sampled from $W_1(\tau)$ or $W_2(\tau)$. Our $W_1(\tau)$ and $W_2(\tau)$ are normalized to 1, and $w_1 + w_2 = 1$. We observed that the tail of $\Gamma^0(\mathbf{p}, \tau)$ has an exponential decay for large times: $\Gamma^0(\mathbf{p}, \tau) \overset{\tau \to +\infty}{\sim} e^{-a(\mathbf{p})\tau}$. The coefficients $a(\mathbf{p})$ are determined through a fit before we start the DiagMC simulation. For the probability density $W_1(\tau)$ we take

$$W_1(\tau) \propto \frac{e^{-a(\mathbf{p})\tau}}{\sqrt{\tau}} , \tag{2.63}$$

For short times ($\tau \to 0^+$) one has $\Gamma^0(\mathbf{p}, \tau) \sim \frac{1}{\sqrt{\tau}}$, so $W_1(\tau)$ will capture the short-time behavior of $\mathcal{D}(\tau)$. Times distributed according to $W_1(\tau)$ are generated through

$$\tau_B = \frac{\left(\mathrm{erf}^{-1}(r)\right)^2}{a(\mathbf{p})} , \tag{2.64}$$

with erf^{-1} the inverse error function and r a random number between 0 and 1. For the probability density $W_2(\tau)$ we choose :

$$W_2(\tau) = \frac{1}{|\max(\tau_A - \Delta, 0) - (\tau_A + \Delta)|} , \tag{2.65}$$

with Δ a parameter that determines the range for τ_B: $\tau_B \in [\max(\tau_A - \Delta, 0), (\tau_A + \Delta)]$.

The case where we want to change the time of a $G^0_\downarrow$-propagator can be handled in a similar way with $W_G(\tau) = w_3 W_3(\tau) + w_2 W_2(\tau)$, with $w_3 + w_2 = 1$. We choose

$$W_3(\tau) \propto e^{-\tau(\frac{p^2}{2m_\downarrow} - \mu)} \,. \tag{2.66}$$

Note that μ is a free parameter, which we have introduced in Sec. 2.1. This parameter is the same for every Γ^0-interaction or $G^0_\downarrow$-propagator on the BBL. Since $\mu < -\epsilon_F - \frac{1}{2m_r a_s^2}$ for the renormalized interaction $\Gamma^0(\mathbf{p}, \tau)$ (see sec. Sec. 2.3) Eq. (2.66) is normalizable for all values of $\mathbf{p}$. A value for τ_B can be sampled from $W_3(\tau_B)$ as follows:

$$\tau_B = -\frac{\ln(1-r)}{\frac{p^2}{2m_\downarrow} - \mu} \,. \tag{2.67}$$

Changing the momentum

In this update we choose at random a propagator $G^0_\uparrow(\mathbf{q}_A, \tau)$ and propose to change the momentum $\mathbf{q}_A \to \mathbf{q}_B$, thereby respecting the forward or the backward direction in time. The acceptance ratio q_{acc} is given by

$$\begin{aligned} q_{acc} =& \frac{|\mathcal{D}(\mathbf{q}_B)|}{|\mathcal{D}(\mathbf{q}_A)|} \frac{W^{p,h}(\mathbf{q}_A)}{W^{p,h}(\mathbf{q}_B)} \\ =& \left| \frac{G^0_\uparrow(\mathbf{q}_B, \tau) \prod_i \Gamma^0(\mathbf{p}_i \pm \mathbf{q}_A \mp \mathbf{q}_B, \tau_i) \prod_j G^0_\downarrow(\mathbf{p}_j \pm \mathbf{q}_A \mp \mathbf{q}_B, \tau_j)}{G^0_\uparrow(\mathbf{q}_A, \tau) \prod_i \Gamma^0(\mathbf{p}_i, \tau_i) \prod_j G^0_\downarrow(\mathbf{p}_j, \tau_j)} \right| \\ & \times \frac{W^{p,h}(\mathbf{q}_A)}{W^{p,h}(\mathbf{q}_B)} \,, \end{aligned} \tag{2.68}$$

where the index i (j) runs over the interactions Γ^0 ($G^0_\downarrow$-propagators), with momentum $\mathbf{q}_i$ ($\mathbf{q}_j$) and time τ_i (τ_j), covered by the $G^0_\uparrow$-propagator. The lower (upper) sign is used if $|\mathbf{q}_A| < k_F$ ($|\mathbf{q}_A| > k_F$). For $W^{p,h}(\mathbf{q})d\mathbf{q}$ we choose a distribution that resembles $G^0_\uparrow(\mathbf{q}, \tau)d\mathbf{q}$. If $|\mathbf{q}_A| > k_F$, we choose a new momentum $\mathbf{q}_B$ (with $|\mathbf{q}_B| > k_F$) with probability $W^p(\mathbf{q}_B)d\mathbf{q}_B = W(\theta, \phi)W^p(|\mathbf{q}_B| = q)dqd\theta d\phi$, with (q, θ, ϕ) a set of spherical coordinates and with

$$W(\theta, \phi) = \frac{\sin(\theta)}{4\pi} \,, \tag{2.69}$$

$$W^p(q) = \frac{q^2 e^{-\tau \frac{q^2}{2m_\uparrow}}}{\int_{k_F}^\infty dq \;\; q^2 e^{-\tau \frac{q^2}{2m_\uparrow}}} \,. \tag{2.70}$$

Since we cannot sample from $W^p(q)$ directly, we instead sample from the distribution (which can be handled more easily numerically):

$$W^p(q) = \frac{q_i^2 e^{-\tau_j \frac{q_i^2}{2m_\uparrow}}}{\sum_{k=0}^{N_q - 1} q_k^2 e^{-\tau_j \frac{q_k^2}{2m_\uparrow}} \Delta_k} \qquad \text{for} \;\; q \in [q_i, q_i + \Delta_i] \;\; \text{and} \;\; i = 0, \ldots, (N_q - 1) \,, \tag{2.71}$$

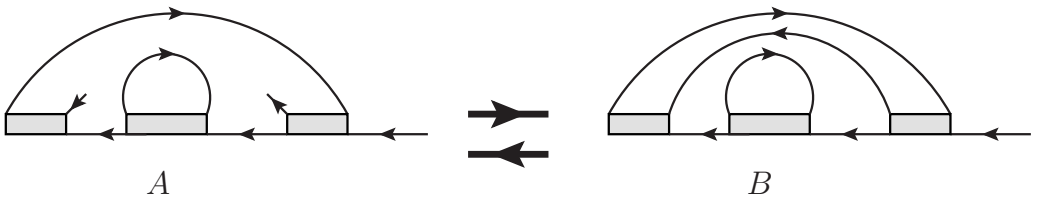

Figure 2.7 – The close-update ($A \to B$) changes in this particular example a worm diagram into a $G^0_\downarrow\Sigma$-diagram by connecting the worm ends with a $G^0_\uparrow$-propagator. The open-update ($B \to A$) removes a forward $G^0_\uparrow$-propagator, thereby changing a $G^0_\downarrow\Sigma$-diagram into a worm diagram.

with q_i a finite number of discrete q-values:

$$q_i = k_F + \sum_{j=0}^{i-1} \Delta_j \qquad \text{for} \quad i = 0, \ldots, (N_q - 1) \,, \tag{2.72}$$

and with the Δ_i a set of chosen mesh sizes and N_q the number of mesh points. This distribution is tabulated for a finite number of imaginary time values τ_j, and we sample from the tabulated distribution with τ_j closest to the τ from the chosen $G^0_\uparrow$-propagator. In practice, we first choose a discrete q_i from a tabulated distribution $W^p_{dis}(q_i)$:

$$W^p_{dis}(q_i) = \frac{q_i^2 e^{-\tau_j \frac{q_i^2}{2m_\uparrow}} \Delta_i}{\sum_{k=0}^{N_q - 1} q_k^2 e^{-\tau_j \frac{q_k^2}{2m_\uparrow}} \Delta_k} \,. \tag{2.73}$$

A value for q_B is then chosen uniformly in the range $[q_i, q_i + \Delta_i]$.

In the case $|\mathbf{q}_A| < k_F$, we choose $\mathbf{q}_B (|\mathbf{q}_B| < k_F)$ with probability $W^h(\mathbf{q}_B) d\mathbf{q}_B = W(\theta, \phi) W^h(q = |\mathbf{q}_B|) dq d\theta d\phi$. We take $W^h(q) \propto q e^{\frac{\tau}{2m_\uparrow} q^2}$, and use

$$q = \sqrt{\frac{\ln(1 + r e^{\frac{\tau}{2m_\uparrow} k_F^2} - r)}{\frac{\tau}{2m_\uparrow}}} \,, \tag{2.74}$$

to generate a new value for q.

Open and Close

The close-update transforms a worm diagram into a $G^0_\downarrow\Sigma$-diagram or a $\Gamma^0\Pi$-diagram by connecting the worm ends with a $G^0_\uparrow$-propagator. The open-update removes a random $G^0_\uparrow$-propagator and changes a $G^0_\downarrow\Sigma$-diagram or a $\Gamma^0\Pi$-diagram into a worm diagram (see Fig. 2.7 for an example). For close, we choose with equal probability that the new $G^0_\uparrow$-propagator goes forward in time or backward in time. The momentum $\mathbf{q}$ of the new $G^0_\uparrow$-propagator can then be chosen with the same probability density $W^{p,h}(\mathbf{q})$ that was used in the previous

update. The $G^0_\uparrow$-propagator to be removed in the open-update is chosen at random. The acceptance ratio q_{acc} for the close-update is given by:

$$\begin{aligned} q_{acc} &= \frac{|\mathcal{D}(B)|}{|\mathcal{D}(A)|}\frac{W_N}{W(\mathbf{q})} \\ &= \frac{1}{(2\pi)^3}\left|\frac{G^0_\uparrow(\mathbf{q},\sum_i \tau_i + \sum_j \tau_j)\prod_i \Gamma^0(\mathbf{p}_i \mp \mathbf{q},\tau_i)\prod_j G^0_\downarrow(\mathbf{p}_j \mp \mathbf{q},\tau_j)}{\prod_i \Gamma^0(\mathbf{p}_i,\tau_i)\prod_j G^0_\downarrow(\mathbf{p}_j,\tau_j)}\right| \\ &\times \frac{1/N}{\frac{1}{2}W^{p,h}(\mathbf{q})}\frac{\xi^{(N)}_{\mathcal{S}}}{\xi^{(N)}_{worm}}\,, \end{aligned} \tag{2.75}$$

with the sector $\mathcal{S}$ equal to $G^0_\downarrow\Sigma$ or $\Gamma^0\Pi$, $W_N = 1/N$,$W(\mathbf{q}) = \frac{1}{2}W^{p,h}(\mathbf{q})$ and the index i (j) runs over the Γ^0-interactions ($G^0_\downarrow$-propagators) for which the number of $G^0_\uparrow$-propagators that lie above will change. The lower (upper) sign is used if the new $G^0_\uparrow$-propagator goes backward (forward) in time. The $\frac{1}{2}$ in front of $W^{p,h}(\mathbf{q})$ comes from the fact that we choose with equal probability a direction in time. The newly created diagram should have exactly one uncovered $G^0_\downarrow$-propagator (in this case we have a $G^0_\downarrow\Sigma$-diagram) or exactly one uncovered Γ^0-interaction (in this case we have a $\Gamma^0\Pi$-diagram). All other cases will not lead to a $G^0_\downarrow\Sigma$-diagram or a $\Gamma^0\Pi$-diagram and the close-update should be rejected. The acceptance ratio q_{acc} for the open-update becomes:

$$\begin{aligned} q_{acc} &= \frac{|\mathcal{D}(A)|}{|\mathcal{D}(B)|}\frac{W(\mathbf{q})}{W_N} \\ &= \left|\frac{(2\pi)^3\prod_i \Gamma^0(\mathbf{p}_i \pm \mathbf{q},\tau_i)\prod_j G^0_\downarrow(\mathbf{p}_j \pm \mathbf{q},\tau_j)}{G^0_\uparrow(\mathbf{q},\sum_i \tau_i + \sum_j \tau_j)\prod_i \Gamma^0(\mathbf{p}_i,\tau_i)\prod_j G^0_\downarrow(\mathbf{p}_j,\tau_j)}\right| \\ &\times \frac{1}{2}\frac{W^{p,h}(\mathbf{q})}{1/N}\frac{\xi^{(N)}_{worm}}{\xi^{(N)}_{\mathcal{S}}}\,. \end{aligned} \tag{2.76}$$

The lower (upper) sign is used if the $G^0_\uparrow$-propagator which is removed goes backward (forward) in time.

The sign of the worm diagrams can be chosen arbitrary since these diagrams are unphysical. We choose their sign to be the same as when the worm ends would be closed with a backward moving $G^0_\uparrow$-propagator. It is important that, with this convention, the sign coming from the number of loops is not changed by the open/close-updates

Reconnect

This update applies only to diagrams in the worm sector and allows one to change the topology of the diagram while the diagram order remains the same. In Reconnect we swap the outgoing worm end (O) with the outgoing end of a randomly chosen $G^0_\uparrow$-propagator that carries momentum $\mathbf{q}$. If the update proposes to change the time direction of the $G^0_\uparrow$-propagator, the update is rejected. We distinguish between two situations. In the first

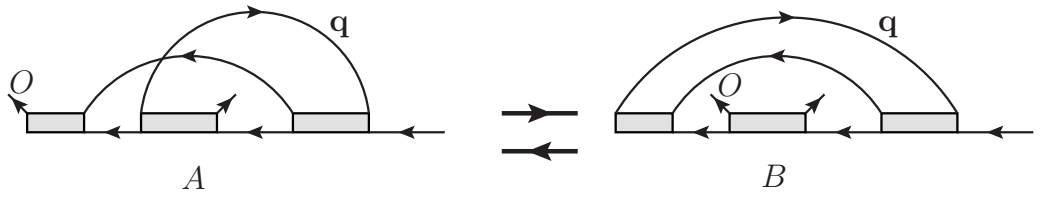

Figure 2.8 – Changing the topology of a diagram with the reconnect-update. The end of a backward $G^0_\uparrow$-propagator with momentum $\mathbf{q}$ ($|\mathbf{q}| < k_F$) is swapped with the outgoing worm end O.

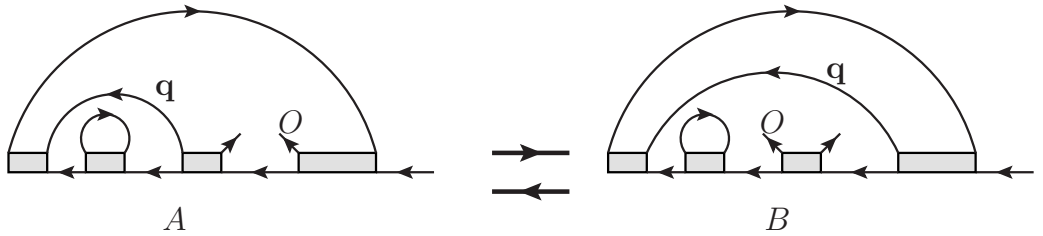

Figure 2.9 – Changing the topology of a diagram with the reconnect-update. The end of a forward $G^0_\uparrow$-propagator with momentum $\mathbf{q}$ ($|\mathbf{q}| > k_F$) is swapped with the outgoing worm end O.

case, the outgoing worm end is not covered by the $G^0_\uparrow$-propagator. Diagrams A in Figs. 2.8 and 2.9 are examples of this. In the second case, the outgoing worm end is covered by the $G^0_\uparrow$-propagator. This situation applies to diagrams B in Figs. 2.8 and 2.9. The acceptance ratio q_{acc} for the first case (for going from A to B in Figs. 2.8 and 2.9) is given by

$$\begin{aligned} q_{acc} &= \frac{|\mathcal{D}(B)|}{|\mathcal{D}(A)|} \\ &= \left| \frac{G^0_\uparrow(\mathbf{q}, \sum_j \tau_j + \sum_i \tau_i) \prod_i \Gamma^0(\mathbf{p}_i \mp \mathbf{q}, \tau_i) \prod_j G^0_\downarrow(\mathbf{p}_j \mp \mathbf{q}, \tau_j)}{\prod_i \Gamma^0(\mathbf{p}_i, \tau_i) \prod_j G^0_\downarrow(\mathbf{p}_j, \tau_j)} \right| . \end{aligned} \tag{2.77}$$

The index i (j) runs over the renormalized interactions Γ^0 ($G^0_\downarrow$-propagators) for which the number of above lying $G^0_\uparrow$-propagators increases. The lower (upper) sign is used if $|\mathbf{q}| < k_F$ ($|\mathbf{q}| > k_F$).

For the second case (going from B to A in Figs. 2.8 and 2.9) the acceptance ratio q_{acc} becomes:

$$\begin{aligned} q_{acc} &= \frac{|\mathcal{D}(A)|}{|\mathcal{D}(B)|} \\ &= \left| \frac{\prod_i \Gamma^0(\mathbf{p}_i \pm \mathbf{q}, \tau_i) \prod_j G^0_\downarrow(\mathbf{p}_j \pm \mathbf{q}, \tau_j)}{G^0_\uparrow(\mathbf{q}, \sum_j \tau_j + \sum_i \tau_i) \prod_i \Gamma^0(\mathbf{p}_i, \tau_i) \prod_j G^0_\downarrow(\mathbf{p}_j, \tau_j)} \right| . \end{aligned} \tag{2.78}$$

The index i (j) runs over the renormalized interactions Γ^0 ($G^0_\downarrow$-propagators) for which the number of $G^0_\uparrow$-propagators lying above decreases. The lower (upper) sign is used if $|\mathbf{q}| < k_F$ ($|\mathbf{q}| > k_F$).

The update is always rejected if the new diagram is a fully closed diagram which is a diagram with zero uncovered Γ^0-interactions and $G^0_\downarrow$-propagators. We impose this additional constraint to optimise the simulation. The fully closed diagrams have a large weight compared to the other diagrams, and therefore we wish to avoid those diagrams which do not contribute to the self-energy anyway. Note that even with the exclusion of these diagrams the simulation stays ergodic.

In the reconnect-update the number of loops changes with one, which has to be taken into account when keeping track of the sign of the diagram.

Add and delete

In the add-update a Γ^0-interaction (with momentum $\mathbf{p}$ and time τ_1) with worm ends and a $G^0_\downarrow$-propagator (with momentum $\mathbf{p}$ and time τ_2) are attached to the uncovered propagator of a $G^0_\downarrow\Sigma$-diagram or to the uncovered Γ^0-interaction of a $\Gamma^0\Pi$-diagram (see Fig. 2.10). The newly created diagram will be a worm diagram. The times τ_1 and τ_2 are chosen with probability densities $W_\Gamma(\tau_1)$ and $W_G(\tau_2)$, respectively. The acceptance ratio q_{acc} is given by

$$\begin{aligned} q_{acc} =& \frac{|\mathcal{D}(B)|}{|\mathcal{D}(A)|} \frac{1}{W_\Gamma(\tau_1) W_G(\tau_2)} \\ =& \left| \frac{\Gamma^0(\mathbf{p},\tau_1) G^0_\downarrow(\mathbf{p},\tau_2)}{W_\Gamma(\tau_1) W_G(\tau_2)} \right| \frac{\xi^{(N+1)}_{\text{worm}}}{\xi^{(N)}_{\mathcal{S}}} , \end{aligned} \tag{2.79}$$

with $\mathcal{S} = G^0_\downarrow\Sigma$ or $\mathcal{S} = \Gamma^0\Pi$. We distinguish between two different cases where the delete-update is applicable. In the first case we consider a diagram with exactly one uncovered Γ^0-interaction and two uncovered $G^0_\downarrow$-propagators. The worm ends should be on the Γ^0-interaction. By removing this Γ^0-interaction and the $G^0_\downarrow$-propagator to the right of the Γ^0-interaction we arrive at a $G^0_\downarrow\Sigma$-diagram (see upper figure in Fig. 2.10). In the second case we consider a diagram with exactly two uncovered Γ^0-interactions and one uncovered $G^0_\downarrow$-propagator. The incoming worm should be on the left Γ^0-interaction with respect to the uncovered $G^0_\downarrow$-propagator. The outgoing worm should be on the right Γ^0-interaction with respect to the uncovered $G^0_\downarrow$-propagator. By removing the uncovered $G^0_\downarrow$-propagator and the Γ^0-interaction on the right we get a $\Gamma^0\Pi$-diagram (see lower figure Fig. 2.10). The acceptance ratio q_{acc} then reads

$$\begin{aligned} q_{acc} =& \frac{|\mathcal{D}(A)|}{|\mathcal{D}(B)|} W_\Gamma(\tau_1) W_G(\tau_2) \\ =& \left| \frac{W_\Gamma(\tau_1) W_G(\tau_2)}{\Gamma^0(\mathbf{p},\tau_1) G^0_\downarrow(\mathbf{p},\tau_2)} \right| \frac{\xi^{(N-1)}_{\mathcal{S}}}{\xi^{(N)}_{\text{worm}}} . \end{aligned} \tag{2.80}$$

If the new diagram is a $G^0_\downarrow\Sigma$-diagram we get an extra minus sign from the increase/decrease in order and another minus sign is coming from the addition/removal of the fermion loop

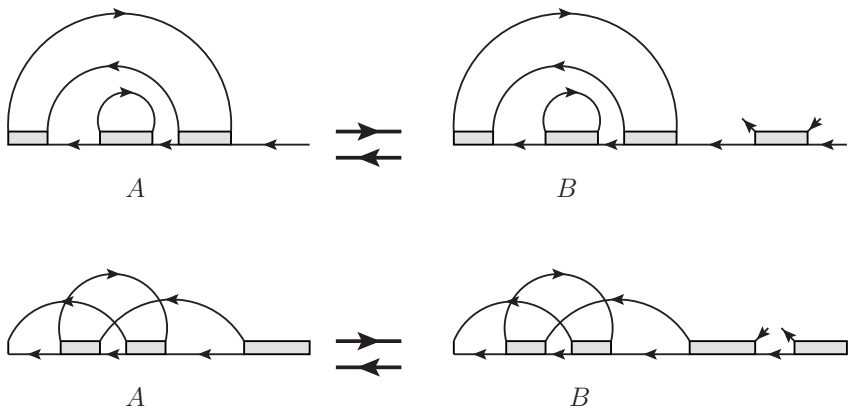

Figure 2.10 – The upper figure shows a $G^0_\downarrow\Sigma$-diagram (A) that is transformed into a worm diagram (B) by attaching a $G^0_\downarrow$-propagator and a Γ^0-interaction to the uncovered $G^0_\downarrow$-propagator. On the lower figure a $G^0_\downarrow$-propagator and a Γ^0-interaction are attached to the uncovered Γ^0-interaction of a $\Gamma^0\Pi$-diagram (A) that is transformed into a worm diagram (B) .

(due to our convention of the sign of a worm diagram). In the case we are dealing with a $\Gamma^0\Pi$-diagram there is no change of loops in the add/delete-updates, so an extra minus due to the change of order has to be considered when keeping track of the sign of the contribution.

$G^0_\downarrow\Sigma$ to Σ and Σ to $G^0_\downarrow\Sigma$ update

A $G^0_\downarrow\Sigma$-diagram (A) is transformed into a Σ-diagram (B) and vice versa. If we want to calculate the ground-state properties of the polaron later, we will need $\Sigma(\mathbf{p},\tau,E)$ with E the ground-state energy of the polaron, which is obtained as follows:

$$\Sigma(\mathbf{p},\tau,E) = \Sigma(\mathbf{p},\tau,\mu)e^{-(\mu-E)\tau} \ . \tag{2.81}$$

If we collect statistics for $\Sigma(\mathbf{p},\tau,\mu)$ and μ is for example much smaller than E, then it is clear that the statistical noise for large times will be amplified by applying Eq. (2.81). Let us denote the value of μ in the Σ-sector by μ_Σ. Although E is a priori unknown, its value can be estimated at the beginning of the simulation, and we take $\mu_\Sigma \approx E$ for the diagrams in the Σ-sector. However, we cannot use this value for μ in all the sectors since some integrals over the internal variables might diverge for this particular choice, $\mu = \mu_\Sigma$.

In the Σ-sector the uncovered $G^0_\downarrow$-propagator is removed. This allows us to directly measure $\Sigma(\mathbf{p},\tau)$ (see also Sec. 2.7.2). In the Σ-sector we can change μ with μ_Σ, which has the advantage that it will not amplify the statistical noise too much if we calculate $\Sigma(\mathbf{p},\tau,E)$ with Eq. (2.81).

The acceptance ratio q_{acc} for $A \to B$ is

$$\begin{aligned} q_{acc} &= \frac{|\mathcal{D}(B)|}{|\mathcal{D}(A)|} \\ &= \frac{e^{(\mu_\Sigma - \mu)\tau}}{|G^0_\downarrow(\mathbf{p}_0, \tau_0, \mu)|} \frac{\xi^{(N)}_\Sigma}{\xi^{(N)}_{G^0_\downarrow \Sigma}} , \end{aligned} \tag{2.82}$$

with $G^0_\downarrow(\mathbf{p}_0, \tau_0, \mu)$ the uncovered propagator for the $G^0_\downarrow\Sigma$-diagram.

$\Gamma^0\Pi$ to Π and Π to $\Gamma^0\Pi$ update

A $\Gamma^0\Pi$-diagram (A) is transformed into a Π-diagram (B) and vice versa. This update is very similar to the previous one and is used to obtain good statistics for $\Pi(\mathbf{p}, \tau, E)$ with E the ground-state energy of the molecule. We change $\mu \to \mu_\Pi$ when we go to the Π-sector, with μ_Π a value close to E. The acceptance ratio q_{acc} for $A \to B$ is:

$$\begin{aligned} q_{acc} &= \frac{|\mathcal{D}(B)|}{|\mathcal{D}(A)|} \\ &= \frac{e^{(\mu_\Pi - \mu)\tau}}{|\Gamma^0(\mathbf{p}_0, \tau_0, \mu)|} \frac{\xi^{(N)}_\Pi}{\xi^{(N)}_{\Gamma^0 \Pi}} , \end{aligned} \tag{2.83}$$

with $\Gamma^0(\mathbf{p}_0, \tau_0, \mu)$ the uncovered Γ^0-interaction of the $\Gamma^0\Pi$-diagram. The number of loops changes since a loop is removed by removing the Γ^0-interaction.

2.7.2 Making a random walk in the configuration space of diagrams

We illustrate in this section how the updates generate a Markov chain of diagrams. For each sector we have a set of possible updates, and we apply one at random. In Fig. 2.11 we show an example of a random sequence of diagrams that could be generated with DiagMC. Note that the external momentum $\mathbf{p}$ of the diagram is kept fixed during the simulation. For each sampled Σ-diagram (Π-diagram) with total time τ we add a number $s = \frac{1}{\xi^{(N)}_\mathcal{S}}$ with $\mathcal{S} = \Sigma$ or $\mathcal{S} = \Pi$ to the applicable time bin of a time-histogram Σ^{MC} or Π^{MC}. After the simulation we can calculate $\Sigma(\mathbf{p}, \tau)$ and $\Pi(\mathbf{p}, \tau)$. To normalize Σ^{MC} (Π^{MC}) we use the first-order worm diagram as a normalization diagram. The number $n^{(1)}$ of times the first-order worm diagram is sampled corresponds to a value which can be easily computed. The properly normalized self-energy $\Sigma(\mathbf{p}, \tau)$ is given by:

$$\Sigma(\mathbf{p}, \tau) = \frac{\Sigma^{MC}(\mathbf{p}, \tau_i)}{n^{(1)} \Delta\tau_i} \xi^{(1)}_{worm} \int_0^\infty d\tau \int_0^\tau d\tau_1 \Gamma^0(\mathbf{p}, \tau - \tau_1) G^0_\downarrow(\mathbf{p}, \tau_1) , \tag{2.84}$$

with $\Delta\tau_i$ the binsize of bin i with time τ_i.

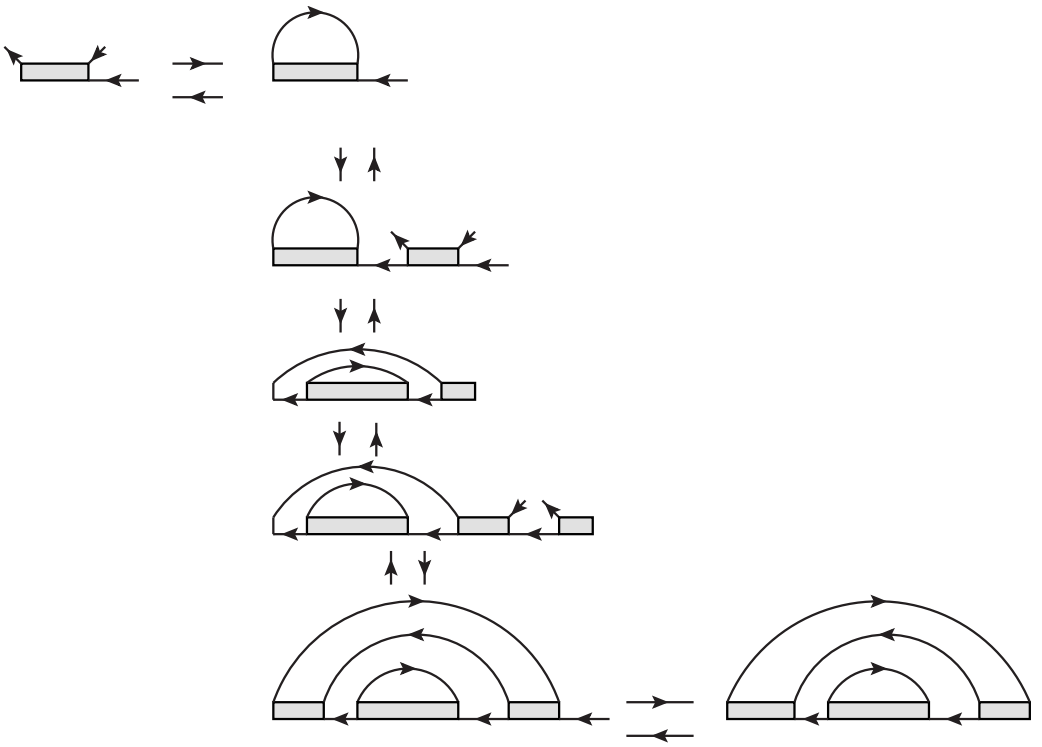

Figure 2.11 – Example of a random walk through the configuration space of diagrams. Starting in the upper left corner and following the forward direction of the arrows, the walk goes through the following sectors: Worm sector $\rightarrow$ $G^0_\downarrow\Sigma$-sector $\rightarrow$ worm sector $\rightarrow$ $G^0_\downarrow\Sigma$-sector $\rightarrow$ worm sector $\rightarrow$ $G^0_\downarrow\Sigma$-sector $\rightarrow$ Σ-sector. For the same direction the following updates are used: Close $\rightarrow$ add $\rightarrow$ close $\rightarrow$ add $\rightarrow$ close $\rightarrow$ $G^0_\downarrow\Sigma$ to Σ. Note that we made use of the cyclic representation of the diagrams.

In Fig. 2.12 and Fig. 2.13 we show the contribution of each order to the one-body self-energy for $k_F a_s = 1$. At an order N_{max} the noise will dominate over the signal given a certain simulation time. The factorial increase of diagrams will nearly limit N_{max}. The different signs of the diagrams, on the other hand, will have a big impact on N_{max}. For example: the two diagrams that contribute to the third-order self-energy have an opposite sign and cancel each other almost (see Sec. 2.6). Even though there are only two diagrams, it requires considerable computational effort to see this cancellation and to calculate $\Sigma^{N=3}(\mathbf{p} = \mathbf{0}, \tau)$ accurately. We observe that $\Sigma^N(\mathbf{p} = \mathbf{0}, \tau)$ starts oscillating as function of the diagram order and seems to diverge. For orders larger than 9, $\Sigma^N(\mathbf{p} = \mathbf{0}, \tau)$ has a bad signal-to-noise ratio, due to our finite simulation time, and therefore we do not go beyond N_{max}.

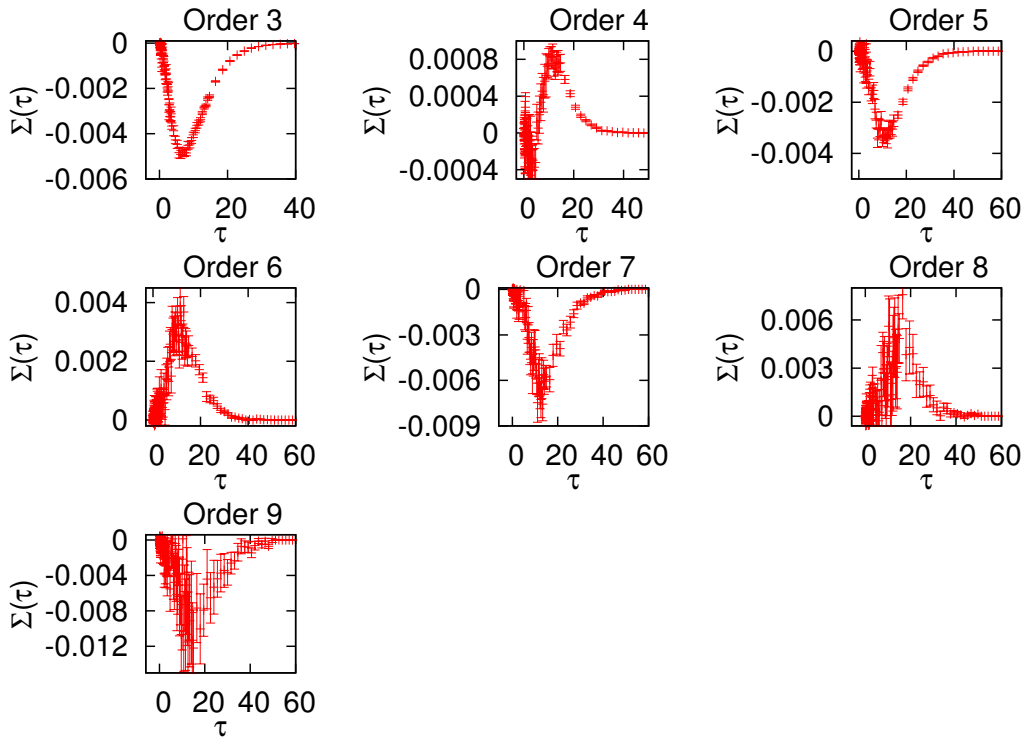

Figure 2.12 – The one-body self-energy $\Sigma^N(\mathbf{p}=\mathbf{0},\tau)$ as function of τ for different orders N for $k_F a_s = 1$ and $\mu = -1.22$.

2.8 Quasiparticle properties of an impurity in a Fermi gas

This section contains the published results of the 3D Fermi polaron [28]. First we will discuss some relevant properties of the self-energies $\Sigma^N(\mathbf{p},\tau)$ and $\Pi^N(\mathbf{p},\tau)$, which are calculated with the DiagMC method. In the previous section we observed that $\Sigma^N(\mathbf{p},\tau)$ oscillates and diverges as a function of N. This scenario raises the question: how can one extract physically relevant information from such an expansion for the one-body self-energy? We will show in this section that a sign-alternating series, even if it is divergent, can be re-summed.

At first sight it might seem plausible that one gets more accurate results if more diagrams are taken into account. This could be done by dressing some lines in the diagrams. Dressing can be achieved by summing a subseries of diagrams. In fact, we already have summed up such a subseries, namely the ladder diagrams in the renormalized interaction. This summation was physically motivated, and it was necessary in our procedure to renormalize the contact interaction. Let us give another example. Take the Green's function defined by $G^1_\downarrow(\mathbf{p},\tau) = G^0_\downarrow(\mathbf{p},\tau) + G^0_\downarrow(\mathbf{p},\tau)\Sigma^{(1)}(\mathbf{p},\tau)G^1_\downarrow(\mathbf{p},\tau)$ (see Sec. 2.4 for the definition of $\Sigma^{(1)}(\mathbf{p},\tau)$). Let us call $G^0_\downarrow$ and Γ^0 the 'bare propagators'. Propagators that include more diagrams will

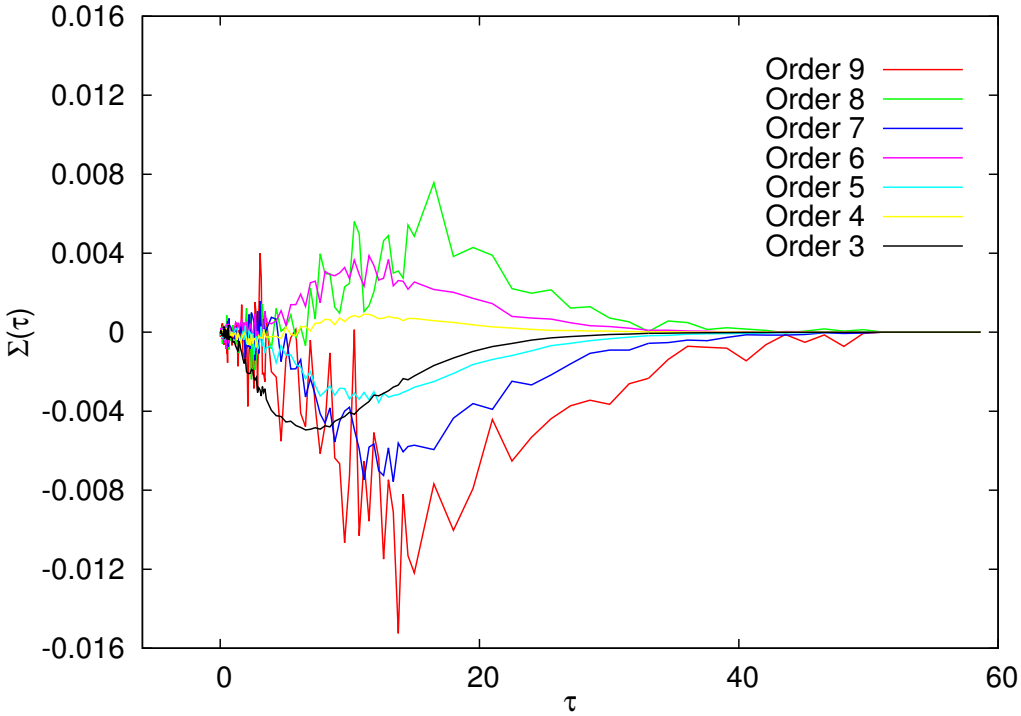

Figure 2.13 – The one-body self-energy $\Sigma^N(\mathbf{p}=\mathbf{0},\tau)$ as function of τ for different orders N for $k_F a_s = 1$ and $\mu = -1.22$.

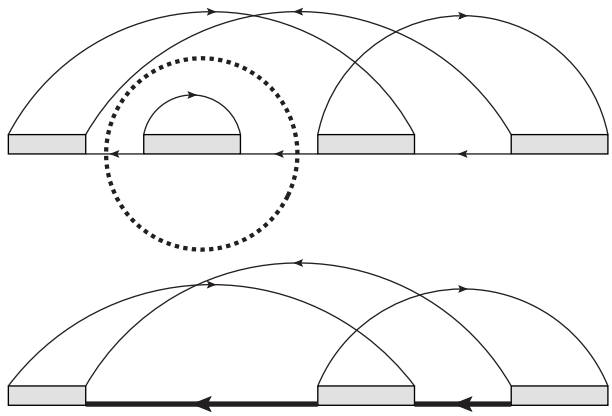

Figure 2.14 – The upper diagram shows a fourth-order Σ-diagram which contains a first-order subdiagram in the dashed circle. In the lower diagram the $G^0_\downarrow$-propagators are replaced by $G^1_\downarrow$-propagators (bold lines) and the upper diagram is included implicitly.

be called dressed or bold propagators. In the DiagMC simulation we could for example replace all $G^0_\downarrow$ with the dressed $G^1_\downarrow$. From Fig. 2.14 it is clear that diagrams which contain a first-order diagram as a subdiagram have to be excluded to avoid double counting. In this way an infinite subset of diagrams is included in each diagram in an implicit way.

We will discuss more advanced schemes and see that taking into account more diagrams does not always lead to better and more accurate results. We will look at different schemes to calculate the ground-state properties for the polaron and the molecule to check the robustness of the results.

Quasiparticle properties of an impurity in a Fermi gas

Jonas Vlietinck[1], Jan Ryckebusch[1], and Kris Van Houcke[1]

[1] *Department of Physics and Astronomy, Ghent University, Proeftuinstraat 86, 9000 Gent, Belgium*

Abstract

We report on a study of a spin-down impurity strongly coupled to a spin-up Fermi sea (a so-called Fermi polaron) with the diagrammatic Monte-Carlo (DiagMC) technique. Conditions of zero temperature and three dimensions are considered for an ultracold atomic gas with resonant interactions in the zero-range limit. A Feynman diagrammatic series is developed for the one-body and two-body propagators providing information about the polaron and molecule channel respectively. The DiagMC technique allows us to reach diagram orders that are high enough for extrapolation to infinite order. The robustness of the extracted results is examined by checking various resummation techniques and by running the simulations with various choices for the propagators and vertex functions. It turns out that dressing the lines in the diagrams as much as possible is not always the optimal choice. We also identify classes of dominant diagrams for the one-body and two-body self-energy in the region of strong interaction. These dominant diagrams turn out to be the leading processes of the strong-coupling limit. The quasiparticle energies and Z-factor are obtained as a function of the interaction strength. We find that the DiagMC results for the molecule and polaron properties are very similar to those obtained with a variational ansatz. Surprisingly, this variational ansatz gives very good predictions for the quasiparticle residue even when this residue is significantly smaller than one.

1 Introduction

The notion of a 'bare' particle loses its significance once it is strongly coupled to a medium. Landau introduced the notion of a quasiparticle whose properties may be very different from those of a bare particle [1][1]. The most prominent example is an electron moving in a crystal: the electron displaces the nearby ions and carries this distortion with it. The presence of the phonon cloud changes the mass and energy of the electron, that is dubbed as 'polaron' [2]. More generally, a polaron arises whenever a quantum impurity is strongly coupled to an environment. These quantum-mechanical quasiparticles play a key role in the low-energy behavior of a macroscopic quantum liquid.

In recent years, the field of ultracold atoms has provided an exciting framework for studying polaronic effects. A key idea is that models designed for describing the rich and non-trivial structure of the solid state, can be emulated in a clean and controllable manner with ultracold atoms. For example, so-called Fermi polarons [3, 4, 5], spin-down impurities that are strongly

[1] The references of the citations in this text are located at the end of this chapter

coupled to a spin-up Fermi sea, can be created in a degenerate two-component atomic Fermi gas when going to the limit of strong spin-imbalance close to a Feshbach resonance. The impurity is coherently dressed with particle-hole excitations of the Fermi sea. The properties of the Fermi polaron are important for the quantitative understanding of a strongly imbalanced Fermi gas [6].

In this paper, we focus on the 'attractive Fermi polaron', with an attractive interaction between the impurity and the fermions of the bath. A recent experiment using an ultracold gas of ^{6}Li atoms in three dimensions revealed the existence of Fermi polarons through a narrow quasiparticle peak in the impurities' radio-frequency (rf) spectrum [4]. At a critical interaction strength, the disappearance of this peak was interpreted as a transition from polaronic to molecular binding, when the impurity and an atom of the sea form a two-body bound state. Such a transition had theoretically been predicted in three dimensions (3D) by Prokof'ev and Svistunov [3]. To determine the transition point, they developed a diagrammatic Monte Carlo technique (DiagMC) capable of solving the Fermi polaron model[3, 8]. Calculations of the ground-state energy showed that for a sufficiently strong attraction between the impurity atom and the atoms of the spin-up Fermi sea, a molecular state becomes energetically favorable. The crossing point was found at an interaction strength $(k_F a)_c = 1.11(2)$, with k_F the Fermi momentum of the spin-up sea and a the s-wave scattering length. A variational treatment developed by Chevy based on an expansion up to single particle-hole excitations on top of the unperturbed Fermi sea turned out to be remarkably accurate [9]. A combination of Chevy's ansatz with a variational wave function in the molecular limit [10, 11, 12] also revealed the polaron-to-molecule transition, very close to the DiagMC result.

In the present work, we study the quasiparticle properties of the Fermi polaron problem in 3D with the DiagMC technique [3, 8]. This technique evaluates a series of Feynman diagrams for the one-particle and two-particle proper self-energies. A full description of the DiagMC algorithm was presented in Ref. [8]. Building on the work of Ref. [8] we have implemented the DiagMC algorithm independently. We explore various DiagMC schemes [13] and series resummation methods to check the robustness of the results against the possible uncertainties of summing the series. First, we confirm the transition point. Next, we calculate the quasiparticle residue which we compare to experimental data and variational results. The quasiparticle residue, or Z-factor, gives the overlap of the non-interacting wave function and the fully interacting one,

$$Z_p = |\langle \Psi_0^{N_\uparrow} | \mathbf{0}_\downarrow, FS(N_\uparrow)\rangle|^2 \,, \tag{1}$$

with $|\Psi_0^{N_\uparrow}\rangle$ the fully interacting ground state and $|\mathbf{0}_\downarrow, FS(N_\uparrow)\rangle$ a free spin-down atom carrying momentum $\mathbf{p} = \mathbf{0}$ in a non-interacting Fermi sea FS of $N_\uparrow$ spin-up atoms. The spin-up atoms are non-interacting since p-wave scattering is negligible. The residue reflects the impurity's probability of free propagation.

The outline of the paper is as follows. In Section 2 we introduce the model and the structure of the Feynman diagrammatic expansion. In Section 3 we discuss the results of the numerical calculations. Thereby, we investigate on how the results depend on the choices made with regard to the diagrammatic series, like the use of bare versus dressed propagators. Also the resummation of the diagrammatic series is discussed in depth. The results for the quasiparticle properties, like the residue, are the subject of Section 4.

2 Model and Diagrammatic structure

We consider a dilute two-component gas of ultra-cold fermionic atoms interacting via the van der Waals-potential. The Hamiltonian has a kinetic and interaction term

$$\hat{H} = \sum_{\mathbf{k},\sigma=\uparrow\downarrow} \epsilon_{\mathbf{k}\sigma}\ \hat{c}^{\dagger}_{\mathbf{k}\sigma}\hat{c}_{\mathbf{k}\sigma} + \frac{1}{\mathcal{V}} \sum_{\mathbf{k},\mathbf{k}',\mathbf{q}} V(\mathbf{k}-\mathbf{k}')\ \hat{c}^{\dagger}_{\mathbf{k}+\frac{\mathbf{q}}{2}\uparrow}\hat{c}^{\dagger}_{-\mathbf{k}+\frac{\mathbf{q}}{2}\downarrow}\hat{c}_{-\mathbf{k}'+\frac{\mathbf{q}}{2}\downarrow}\hat{c}_{\mathbf{k}'+\frac{\mathbf{q}}{2}\uparrow}\ .$$

The operators $\hat{c}^{\dagger}_{\mathbf{k}\sigma}$ ($\hat{c}_{\mathbf{k}\sigma}$) create (annihilate) fermions with momentum $\mathbf{k}$ and spin σ. The spin-σ fermions have mass m_σ and dispersion $\epsilon_{\mathbf{k}\sigma} = k^2/2m_\sigma$, and $\mathcal{V}$ is the volume of the system. We take $\hbar = 1$ throughout the paper, and consider the mass-balanced case $m_\uparrow = m_\downarrow = m$. All the theoretical considerations are for zero temperature (or $T \ll T_F$ with T_F the Fermi temperature). The diluteness of the system ensures that the range b of the potential is much smaller than the typical inter-particle distance $1/k_F$, or $k_F b \ll 1$, with k_F the Fermi momentum of the spin-up sea, and therefore the details of the interaction potential become irrelevant. Accordingly, without loss of generality, one can model the short-ranged interaction as a contact interaction, $V(\mathbf{r}) = g_0\delta(\mathbf{r})$, in combination with the standard ultra-violet divergence regularization procedure described below.

The one-body and two-body propagators provide access to information about the 'polaron' and 'molecule' channel respectively. The polaron and molecule are two distinct objects belonging to different charge sectors. The one-body and two-body propagators are discussed in Sections 2.1 and 2.3. The adopted regularization procedure for the renormalized interaction is the subject of Section 2.2. The DiagMC method is introduced in Section 2.4.

2.1 One-body propagator

The polaron quasiparticle properties can be extracted from the impurity's Green's function defined as

$$G_\downarrow(\mathbf{k},\tau) = -\theta(\tau)\langle\Phi_0^{N_\uparrow}|\hat{c}_{\mathbf{k}\downarrow}(\tau)\hat{c}^{\dagger}_{\mathbf{k}\downarrow}(0)\ |\Phi_0^{N_\uparrow}\rangle\ , \tag{2}$$

with $\hat{c}_{\mathbf{k}\downarrow}(\tau)$ the annihilation operator in the Heisenberg picture,

$$\hat{c}_{\mathbf{k}\downarrow}(\tau) = e^{(\hat{H}-\mu\hat{N}_\downarrow-\mu_\uparrow\hat{N}_\uparrow)\tau}\hat{c}_{\mathbf{k}\downarrow}e^{-(\hat{H}-\mu\hat{N}_\downarrow-\mu_\uparrow\hat{N}_\uparrow)\tau}\ . \tag{3}$$

The propagator $G_\downarrow(\mathbf{k},\tau)$ is written in the momentum imaginary-time representation, μ is a free parameter, $\hat{N}_\sigma$ is the number operator for spin-σ particles, and $\mu_\uparrow$ is the chemical potential of the spin-up sea. The state

$$|\Phi_0^{N_\uparrow}\rangle = |\rangle_\downarrow|FS(N_\uparrow)\rangle\ , \tag{4}$$

consists of the spin-down vacuum and the non-interacting spin-up Fermi sea. Since we are dealing with an impurity spin-down atom, $G_\downarrow$ is only non-zero for times $\tau > 0$. The ground-state energy and Z-factor can be extracted from the Green's function of Eq. (2). Inserting a complete set of eigenstates $|\Psi_n^{N_\uparrow}\rangle$ of the full Hamiltonian (2) for one spin-down

particle and $N_\uparrow$ spin-up particles into Eq. (2) yields for $\mathbf{k} = \mathbf{0}$

$$G_\downarrow(\mathbf{0},\tau) = -\theta(\tau)\sum_n |\langle\Psi_n^{N_\uparrow}|\hat{c}^\dagger_{\mathbf{0}\downarrow}|\Phi_0^{N_\uparrow}\rangle|^2 e^{-(E_n(N_\uparrow)-E_{FS}-\mu)\tau}$$
$$\overset{\tau\to+\infty}{=} -Z_p\, e^{-(E_p-\mu)\tau}\ ,$$

with E_p the energy of the polaron, $E_n(N_\uparrow)$ the energy eigenvalues of the Hamiltonian (2) and $E_{FS} = 3\ \epsilon_F N_\uparrow/5$ the energy of the ideal spin-up Fermi gas, with $\epsilon_F = k_F^2/(2m)$ the Fermi energy.

The difference between the polaronic and molecular state is embedded in the factors $|\langle\Psi_n^{N_\uparrow}|\hat{c}^\dagger_{\mathbf{0}\downarrow}|\Phi_0^{N_\uparrow}\rangle|^2$ in Eq. (5). For situations where the polaron is a well-defined quasiparticle in the ground state $|\Psi_0^{N_\uparrow}\rangle$, we have Eq. (1) for the Z-factor and $E_p = E_0(N_\uparrow) - E_{FS}$. If, on the other hand, the ground state $|\Psi_0^{N_\uparrow}\rangle$ is a dressed molecule the overlap $\langle\Psi_0^{N_\uparrow}|\hat{c}^\dagger_{\mathbf{0}\downarrow}|\Phi_0^{N_\uparrow}\rangle$ is zero [11]. This is clear from the expansion of the molecular state in the number of particle-hole excitations,

$$|\Psi_0^{N_\uparrow}\rangle = \left(\sum_{\mathbf{k}}{}' \xi_{\mathbf{k}}\hat{c}^\dagger_{-\mathbf{k}\downarrow}\hat{c}^\dagger_{\mathbf{k}\uparrow} + \sum_{\mathbf{k},\mathbf{k}',\mathbf{q}}{}' \xi_{\mathbf{k}\mathbf{k}'\mathbf{q}}\hat{c}^\dagger_{\mathbf{q}-\mathbf{k}-\mathbf{k}'\downarrow}\hat{c}^\dagger_{\mathbf{k}\uparrow}\hat{c}^\dagger_{\mathbf{k}'\uparrow}\hat{c}_{\mathbf{q}\uparrow} + \dots\right)|\Phi_0^{N_\uparrow-1}\rangle\ . \tag{5}$$

The coefficients ξ are variational parameters, and the primes indicate that the sums on $\mathbf{k}$, $\mathbf{k}'$ and $\mathbf{q}$ are restricted to $|\mathbf{k}|, |\mathbf{k}'| > k_F$ and $|\mathbf{q}| < k_F$. Even if a molecule is formed in the ground state, the polaron can be a well-defined excited state (in the sense of a narrow peak in the spectral function), and Z_p can be non-zero.

For vanishing interactions V the impurity Green's function of Eq. (2) becomes

$$G^0_\downarrow(\mathbf{k},\tau) = -\theta(\tau)e^{-(\epsilon_{\mathbf{k}\downarrow}-\mu)\tau}\ . \tag{6}$$

The one-body propagator for the spin-up sea is defined as

$$G_\uparrow(\mathbf{k},\tau) = -\langle\Psi_0^{N_\uparrow}|T_\tau\left[\hat{c}_{\mathbf{k}\uparrow}(\tau)\hat{c}^\dagger_{\mathbf{k}\uparrow}(0)\right]\ |\Psi_0^{N_\uparrow}\rangle\ , \tag{7}$$

with T_τ the time-ordering operator. Without interactions, one obtains the free propagator

$$G^0_\uparrow(\mathbf{k},\tau) = \begin{cases} -e^{-(\epsilon_{\mathbf{k}\uparrow}-\epsilon_F)\tau}\theta(|\mathbf{k}|-k_F) & \text{if}\quad \tau > 0\ , \\ e^{-(\epsilon_{\mathbf{k}\uparrow}-\epsilon_F)\tau}\theta(k_F-|\mathbf{k}|) & \text{if}\quad \tau < 0\ . \end{cases}$$

Our goal is to calculate the $G_\downarrow$ of Eq. (2) to extract E_p by means of Eq. (5). This is achieved by summing all irreducible one-particle self-energy diagrams with the DiagMC algorithm (which works in momentum-imaginary-time representation). The irreducible self-energy $\Sigma(\mathbf{k},\omega)$ in imaginary-frequency representation is obtained after a numerical Fourier transform, and inserted into Dyson's equation to give $G_\downarrow$,

$$\left[G_\downarrow(\mathbf{k},\omega)\right]^{-1} = \left[G^0_\downarrow(\mathbf{k},\omega)\right]^{-1} - \Sigma(\mathbf{k},\omega)\ , \tag{8}$$

with ω the imaginary frequency. A graphical representation of the Dyson equation is shown in the top panel of Fig. 1. As was shown in Ref. [8], the polaron energy E_p and Z-factor Z_p

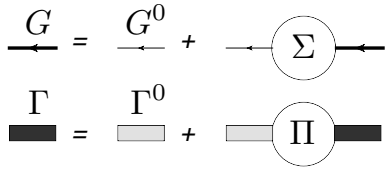

Figure 1 – Graphical representation of the Dyson equation and the Bethe-Salpeter equation. The free (dressed) one-body impurity propagator is denoted by $G^0_\downarrow$ ($G_\downarrow$). The Σ and Π are the one-body and two-body self-energies, respectively. The Γ is the fully dressed interaction, wheres Γ^0 is the partially dressed interaction obtained by summing all the bare ladders $G^0_\downarrow G^0_\uparrow$ (see Eqs. (14) and (15)).

can be extracted directly from the self-energy $\Sigma(\mathbf{0},\tau)$,

$$E_p = \int_0^{+\infty} d\tau\ \Sigma(\mathbf{0},\tau)\ e^{(E_p-\mu)\tau}\ , \tag{9}$$

$$Z_p = \frac{1}{1-\int_0^{+\infty} d\tau\ \tau\ \Sigma(\mathbf{0},\tau)\ e^{(E_p-\mu)\tau}}\ . \tag{10}$$

The effective mass m_* of the polaron is evaluated with the estimator[8]

$$m_* = \frac{1/Z_p}{1/m + B_0}\ , \tag{11}$$

with

$$B_0 = \int_0^{+\infty} d\tau\ e^{(E_p-\mu)\tau}\ \left[\frac{1}{3}\nabla^2_{\mathbf{k}}\Sigma(\mathbf{k},\tau)|_{k=0}\right]\ , \tag{12}$$

which can conveniently be estimated by expanding $\Sigma(\mathbf{k},\tau)$ in Legendre polynomials. One obtains

$$\frac{1}{3}\nabla^2_{\mathbf{k}}\Sigma(\mathbf{k},\tau)|_{k=0} = \frac{15}{2\Delta^3}\int_0^{\Delta} dk\ \Sigma(k,\tau)\left(\frac{3k^2}{\Delta^2}-1\right)\ , \tag{13}$$

and the integral can be evaluated during the MC simulation. The upper limit of integration (Δ) is optimized to minimize the statistical noise while avoiding a systematic error at too large Δ. We also used an alternative way by calculating the quasiparticle spectrum $E(\mathbf{k})$ and fitting m_* via $E(\mathbf{k}) = E_p + k^2/(2m_*)$.

2.2 Renormalized interaction

We introduce the s-wave scattering length a for collisions between spin-up and spin-down particles. One of the advantages of working with Feynman diagrams is that one can work directly in the zero-range limit $k_F b \to 0$ (or, equivalently, $\Lambda/k_F \to +\infty$ with Λ an ultraviolet momentum cut-off) while keeping $k_F a$ constant. Thereby, the ultra-violet physics can be taken into account by means of a summation over all Feynman ladder diagrams.

In momentum-imaginary-frequency representation $(\mathbf{p}, \Omega)$, one obtains for the partially dressed interaction

$$\Gamma^0(\mathbf{p},\Omega) \quad = \quad g_0 + g_0\, \Pi^0(\mathbf{p},\Omega)\, \Gamma^0(\mathbf{p},\Omega)\,, \tag{14}$$

with Π^0 the two-particle self-energy consisting of one 'bare' ladder

$$\begin{aligned}\Pi^0(\mathbf{p},\Omega) &= -\frac{1}{2\pi\mathcal{V}} \sum_{|\mathbf{q}|<\Lambda} \int d\omega\; G^0_\uparrow(\frac{\mathbf{p}}{2}+\mathbf{q},\omega) G^0_\downarrow(\frac{\mathbf{p}}{2}-\mathbf{q},\Omega-\omega) \\ &= \frac{1}{\mathcal{V}} \sum_{|\mathbf{q}|<\Lambda} \frac{\theta(|\mathbf{p}/2+\mathbf{q}|-k_F)}{i\Omega - p^2/(4m) - q^2/m + \mu + \epsilon_F}\,,\end{aligned} \tag{15}$$

where the momentum cutoff Λ is required to keep the sum finite. The bare coupling constant $V(\mathbf{p}) = \int d\mathbf{r} e^{-i\mathbf{p}\cdot\mathbf{r}} V(\mathbf{r}) = g_0$ can be eliminated in favor of the physical scattering length a by using standard scattering theory

$$\frac{1}{g_0} = \frac{m}{4\pi a} - \frac{1}{\mathcal{V}} \sum_{|\mathbf{k}|<\Lambda} \frac{1}{2\epsilon_{\mathbf{k}}}\,. \tag{16}$$

The $\Gamma^0(\mathbf{p},\Omega)$ from Eq. (14) can be expressed in terms of the s-wave scattering length a, by taking the limit $\Lambda \to +\infty$ and $g_0 \to 0^-$ with a fixed. In this zero-range limit, one gets

$$[\Gamma^0(\mathbf{p},\Omega)]^{-1} = [\tilde{\Gamma}^0(\mathbf{p},\Omega)]^{-1} - \bar{\Pi}(\mathbf{p},\Omega)\,, \tag{17}$$

with

$$\bar{\Pi}(\mathbf{p},\Omega) = -\int \frac{d\mathbf{q}}{(2\pi)^3}\, \theta(k_F-q) \frac{1}{i\Omega - \frac{q^2}{2m} - \frac{(\mathbf{p}-\mathbf{q})^2}{2m} + \mu + \epsilon_F}\,. \tag{18}$$

Here, we have taken the thermodynamic limit ($\mathcal{V} \to +\infty$ and $N_\uparrow/\mathcal{V}$ fixed). The integral in Eq. (18) can be evaluated analytically, and the dressed interaction in vacuum is given by

$$[\tilde{\Gamma}^0(\mathbf{p},\Omega)]^{-1} = \frac{m}{4\pi a} - \frac{m}{8\pi}\sqrt{p^2 - 4m(i\Omega + \mu + \epsilon_F)}\,, \tag{19}$$

for $\Omega \neq 0$ or $\mu < -\epsilon_F$, and assuming the principal branch. For $\mu < -[\epsilon_F + 1/(ma^2)]$, the Fourier transform to imaginary time can be done analytically, producing

$$\tilde{\Gamma}^0(\mathbf{p},\tau) = -\frac{4\pi}{m^{3/2}} e^{-(\frac{p^2}{4m}-\mu-\epsilon_F)\tau} \left(\frac{1}{\sqrt{\pi\tau}} + \frac{1}{\sqrt{m}a} e^{\frac{\tau}{ma^2}} \mathrm{erfc}\Big(-\sqrt{\frac{\tau}{m}}\frac{1}{a} \Big) \right)\,, \tag{20}$$

with $\mathrm{erfc}(x)$ the complementary error function. As in Ref. [8], we use $\Gamma^0(\mathbf{p},\tau)$ as a partially dressed interaction vertex in the diagrammatic series, instead of the bare interaction vertex g_0. This dressed vertex is calculated here in imaginary time representation by performing the Fourier transform of Eq. (17) numerically.

In a next step, the interaction vertex will be fully dressed by calculating the two-particle self-energy Π and plugging it into the Bethe-Salpeter equation,

$$[\Gamma(\mathbf{p},\Omega)]^{-1} = [\Gamma^0(\mathbf{p},\Omega)]^{-1} - \Pi(\mathbf{p},\Omega)\,. \tag{21}$$

A graphical representation of this equation is shown in Fig. 1. The self-energy Π contains all connected two-particle diagrams that are irreducible with respect to cutting a single Γ^0 propagator. To avoid double counting, the diagrams for Π should not contain any ladders, since those have been summed in Γ^0 by means of the Eq. (14). This rule also holds when summing diagrams for the one-body self-energy Σ, built from free propagators G^0_σ and Γ^0.

2.3 Two-body propagator

Here, we consider the pair annihilation operator,

$$\hat{P}_{\mathbf{k}} = \sum_{\mathbf{q}} \varphi(\mathbf{q})\ \hat{c}_{\mathbf{k}-\mathbf{q}\uparrow}\hat{c}_{\mathbf{q}\downarrow}\ , \tag{22}$$

with $\varphi(\mathbf{q})$ the momentum representation of the wave function $\varphi(\mathbf{r})$ for relative motion of the two fermions of opposite spin. The two-particle propagator is defined as

$$G_2(\mathbf{k},\tau) = -\theta(\tau)\langle\Phi_0^{N_\uparrow}|\hat{P}_{\mathbf{k}}(\tau)\hat{P}^\dagger_{\mathbf{k}}(0)\ |\Phi_0^{N_\uparrow}\rangle\ , \tag{23}$$

where we included the fact that the impurity spin-$\downarrow$ atom propagates forward in time. Inserting the complete basis $|\Psi_n^{N_\uparrow+1}\rangle$ for $(N_\uparrow+1)$ spin-up particles and one spin-down particle, gives

$$\begin{aligned} G_2(\mathbf{0},\tau) &= -\theta(\tau)\sum_n |\langle\Psi_n^{N_\uparrow+1}|\hat{P}^\dagger_{\mathbf{0}}\ |\Phi_0^{N_\uparrow}\rangle|^2 e^{-(E_n(N_\uparrow+1)-E_{FS}(N_\uparrow)-\mu_\uparrow-\mu)\tau} \\ &\overset{\tau\to+\infty}{=} -Z_{\rm mol}\ e^{-(E_{\rm mol}-\mu)\tau}\ , \end{aligned} \tag{24}$$

with $E_{\rm mol}$ the molecule energy and $Z_{\rm mol}$ the molecule Z-factor. If the molecule is a well-defined quasiparticle in the ground state, we have

$$Z_{\rm mol} = |\langle\Psi_0^{N_\uparrow+1}|\hat{P}^\dagger_{\mathbf{0}}|\Phi_0^{N_\uparrow}\rangle|^2\ , \tag{25}$$

and $E_{\rm mol} = E_0(N_\uparrow+1) - E_{FS}(N_\uparrow) - \mu_\uparrow$. Note that the value of $Z_{\rm mol}$ depends on the wave function $\varphi(\mathbf{q})$. The functional from of this pair wave function depends on the nature of experiment used to probe the molecule.

In practice, it is easier to calculate the molecule energy from the fully dressed interaction Γ (see Eq. (21)). This function is closely related to the pair correlation function, namely,

$$\Gamma(\mathbf{k},\tau) = g_0\delta(\tau) + g_0\ \mathcal{P}(\mathbf{k},\tau)\ g_0\ , \tag{26}$$

with

$$\mathcal{P}(\mathbf{r},\tau) = -\theta(\tau)\langle\Phi_0^{N_\uparrow}|(\hat{\Psi}_\uparrow\hat{\Psi}_\downarrow)(\mathbf{r},\tau)(\hat{\Psi}^\dagger_\downarrow\hat{\Psi}^\dagger_\uparrow)(\mathbf{0},0)|\Phi_0^{N_\uparrow}\rangle\ , \tag{27}$$

the pair correlation function. The field operators $\hat{\Psi}^\dagger_\sigma(\mathbf{r}) = \sum_{\mathbf{k}} e^{-i\mathbf{k}\mathbf{r}}\hat{c}^\dagger_{\mathbf{k},\sigma}/\sqrt{\mathcal{V}}$ create a spin-σ fermion at position $\mathbf{r}$. In Eq. (27) the pair of particles is created at the same position (which corresponds to $\varphi(\mathbf{q})=1$ in Eq. (22)). The structure of the fully dressed interaction Γ and the two-particle propagator G_2 now implies that both structures have the same poles (see Eq. (26)). Therefore, the exponential tail of the function $\Gamma(\mathbf{k}=\mathbf{0},\tau)$ can conveniently be used for estimating the molecule energy, rather than the tail of $G_2(\mathbf{0},\tau)$. This is equivalent with looking for this pole of the Bethe-Salpeter equation (21). The molecule's energy $E_{\rm mol}$ is given by the parameter μ that satisfies the equation

$$[\Gamma^0(\mathbf{p}=\mathbf{0},\Omega=0)]^{-1} = \Pi(\mathbf{p}=\mathbf{0},\Omega=0)\ , \tag{28}$$

where the left-hand-side is known analytically, and the right-hand-side is evaluated with the DiagMC algorithm in imaginary-time domain.

2.4 Diagrammatic Monte Carlo

DiagMC evaluates the series of Feynman diagrams for the self-energy in a stochastic way. We deal with both the one-body and two-body self-energies. In a first step, the self-energy is built from the free propagators G^0_σ and the partially dressed interaction Γ^0 (obtained through summation of $G^0_\downarrow G^0_\uparrow$ ladders; as discussed in Section 2.2). We will refer to this series as the 'bare series'. Fig. 2 shows the one-body and two-body self-energy diagrams up to order 3 in the bare scheme. The order of a diagram is N when there are N dressed interactions Γ (i.e., N boxes) present in the Σ-diagram, and $N-1$ boxes in the Π-diagram. Note that the diagrams cannot contain ladders since these have been taken into the vertex function Γ^0. To illustrate the factorial growth with order, the number of one-body self-energy diagrams for given order $N \leq 12$ is given in the second column of Table 1 for the bare series.

In a second step, we will use dressed propagators or 'bold lines' in the diagrams. Such dressed (skeleton) series are evaluated with the Bold DiagMC technique [13, 3]. We consider the case with only dressed $G_\downarrow$ propagators while keeping Γ^0 of Eqs. (17) and (18) as renormalized interaction, and the case whereby both the one-body propagators and interactions are dressed. We will refer to these skeleton series as 'bold G' and 'bold G-Γ', respectively. In the latter case, the Bold DiagMC algorithm is constructed as follows: given approximate one-body and two-body self-energies Σ and Π, the Dyson and Bethe-Salpeter equation are solved to deliver the one-body propagator $G_\downarrow$ and the dressed interaction Γ (see Eqs. (8) and (21)). In a next step, these are used to dress the series for Σ and Π, which are evaluated stochastically with DiagMC up to order N_*. This self-consistent cycle is repeated until convergence is reached. Fig. 3 shows the skeleton (bold G-Γ) series for the one- and two-body self-energies up to order 4. Evidently, when dressing the lines in the self-energies, one has to keep track of two-particle reducibility, and systematically avoid any double counting. This typically means that at any order N the numbers in the second column of Table 1 (Bare) are an upper limit of the number of diagrams in the third and fourth column. At $N = 2$ and $N = 4$, however, the number of diagrams increases due to the fact that ladders should be included again once $G_\downarrow$ is bold. All the diagrams of Table 1 are summed explicitly during the (Bold) DiagMC simulation.

3 Resummation and boldification

When considering a diagrammatic series, it is natural to ask whether there are dominant classes of diagrams. Identification of the dominant diagrams potentially allows one to make good approximations. To address this issue, we constructed a histogram counting how many times a certain topology is sampled. We consider first the bare series. It turns out that for the one-body self-energy, roughly half of the simulation time is spent on sampling two diagrams at each order. These two diagrams are shown in Figure 4 for diagram order six. To understand why these two diagrams are dominant at a fixed N, we use an argument first made by Hugenholtz[14]. For the dilute spin-up gas, momentum integration inside the Fermi sea is heavily restricted in phase space (momentum integration runs up to the Fermi momentum $k_F \sim (N_\uparrow/\mathcal{V})^{1/3}$). This implies the presence of a backward (or hole) spin-up propagator reducing the contribution of the diagram significantly, while the forward (particle) propagator enhances the contribution roughly with a factor $\int_{|\mathbf{k}|>k_F} d\mathbf{k}$. As a consequence,

N	Bare	Bold G	Bold G-Γ
1	1	1	1
2	0	1	0
3	2	2	1
4	6	7	2
5	34	34	13
6	210	206	74
7	1,526	1,476	544
8	12,558	12,123	4,458
9	115,618	111,866	41,221
10	1,177,170	1,143,554	421,412
11	13,136,102	12,816,572	4,722,881
12	159,467,022	156,217,782	57,553,440

Table 1 – Factorial increase of the number of Feynman diagrams. At fixed order N, the number of one-body self-energy diagrams is given for different types of series: the bare series, the skeleton series with dressed $G_\downarrow$ (bold G), and the skeleton series with dressed $G_\downarrow$ and Γ lines (bold G-Γ).

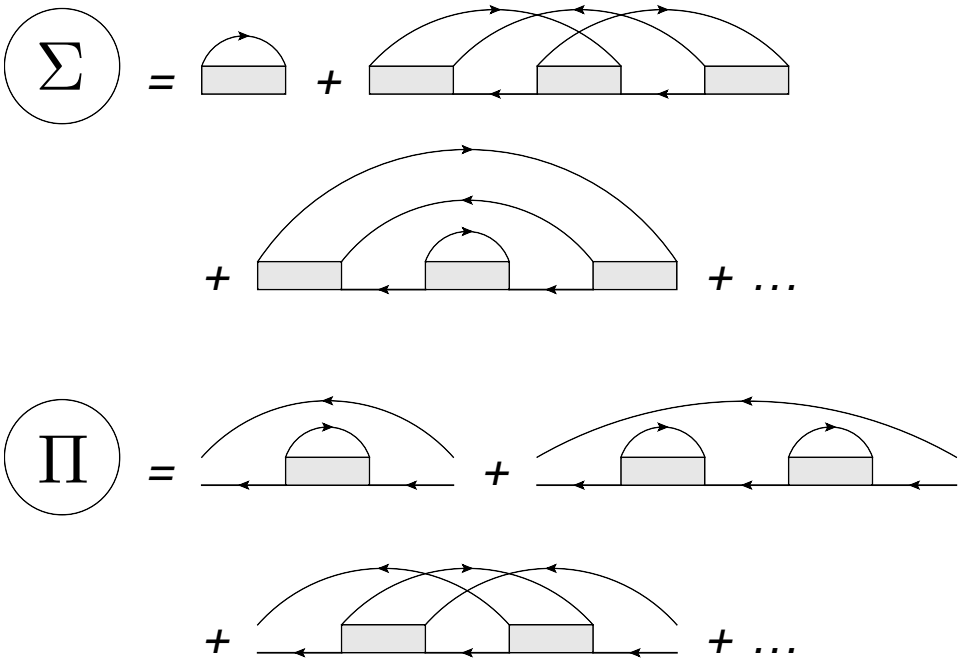

Figure 2 – Diagrammatic expansion for the one-body self-energy Σ and the two-body self-energy Π. Here, the diagrams are built from the bare propagators G^0_σ (thin lines), and the partially dressed interaction Γ^0 (light grey box). All diagrams have a 'backbone' structure, since we have a single impurity propagating forward in time and interacting with a Fermi sea of free particles.

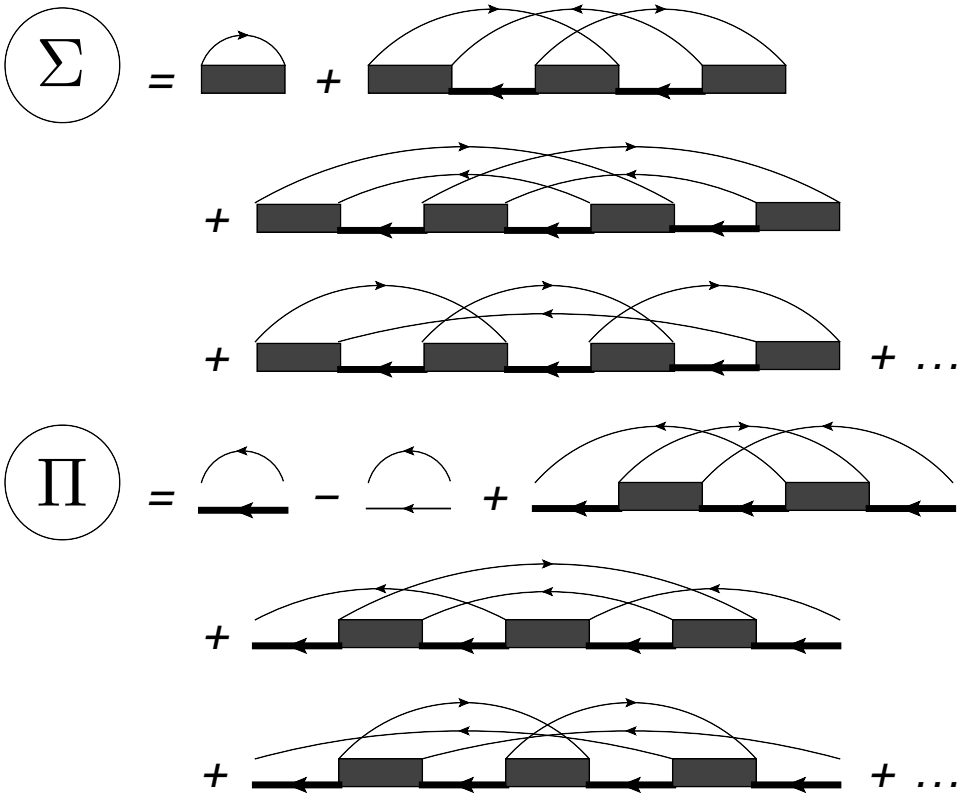

Figure 3 – Skeleton diagrammatic expansion for the one-body and two-body self-energy: the impurity propagator and interaction lines that appear in the diagram are fully dressed solutions of the Dyson equation and the Bethe-Salpeter equation (see Fig. 1).

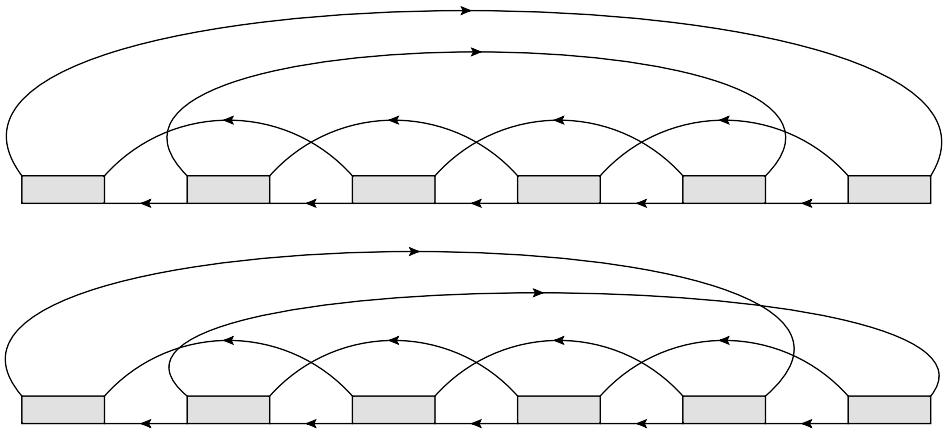

Figure 4 – The figure contains the two dominant one-body self-energy diagrams for $N = 6$. Imaginary time runs from right to left.

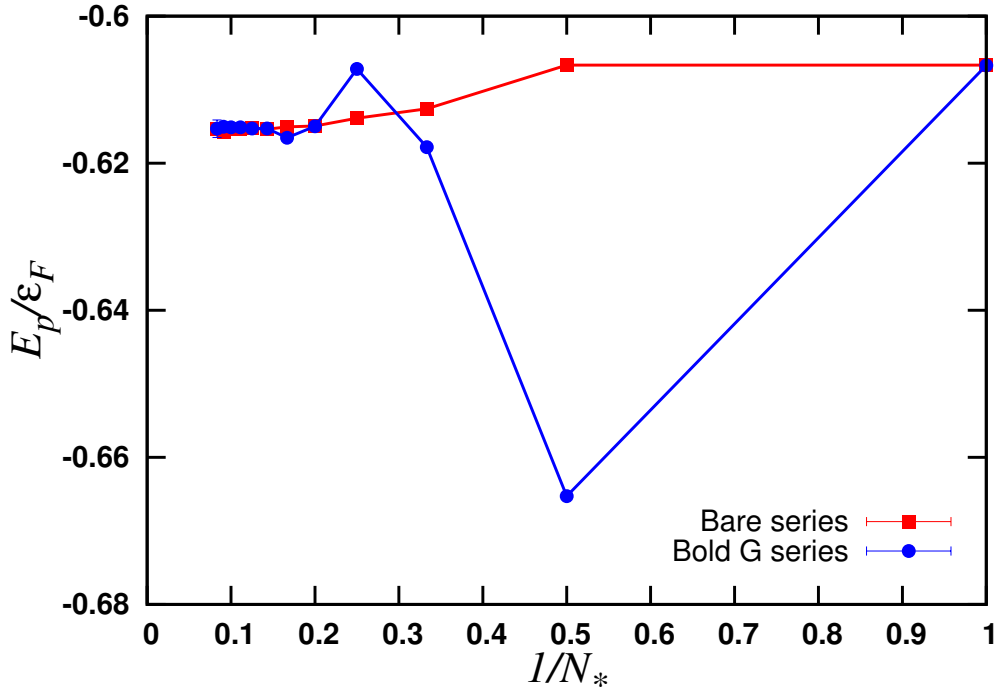

Figure 5 – The polaron energy in units of the Fermi energy as a function of the inverse maximum diagram order $1/N_*$ for irreducible self-energy diagrams at unitarity $1/(k_F a) = 0$. The red squares show the polaron energy calculated via Eq. (9) with self-energy diagrams built from the free propagators G^0_σ and the partially dressed propagator Γ^0. The blue circles show the results from the bold-G approach.

diagrams with the smallest possible number of hole propagators will be dominant. For the self-energy, we see that, at fixed order, the minimum number of hole propagators is two. Since the number of fermion loops differs by one, these two diagrams have opposite sign. Numerically we found that the two diagrams almost cancel each other. This can be seen in Figure 5, where we show the polaron energy E_p as a function of the inverse diagram order cut-off N_* for the interaction strength $1/(k_F a) = 0$. For the 'bare series', we observe a fast convergence due to cancellation of diagrams. This magic cancellation was referred to as 'sign blessing' [3]. At infinite scattering length, such near cancellation was also observed by Combescot and Giraud [15]. They have found that the success of the Chevy ansatz at strong coupling can be attributed to a nearly perfect destructive interference of the states with more than one particle-hole excitation. Combescot and Giraud illustrated that an expansion in powers of the hole wave vectors converges extremely rapidly at unitarity. In our case, the series is organized differently, but at fixed order we have exactly the same type of cancellation between diagrams with the same number of hole propagators[16]. Just like in the Combescot-Giraud argument, the cancellation is exact when the momentum-dependence of the hole propagators is neglected. Note that the dominant diagrams (see Figure 4) can also be viewed as three-body T-matrix diagrams closed with two hole propagators [17]. This class

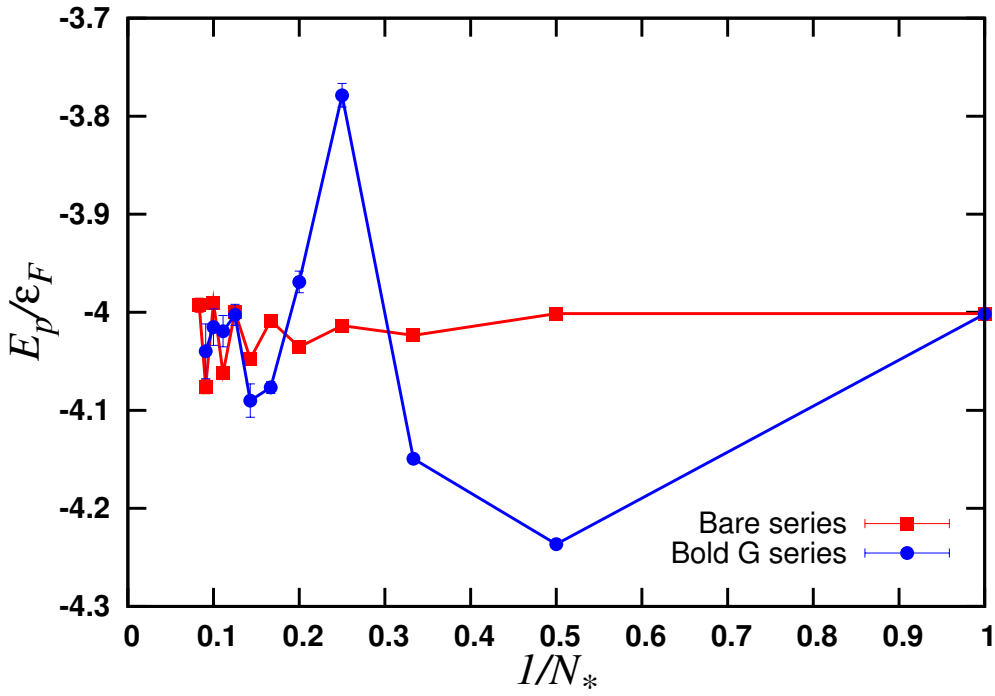

Figure 6 – Same plot as Figure 5, but now considering the interaction strength parameter $1/(k_F a) = 1.333$. In the bare series, small oscillations prevent us from extrapolating to infinite diagram order.

of diagrams, in which there are at most two particle-hole excitations, has been considered previously for the polaron problem [12, 15]. It was shown that they exactly reproduce the Skorniakov and Ter-Martirosian equation [18] in the BEC limit. In this strong-coupling limit, the dominant process is scattering between a dimer and a spin-up fermion, which is diagrammatically represented by the three-body T-matrix diagrams. Away from this limit, the considered class of diagrams turns out to give a quantitatively good correction to the lowest order result. We find that this is due to their dominance, even away from the BEC limit.

When going towards the BEC side ($1/a > 0$), the cancellation between dominant diagrams of the type shown in Figure 4 is no longer perfect. Figure 6 shows the polaron energy as a function of $1/N_*$ for $1/(k_F a) = 1.333$. For the bare series, the oscillations prevent one from extracting E_p for $1/N_* \to 0$.

To cure the bad convergence of the bare series for $1/(k_F a) > 0$ one can include more diagrams by dressing the propagators. We start by dressing the spin-down propagator lines, while keeping the partially dressed Γ^0. Diagrams reducible with respect to cutting *two* spin-down lines should no longer be sampled, since they are included implicitly. For $1/(k_F a) = 0$ the self-energy $\Sigma(\mathbf{k}, \tau)$ converges in this 'bold G scheme' for $N_* \geq 7$. Extrapolation to infinite N_* gives the exact Σ and $G_\downarrow$. Figure 5 includes the polaron energy as function of diagram order

cut-off when the one-body self-energy is built with the exact $G_\downarrow$. The bare and bold series converge to the same energy. Remarkably, the dressed scheme gives worse results at low N_*. This indicates that approximations based on a few low order diagrams are completely uncontrolled, and including more diagrams by dressing the lines does not necessarily improve the quality of the results.

For $1/(k_F a) = 1.333$, we see that dressing the impurity lines helps to get rid of the residual oscillations in the bare scheme (see Figure 6). One might expect that dressing even more, by using a fully dressed Γ instead of Γ^0, might lead to even better convergence. Figure 7 shows however that, even for $1/(k_F a) = 0$, the fully bold series (bold G-Γ scheme) does not seem to converge (N_* is the diagram cut-off for both Σ and Π, and a Bold DiagMC simulation is done for each N_*), in contrast to the results of Ref.[8]. The data for the fully bold simulation of Ref.[8] was obtained by using the exact G and Γ (i.e. extrapolated to the $N_* \to \infty$ limit with resummation factors). They were not obtained with a self-consistent simulation, which explains the difference. Moreover, data is not shown above $N_* = 7$, where oscillations do occur. In order to understand why the series no longer converges, we introduce an intermediate scheme (which we call bold G-Γ^1): the self-energy is built from the fully converged $G_\downarrow$ and a partially dressed interaction Γ^1, built from summing the ladders $G_\downarrow G^0_\uparrow$. The result is also shown in Figure 7, and we again observe convergence to the same answer as in Figure 5. The key difference between both schemes is that in the bold G-Γ^1 scheme, both dominant diagrams shown in Fig. 4 still explicitly contribute to the self-energy, whereas in the fully bold scheme the upper dominant diagram becomes reducible and is taken into account self-consistently. This means that the balance of cancellation between diagrams is broken, and a single dominant diagram keeps contributing at each order. So, it turns out that dressing the diagrams as much as possible is not always a good idea. In this respect, our findings disagree with Ref.[8].

A second method to cure the bad convergence of the bare series on the BEC side, is to employ series resummation techniques. We will use the Abelian resummation techniques[19] which have been used when calculating the equation of state of the unitary gas with Bold DiagMC[20]. This resummation technique works as follows. One starts from a series $f(x) = \sum_n d_n x^n$ that has a *finite* radius of convergence $R > 0$. The idea is to sum the series at some point x_0 outside of the radius R by analytically continuing the function f. This provides a good procedure for summing the divergent series in the sense that it respects basic operations (sum, multiplication and derivative) and that it preserves distinctness[19]. It is well-known that with analytic continuation, one can encounter problems with the existence and/or uniqueness of the solution[21]. However, one can formally define a domain called the 'Mittag-Leffler star' where the function can be analytically continued along straight lines $[0, x_0]$. Note that this star will always contain the disk of convergence. It can be shown[19] that for each point x_0 of the Mittag-Leffler star, the limit

$$\lim_{\epsilon \to 0^+} \sum_n d_n x_0^n e^{-\epsilon \lambda_n} , \tag{29}$$

with $\lambda_n = n \log(n)$ for $n > 0$ and $\lambda_0 = 0$, exists and is equal to the analytic continuation of f to the point x_0. Note that within the disk of convergence the procedure works equally well, and can improve the rate of convergence. We apply the Abelian resummation technique to the expansion of the self-energy Σ and Π. As the analytic structure of Σ and Π is unknown, it is currently impossible to determine whether there is a finite radius of convergence and

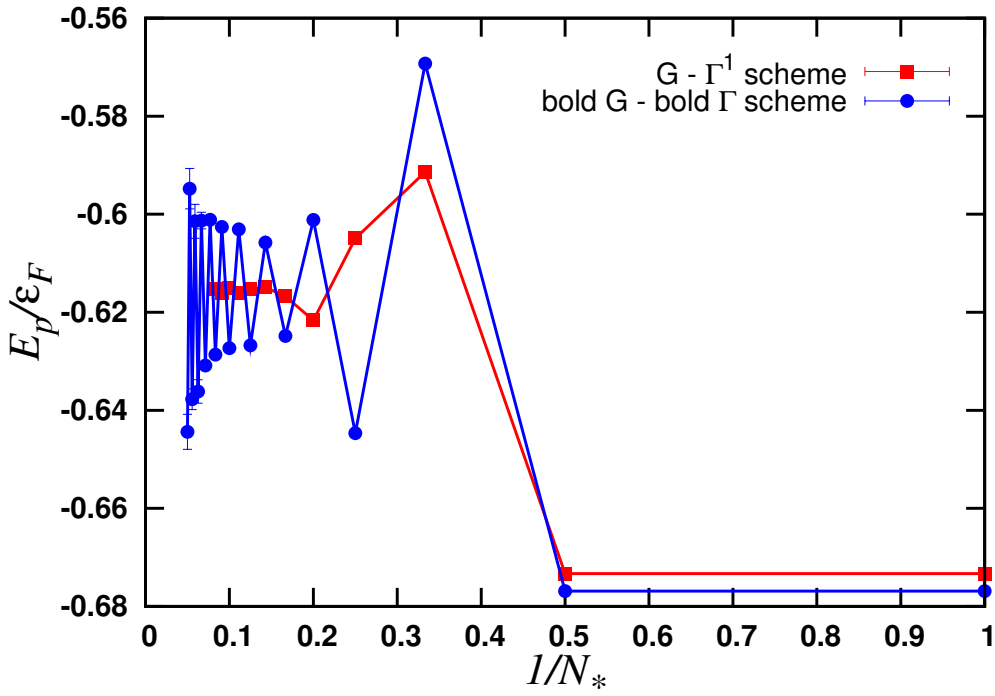

Figure 7 – The polaron energy in units of the Fermi energy as a function of the inverse maximum diagram order $1/N_*$ for irreducible self-energy diagrams at unitarity $1/(k_F a) = 0$. The blue circles show results from a fully Bold DiagMC simulation: the self-energy diagrams are built from fully dressed one-particle propagators $G_\downarrow$ and two-particle propagators Γ up to self-energy diagram order N_*. The red squares show the polaron energy calculated with diagrams built with the exact $G_\downarrow$ and a partially dressed interaction Γ^1 containing the sum of all $G_\downarrow G_\uparrow^0$ ladders.

whether we are in the Mittag-Leffler star. In practice, we apply different resummation techniques (i.e., different functions λ_n), and test the uniqueness of the result.

We use following λ_n: (i) Lindelöf 1: $\lambda_n = n\,\log(n)$ for $n > 0$ and $\lambda_0 = 0$; (ii) Lindelöf 2: $\lambda_n = (n-1)\,\log(n-1)$ for $n > 1$ and $\lambda_0 = \lambda_1 = 0$; (iii) Gauss 1: $\lambda_n = n^2$ for $n \geq 0$; (iv) Gauss 2: $\lambda_n = (n-1)^2$ for $n \geq 1$ and $\lambda_0 = 0$; (iv) Gauss 3: $\lambda_n = (n-2)^2$ for $n \geq 2$ and $\lambda_0 = \lambda_1 = 0$. Before applying these resummation techniques to our diagrammatic series, we illustrate its power with an example for the geometric series. Figure 8 shows the sums $f_\epsilon(x_0 = -3) = \sum_n x_0^n e^{-\epsilon\lambda_n}$ for a few choices of λ_n. At small ϵ, the computation of f_ϵ is no longer feasible due to finite computer precision. By extrapolating to $\epsilon = 0$, we indeed find $1/(1-x_0)$ with high precision. The Lindelöf curve gives a slighly less accurate extrapolation because it suppresses high order contributions in a much smoother fashion than the Gaussian resummation. When applying these techniques to our diagrammatic series, it is the growth of the statistical error bars (due to factorial complexity) that prevents us from going to very small values of ϵ. Figure 9 shows the polaron energy calculated with the resummed self-energy as a function of the control parameter ϵ for $1/(k_F a) = 1.333$. The polaron energy

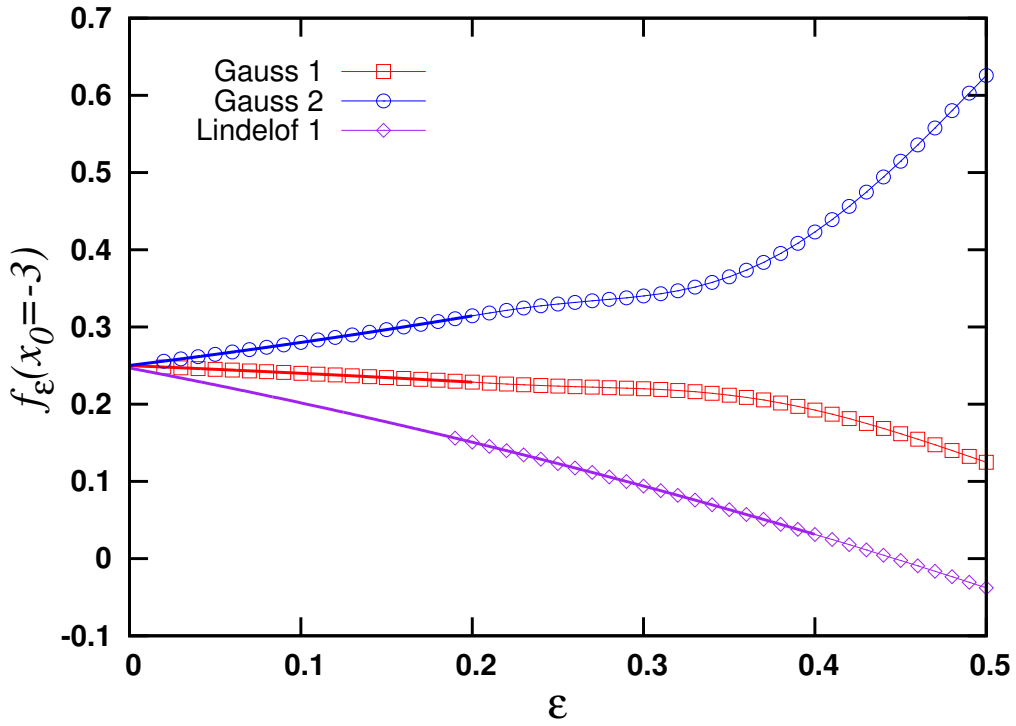

Figure 8 – Illustration of the Abelian resummation technique for the geometric series. We evaluate $f_\epsilon(x_0) = \sum_n x_0^n e^{-\epsilon\lambda_n}$ for $x_0 = -3$. and various choices of λ_n. The value of the analytically continued function $1/(1-x_0)$ is retrieved for $\epsilon \to 0^+$.

E_p can be extracted with high accuracy. The major source of error bar stems from the uncertainty in the extrapolation.

Histogramming the different topologies of the two-body self-energies Π revealed a dominant diagram at each order. This diagram is shown in Figure 10. Again it shows a three-body T-matrix structure that is closed with a single spin-up hole propagator. Upon increasing the diagram order up to 20, we observe a steady growth in the contribution of this diagram. This is illustrated in Figure 11, where we plot the n-th order contribution Π_n to the two-body self-energy as a function of imaginary time τ for external momentum zero. Figure 12 illustrates that we can nonetheless get accurate values for the molecule energy E_{mol} by using different Abelian resummation techniques and extrapolating to $\epsilon = 0^+$. Again, the Gaussian resummation methods allow one to reach very small values of ϵ. The quoted error bars are rather conservative as we include the extrapolated results obtained with all choices for λ_n.

We also tested the resummability of the fully bold series (bold G - bold Γ scheme), since this was used in the Bold DiagMC method for determining the equation of state of the unitary gas[20]. When applying the Abelian resummation techniques and extrapolate to $\epsilon = 0^+$ at $1/(k_F a) = 0$, the correct polaron energy is retrieved. This constitutes an independent check for the resummation of the skeleton series.

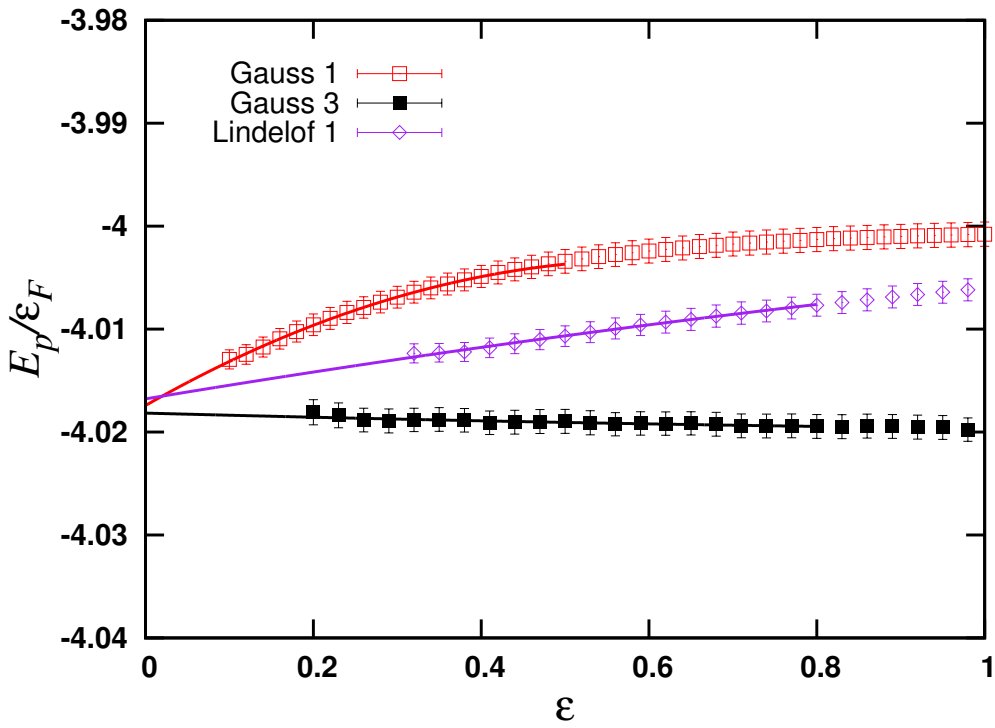

Figure 9 – Abelian resummation of the bare series of one-body self-energy diagrams at $1/(k_F a) = 1.333$. The polaron energy E_p/ϵ_F is extracted in the limit $\epsilon = 0^+$ for different choices of λ_n.

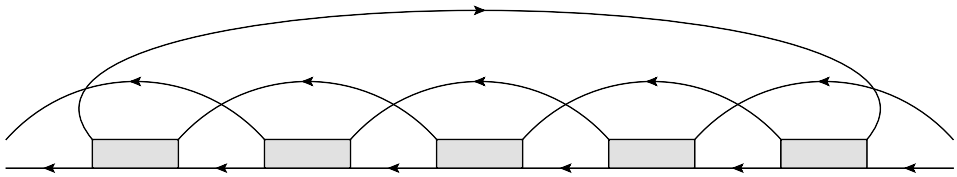

Figure 10 – At fixed order, there is one dominant diagram for the two-body self-energy. Here, we draw this diagram at order six.

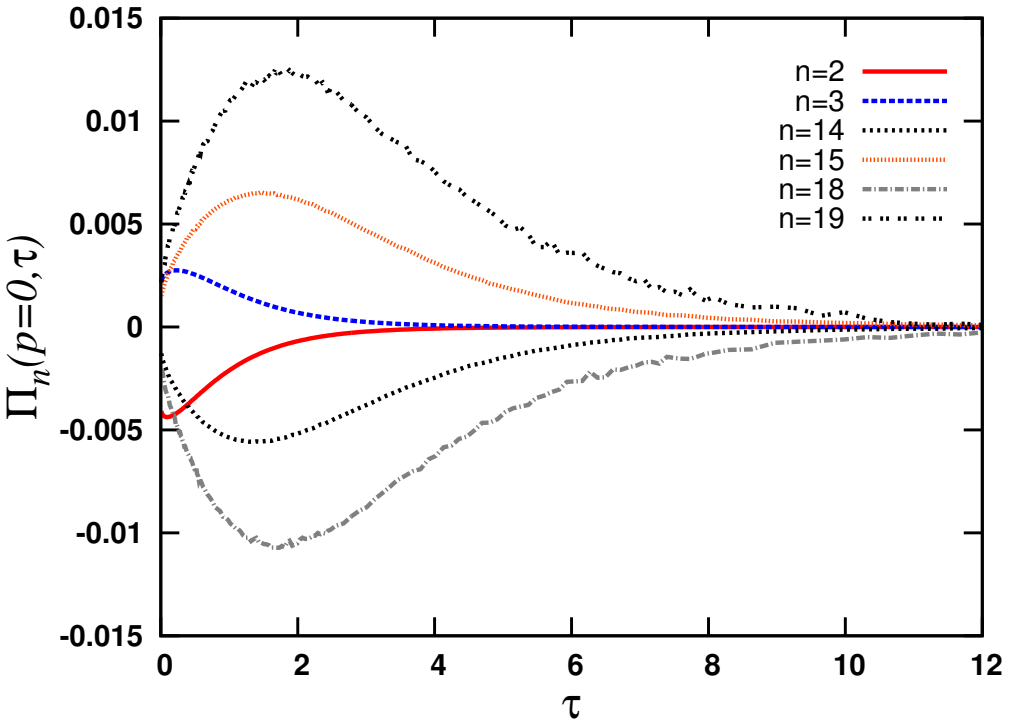

Figure 11 – The two-particle self-energy Π at external momentum zero as a function of imaginary time for $k_F a = 1$. The Π_n are the contribution of all n-th order diagrams, and here shown for various n. As n increases, Π_n keeps on growing. We work in units $k_F = 1$, $m = 1$, $\hbar = 1$ and $\mu/\epsilon_F = -3.2$. The noise in the curves indicates the magnitude of the statistical error.

4 Quasiparticle properties

As an independent cross-check of Ref. [3], which uses alternate ways of resumming the diagrammatic series, we calculate the ground-state energies of the polaron and molecule. Figure 13 shows these energies shifted by the vacuum molecule energy $E_b = -1/(ma^2)$ in units of the Fermi energy ϵ_F. A selection of the polaron and molecule energies is also given in Table 2. We find the transition point at $(k_F a)_c = 1.15(3)$, in agreement with Ref. [3]. Close to the transition point, we find polaron energies that differ about 1% with the polaron energies of Ref.[3], which, we believe, is due to a small systematic error in the lowest order diagram in Ref.[3]. The variational energies obtained from a wave-function ansatz for the polaron[9] and the molecule[11] are very close to the Monte Carlo results. Note that Chevy's variational ansatz for the polaron state is completely equivalent with the non-self-consistent T-matrix approximation [12] which is exactly our bare series at $N_* = 1$. Fixed node-difussion Monte Carlo (FN-DMC) results are also in good agreement with the DiagMC data. For $1/(k_F a) = 2$ it seems that systematic errors on the FN-DMC results were underestimated, since FN-DMC should in principle give an upper bound to the true ground-state energy.

Figure 14 shows the effective mass of the polaron as calculated with DiagMC. We compare

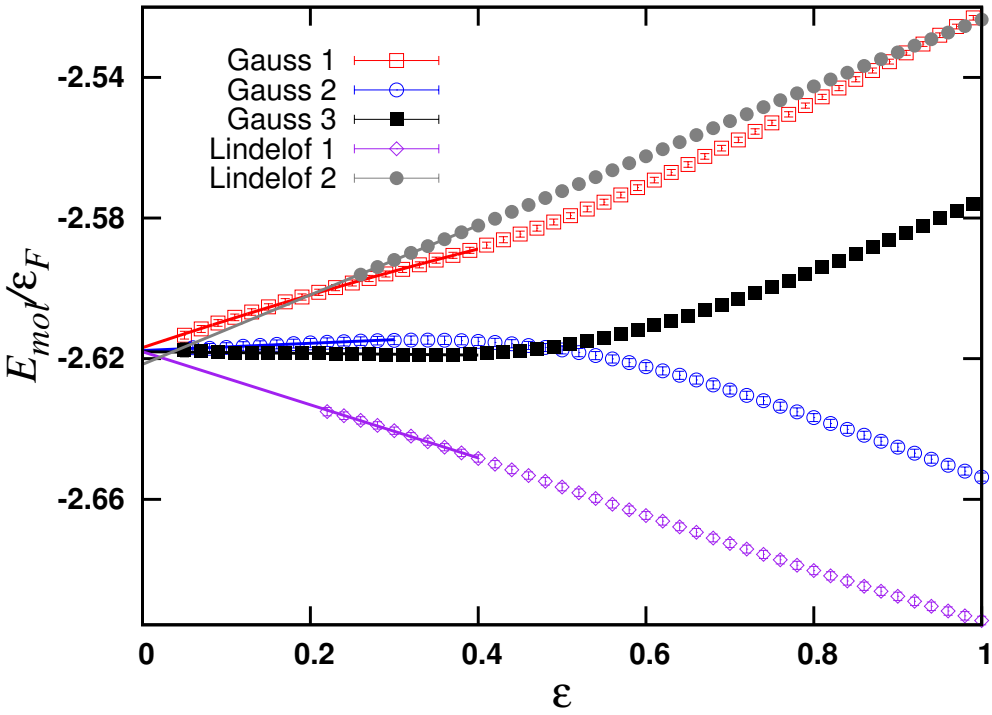

Figure 12 – Abelian resummation of the bare series of two-particle self-energy diagrams at $k_F a = 1$. The molecule energy $E_{\rm mol}/\epsilon_F$ is extracted in the limit $\epsilon = 0^+$ for different choices of λ_n.

with the ENS experiment [5] at unitarity, DiagMC calculations by Prokof'ev-Svistunov[3], FN-DMC[6, 7], a variational calculation up to two particle-hole excitations[12], and the first order ($N_* = 1$) result in the bare scheme and the fully bold G-Γ scheme. The experimental effective mass, which is in perfect agreement with DiagMC [3], was extracted from the low frequency breathing modes, and in particular the Fermi polaron breathing mode. The lowest order bare calculation, also known as T-matrix approximation, is equivalent to the Chevy ansatz, while the lowest order bold calculation corresponds to the self-consistent T-matrix approximation. These results show that including only single particle-hole pair excitions does not lead to accurate results for the effective mass, while the variational calculation based on diagrams taking into account at most two particle-hole pairs excitations agrees with the DiagMC results[12].

Experimental and theoretical quasiparticle residues are shown in Fig. 15. To create and probe polarons, the MIT experiment[4] starts from a cloud of ^{6}Li atoms with most atoms occupying the lowest hyperfine state $|1\rangle$ (spin-up), and about 2% of the atoms occyping the hyperfine state $|3\rangle$ (spin-down) in the degenerate regime $T \approx 0.14\ T_F$ with T_F the Fermi temperature. A broad Feshbach resonance is used to enhance the scattering between atoms in states $|1\rangle$ and $|3\rangle$. Radio-frequency (rf) spectra of the spin-up and spin-down components are measured. The atoms are transferred to a third empty state with very weak final-state interactions. Therefore, the measured transition rate I can be connected with the impurity's

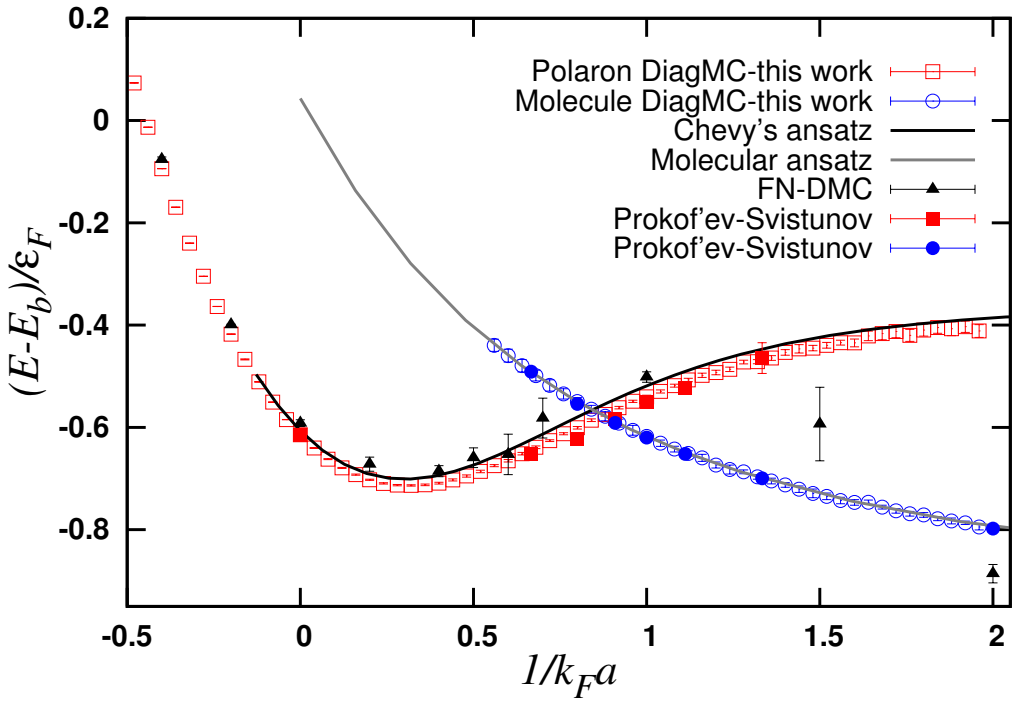

Figure 13 – The extracted polaron and molecule energy as a function of the interaction strength $1/(k_F a)$. The energies are expressed as $(E - E_b)/\epsilon_F$, with $E_b = -1/(ma^2)$ the molecule energy in vacuum. The FN-DMC results are from Ref.[6], the variational results for the polaron from Ref.[9] and for the molecule from Ref.[11]. DiagMC results by Prokof'ev and Svistunov[3] are also shown.

spectral function $\rho_\downarrow$ in linear response theory[22, 23]

$$I(\omega_L) \propto \sum_{\mathbf{k}} n_F(\epsilon_{\mathbf{k}} - \mu - \omega_L)\ \rho_\downarrow(\mathbf{k}, \epsilon_{\mathbf{k}} - \mu - \omega_L)\ , \tag{30}$$

with ω_L the frequency of the rf photons and $n_F(x) = 1/(1+e^{\beta x})$ the Fermi distribution. Note that the spectral function depends on the temperature. Density inhomogeneities are taken care of through tomographic reconstruction [4]. At sufficiently weak attractions, the Fermi polaron is observed as a narrow peak in the impurity spectrum that is not matched by the broad environment spectrum. The peak position gives the polaron energy E_p, and was found to be in perfect agreement with the DiagMC results of Ref. [3]. The polaron Z-factor was measured by determining the ratio of the area under the impurity peak that is not matched by the environment, and the total area under the impurity's spectrum. The experimental Z-factor from Ref. [4] is shown in Figure 15, together with the Z-factor calculated from Chevy's ansatz[11, 24], the fully self-consistent result in lowest order ($N_* = 1$) and our DiagMC simulation. DiagMC data for the Z-factor is also given in Table 2.

The results obtained via DiagMC simulation agree extremely well with Chevy's variational ansatz. This is very surprising in the strongly interacting regime where Z_p is significantly

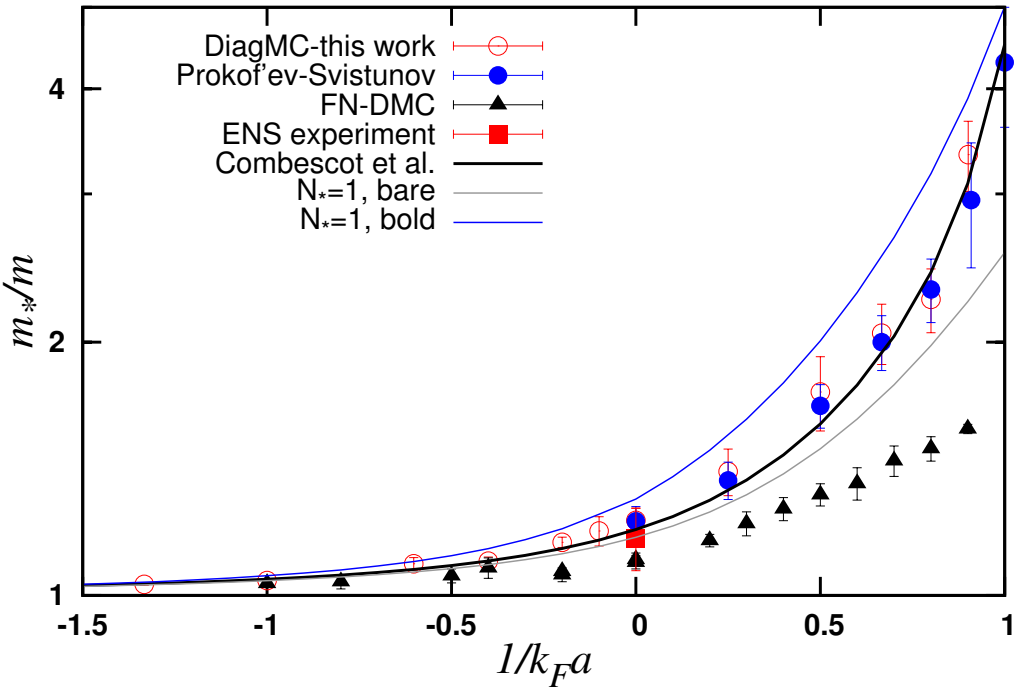

Figure 14 – The effective mass m_* of the polaron in units of the bare mass m as a function of the interaction parameter $1/(k_F a)$. Our DiagMC results (open circles) are shown together with DiagMC results by Prokof'ev and Svistunov[3] (filled blue circles), FN-DMC results[6, 7] (black triangles), ENS experiment[5] (red square) and a variational calculation up to two particle-hole excitations [12] (solid black line). We also show m_* calculated from the lowest order self-energy diagram (i.e., $N_* = 1$) for the bare series (solid grey line) and for the fully bold G-Γ series (solid blue line), which are equivalent to the non-self-consistent and the self-consistent T-matrix approximation, respectively.

smaller than one. Here, one would expect multiple particle-hole excitations to be important since the overlap with the non-interacting wave-function is small. Remarkably, including just single particle-hole excitations on top of the Fermi sea produces almost the exact Z_p. When the lowest order diagram is calculated in a fully self-consistent way, however, the agreement with DiagMC is less good. This hints at the fact that the almost perfect agreement with Chevy's ansatz (i.e., the lowest order bare result) is rather accidental.

The Z-factors computed with Chevy's ansatz and DiagMC both exceed the measured ones. It was suggested in Ref.[11] that the disagreement between the experiment and the Chevy ansatz is an artefact of Chevy's expansion being restricted to one particle-one hole excitations. As the DiagMC technique includes multiple particle-multiple hole excitations and agrees very well with Chevy's ansatz, we see that this is not the case. However, since the measured Z_p might only give a lower bound[4], theory and experiment might not be in disagreement.

The measured polaron Z-factor vanishes beyond a critical interaction strength. Ignoring issues related to metastability, once the two-body bound state becomes energetically favorable,

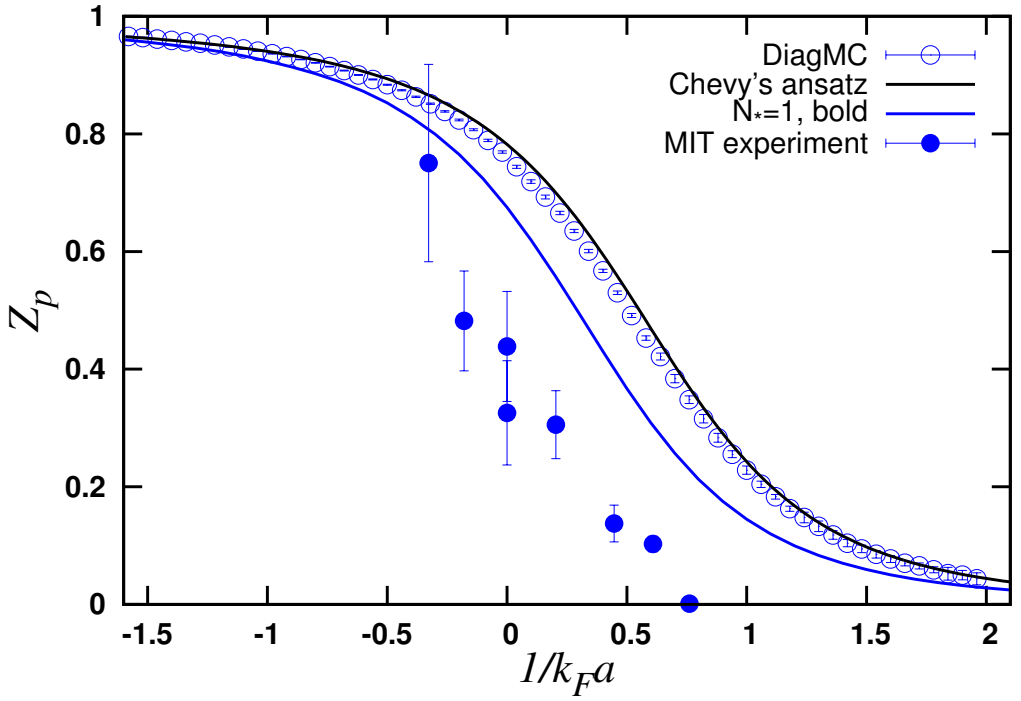

Figure 15 – The polaron quasiparticle residue Z_p as a function of the interaction parameter $1/(k_F a)$. DiagMC results (open circles) are compared with variational ansatz[11] (black solid line), the fully bold G-Γ series at $N_* = 1$ or self-consistent T-matrix approximation (solid blue line) and the MIT experiment[4] (blue circles).

all polarons disappear and the polaron peak vanishes. In the experiment $T/T_F = 0.14(3)$, and finite-temperature effects are thus expected to become important. Indeed, close to $(k_F a)_c = 1.15(3)$ the energy difference between the molecule and polaron state is of the order of 0.1 T_F (Fig. 13). Therefore, one expects that $T = 0$ calculations underestimate the critical $1/(k_F a)$ measured at $T \approx 0.1\ T_F$. Similarly, the measured $1/(k_F a)_c$ can be interpreted as an upper bound for the $T = 0$ situation. On the other hand, due to depletion of the experimental spectrum, the measured Z might only give a lower bound, which means that the experimentally determined critical $1/(k_F a)$ might be underestimated. These uncertainties might explain why the critical $1/(k_F a)$ in the experiment is lower than the value obtained with DiagMC for a single impurity. Fixed-node Monte-Carlo simulations for a finite density of impurities, on the other hand, predict phase separation before the systems even reaches the polaron-to-molecule transition[6], and the vanishing Z-factor might be a manifestation of this phase separation.

$1/(k_F a)$	E_p/E_F	E_{mol}/E_F	Z_p
-1.8	-0.1793(1)		0.9727(4)
-1.6	-0.1961(1)		0.9665(5)
-1.4	-0.2159(2)		0.9590(3)
-1.2	-0.2393(2)		0.9502(3)
-1.0	-0.2687(2)		0.9376(4)
-0.8	-0.3052(2)		0.9209(5)
-0.6	-0.3526(2)		0.8978(8)
-0.4	-0.4141(2)		0.8670(10)
-0.2	-0.4976(2)		0.8237(15)
0.0	-0.615(1)		0.7586(27)
0.2	-0.782(1)		0.6720(42)
0.4	-1.028(2)		0.5672(28)
0.6	-1.385(2)	-1.180(13)	0.4410(32)
0.8	-1.880(2)	-1.830(8)	0.3258(58)
1.0	-2.540(3)	-2.618(6)	0.2283(70)
1.2	-3.372(4)	-3.554(6)	0.1559(69)
1.4	-4.373(5)	-4.633(5)	0.1102(68)
1.6	-5.554(8)	-5.867(6)	0.0771(58)
1.8	-6.889(12)	-7.251(5)	0.0578(35)

Table 2 – Selection of DiagMC data for the polaron energy E_p, molecule energy E_{mol} and polaron residue Z_p for several values of the interaction strength parameter $1/(k_F a)$.

5 Conclusions

We have considered the Fermi-polaron system in three dimensions, in which a single spin-down impurity is strongly coupled to a non-interacting Fermi sea of spin-up particles. Although this system contains strongly interacting fermions, it can be solved with the Diagrammatic Monte-Carlo method. This method is based on the stochastic evaluation of a series of Feynman diagrams. To extract ground-state properties, one has to overcome a factorial complexity due to the increase of the number of diagrams. Nonetheless, extrapolation to infinite diagram order becomes possible when the diagrams cancel each other better than the factorial increase in number. At interaction strength $1/(k_F a) = 0$, we find such perfect cancellation (within our statistical errors). When considering the series built on bare propagators on the BEC side, however, oscillations with diagram order remain and prevent a controlled extrapolation to the infinite diagram order. We have followed two strategies around this problem: the first is to consider skeleton series (built on dressed propagators), and the second the use of resummation techniques. Though dressed series can be evaluated to higher orders, we have found that in some cases dressing can destroy a favorable cancellation of diagrams. For all interaction strengths we found that the (skeleton) series of the one-body and two-body self-energy is resummable by means of Abelian resummation. Bare series, skeleton series and resummed series give robust answers in their respective region of applicability (i.e. where the infinite diagram order extrapolation is controlled).

We have identified classes of dominant diagrams for the one-body and two-body self-energy in the crossover region of strong interaction. The dominant diagrams turn out to be the leading

processes of the strong-coupling limit: scattering between a dimer and a spin-up fermion, which is diagrammatically represented by the three-body T-matrix diagrams. Including just these dominant diagrams gives a quantitatively good correction to the lowest order result, even away from the strong-coupling limit.

We have shown that not only the polaron and molecule energies agree very well with a variational ansatz from weak to strong attraction, but also the polaron residue or Z-factor. Though this agreement must be due to strong cancellation of diagrams, we only observed convergence for the bare series at $1/(k_F a) = 0$. A full explanation for the success of the variational ansatz is still missing, and it is therefore unclear in which cases the ansatz is appropriate.

This work is supported by the Fund for Scientific research - Flanders. The authors would like to thank C. Lobo, N. Prokof'ev, B. Svistunov, F. Werner and M. Zwierlein for the helpful discussions and suggestions. We thank R. Combescot, S. Pilati, N. Prokof'ev, M. Punk, B. Svistunov and M. Zwierlein for sending us their data.

References

[1] L.D. Landau, Phys. Z. Sowjetunion **3**, 664 (1933).

[2] E.M. Lifshitz and L.P. Pitaevskii, *Statistical Mechanics*, Part 2 (Pergamon Press, New York, 1980).

[3] N.V. Prokof'ev and B.V. Svistunov, Phys. Rev. B **77**, 020408 (2008).

[4] A. Schirotzek, C.H. Wu, A. Sommer and M.W. Zwierlein, Phys. Rev. Lett. **102**, 230402 (2009).

[5] S. Nascimbène, N. Navon, K.J. Jiang, L. Tarruell, M. Teichmann, J. McKeever, F. Chevy and C. Salomon, Phys. Rev. Lett. **103**, 170402 (2009).

[6] S. Pilati and S. Giorgini, Phys. Rev. Lett. **100**, 030401 (2008).

[7] S. Pilati, private communication.

[8] N.V. Prokof'ev and B.V. Svistunov, Phys. Rev. B **77**, 125101 (2008).

[9] F. Chevy, Phys. Rev. A **74**, 063628 (2006).

[10] C. Mora and F. Chevy, Phys. Rev. A **80**, 033607 (2009).

[11] M. Punk, P.T. Dumitrescu and W. Zwerger, Phys. Rev. A **80**, 053605 (2009).

[12] R. Combescot, S. Giraud and X. Leyronas, EPL **88**, 60007 (2009).

[13] N.V. Prokof'ev and B.V. Svistunov, Phys. Rev. Lett. **99**, 250201 (2007).

[14] N.M. Hugenholtz, Physica **23**, 533 (1957).

[15] R. Combescot and S. Giraud, Phys. Rev. Lett. **101**, 050404 (2008).

[16] S. Giraud, Ph.D. thesis, Université Paris VI, 2010, http://tel.archives-ouvertes.fr/tel-00492339

[17] X. Leyronas and R. Combescot Phys. Rev. Lett. **99**, 170402, (2007).

[18] G.V. Skorniakov and K.A. Ter-Martirosian, Zh. Eksp. Teor. Fiz. **31**, 775 (1956) [Sov. Phys. JETP **4**, 648 (1957)].

[19] G.H. Hardy, *Divergent Series* (Oxford University Press, New York, 1956).

[20] K. Van Houcke, F. Werner, E. Kozik, N. Prokofev, B. Svistunov, M.J.H. Ku, A. T. Sommer, L.W. Cheuk, A. Schirotzek and M.W. Zwierlein, Nature Phys. **8**, 366 (2012).

[21] P. Dennery and A. Krzywicki, *Mathematics for Physicists* (Dover, New York, 1996).

[22] Y. Ohashi and A. Griffin, Phys. Rev. A **72**, 013601 (2005).

[23] P. Massignan, G.M. Bruun and H.T.C. Stoof, Phys. Rev. A **77**, 031601(R) (2008).

[24] C. Trefzger and Y. Castin, arXiv:1210.8179.

CHAPTER 3

The 2D Fermi polaron

In chapter 2 we discussed why ultracold gases provide a very good test system to study strongly interacting many-body systems. With the use of optical potentials the degrees of motion in one direction can be frozen out and it becomes possible to study low-dimensional systems. It is generally known that the behavior of a quantum system can change drastically by lowering the dimensionality. A dramatic example is the ideal, uniform Bose gas which undergoes the BEC phase transition in 3D at a finite temperature, while in 2D no condensation is possible at a finite temperature [19]. In this chapter we study the 2D Fermi polaron by making use of a diagrammatic series for the Green's function.

3.1 Renormalized interaction

For the 3D Fermi polaron we calculated a renormalized interaction which is well-defined in the continuum limit. It turns out that for the 2D Fermi polaron we also encounter divergences if we use the interaction $V_{\downarrow\uparrow}(\mathbf{r}-\mathbf{r}') = g_0\delta(\mathbf{r}-\mathbf{r}')$. For the 1D Fermi polaron these divergences are absent and there is no regularization requirement[29, 30]. We calculate a renormalized interaction for the 2D Fermi polaron, thereby following a similar approach as in the 3D case (see Sec. 2.3).

Consider the expression given in Eq. (2.23), now in 2D:

$$\frac{1}{\Gamma^0(\mathbf{p},\Omega)} = \frac{1}{g_0} - \int_{\mathcal{B},|\mathbf{q}|>k_F} \frac{d\mathbf{q}}{(2\pi)^2} \quad \frac{1}{i\Omega - \epsilon_{\mathbf{p}-\mathbf{q}\downarrow} + \mu - \epsilon_{\mathbf{q}\uparrow} + \epsilon_F} \,. \tag{3.1}$$

with $\epsilon_{\mathbf{p}-\mathbf{q}\downarrow} = \frac{(\mathbf{p}-\mathbf{q})^2}{2m_\downarrow}$ and $\epsilon_{\mathbf{q}\uparrow} = \frac{q^2}{2m_\uparrow}$. The integral is over the first Brillouin zone $\mathcal{B} =]-\pi/b, \pi/b]^2$ of the reciprocal lattice, with b the lattice spacing. With the use of Eq. (1.20) the interaction strength parameter g_0 can be removed in favour of the two-body binding

energy ε_B in Eq. (3.1),

$$\frac{1}{\Gamma^0(\mathbf{p},\Omega)} = -\int_{\mathcal{B}} \frac{d\mathbf{q}}{(2\pi)^2} \frac{1}{\epsilon_{\mathbf{q}\downarrow} + \epsilon_{\mathbf{q}\uparrow} + \varepsilon_B} - \int_{\mathcal{B},|\mathbf{q}|>k_F} \frac{d\mathbf{q}}{(2\pi)^2} \frac{1}{i\Omega - \epsilon_{\mathbf{p}-\mathbf{q}\downarrow} + \mu - \epsilon_{\mathbf{q}\uparrow} + \epsilon_F} . \quad (3.2)$$

Note that we use the convention here that $\varepsilon_B > 0$ (hence the extra minus in front of ε_B). By grouping the two integrands together, this expression is well-defined in the continuum limit, $l \to 0$ and $g_0 \to 0^-$ such that ε_B is fixed. We consider only the mass-balanced case $m_\uparrow = m_\downarrow = m$, with $\epsilon_{\mathbf{k}\downarrow,\uparrow} = \epsilon_{\mathbf{k}} = \frac{\mathbf{k}^2}{2m}$. To evaluate Eq. (3.2) we write $\Gamma^{0^{-1}}(\mathbf{p},\Omega)$ as

$$\Gamma^{0^{-1}}(\mathbf{p},\Omega) = \tilde{\Gamma}^{0^{-1}}(\mathbf{p},\Omega) - \bar{\Pi}(\mathbf{p},\Omega) , \quad (3.3)$$

with

$$\frac{1}{\tilde{\Gamma}^0(\mathbf{p},\Omega)} = -\int \frac{d\mathbf{q}}{(2\pi)^2} \left(\frac{1}{i\Omega - \epsilon_{\mathbf{p}-\mathbf{q}} + \mu - \epsilon_{\mathbf{q}} + \epsilon_F} + \frac{1}{\epsilon_{\mathbf{q}} + \epsilon_{\mathbf{q}} + \varepsilon_B} \right) , \quad (3.4)$$

and $\bar{\Pi}(\mathbf{p},\Omega)$:

$$\bar{\Pi}(\mathbf{p},\Omega) = -\int \frac{d\mathbf{q}}{(2\pi)^2} \frac{\theta(k_F - |\mathbf{q}|)}{i\Omega - \epsilon_{\mathbf{q}} - \epsilon_{\mathbf{p}-\mathbf{q}} + \mu + \epsilon_F} . \quad (3.5)$$

The function $\tilde{\Gamma}^{0^{-1}}(\mathbf{p},\Omega)$ can be calculated analytically, for $\Omega \neq 0$ or $\mu < -\epsilon_F$:

$$\tilde{\Gamma}^{0^{-1}}(\mathbf{p},\Omega) = \frac{m}{4\pi} \ln\left[-\frac{\varepsilon_B}{i\Omega + \mu + \epsilon_F - \frac{\epsilon_{\mathbf{p}}}{2}} \right] , \quad (3.6)$$

and

$$\begin{aligned} \bar{\Pi}(\mathbf{p},\Omega) &= -\int \frac{d\mathbf{q}}{(2\pi)^2} \frac{\theta(k_F - |\mathbf{q}|)}{i\Omega - \epsilon_{\mathbf{p}-\mathbf{q}} - \epsilon_{\mathbf{q}} + \mu + \epsilon_F} \\ &= -\frac{m}{4\pi} \left(\ln\left[-2(z + 2\epsilon_F) + \epsilon_{\mathbf{p}} \right] - \ln\left[-z + \sqrt{(z - \epsilon_{\mathbf{p}})^2 - 4\epsilon_F \epsilon_{\mathbf{p}}} \right] \right) , \end{aligned} \quad (3.7)$$

with $z = i\Omega + \mu - \epsilon_F$, and we have assumed $\mu < -\epsilon_F$ to obtain this last equality. After combining Eqs. (3.3), (3.6) and (3.7), one gets

$$\Gamma^{0^{-1}}(\mathbf{p},\Omega) = \frac{m}{4\pi} \ln\left[-\frac{2\varepsilon_B}{z - \sqrt{(z - \epsilon_{\mathbf{p}})^2 - 4\epsilon_F \epsilon_{\mathbf{p}}}} \right] . \quad (3.8)$$

We now take the Fourier transform of Eq. (3.6) to imaginary-time representation to obtain $\tilde{\Gamma}^0(\mathbf{p},\tau)$ (see appendix B):

$$\begin{aligned} \tilde{\Gamma}^0(\mathbf{p},\tau) &= \frac{1}{2\pi} \int_{-\infty}^{+\infty} d\Omega \; e^{-i\Omega\tau} \; \tilde{\Gamma}^0(\mathbf{p},\Omega) , \\ &= -\frac{4\pi\varepsilon_B}{m} e^{-(\frac{\epsilon_{\mathbf{p}}}{2} - \epsilon_F - \mu)\tau} \left[\int_0^{+\infty} dx \frac{e^{-x\varepsilon_B\tau}}{\pi^2 + \ln^2(x)} + e^{\varepsilon_B\tau} \right] \theta(\tau) , \end{aligned} \quad (3.9)$$

for $\mu < -\epsilon_F - \varepsilon_B$. The integral in Eq. (3.9) can be computed numerically. For $\tau \to 0^+$ we make use of the following assymptotic behavior:

$$\begin{aligned} \int_0^{+\infty} dx \frac{e^{-x\varepsilon_B\tau}}{\pi^2 + \ln^2(x)} &= \frac{1}{\varepsilon_B\tau} \int_0^{+\infty} dy \frac{e^{-y}}{\pi^2 + \ln^2(\frac{y}{\varepsilon_B\tau})} \\ &\underset{\tau\to 0}{\sim} \frac{1}{\varepsilon_B\tau} \frac{1}{\ln^2(\varepsilon_B\tau)} . \end{aligned} \quad (3.10)$$

Similar as in the 3D case, we consider the sum of $\left(\Gamma^0(\mathbf{p},\tau)-\tilde{\Gamma}^0(\mathbf{p},\tau)\right)$ and $\tilde{\Gamma}^0(\mathbf{p},\tau)$ to obtain $\Gamma^0(\mathbf{p},\tau)$. The function $\tilde{\Gamma}^0(\mathbf{p},\tau)$ contains the sharp, divergent behavior if $\tau \to 0^+$, which is handled through the analytic expression Eq. (3.10). The difference $\left(\Gamma^0(\mathbf{p},\tau)-\tilde{\Gamma}^0(\mathbf{p},\tau)\right)$ is a bounded function and can easily be tabulated numerically.

3.2 DiagMC for the 2D Fermi polaron

In this section we highlight some differences for the DiagMC method for the 2D Fermi polaron compared to the 3D Fermi polaron. We propose different probability distributions to sample new imaginary times for Γ^0-interactions and to sample new momenta for the $G^0_\uparrow$-propagators.

Since $\Gamma^0(\mathbf{p},\tau)$ contains a strongly divergent behavior for $\tau \to 0^+$, it is important to choose a good proposal function $W_1(\tau)$ that allows one to generate small times.

Let us first estimate a typical value of τ if $\Gamma^0(\mathbf{p},\tau)$ is used as a renormalized interaction in the Feynman diagrams. Consider therefore the following integral over the first order expansion for $\tau \to 0$ of $\Gamma^0(\mathbf{p},\tau)$, given in Eq. (3.10) with $\varepsilon_B = 1$:

$$\int_0^{0.1} d\tau \frac{1}{\tau}\frac{1}{\ln^2(\tau)} \,. \tag{3.11}$$

From the following ratio R we can estimate the importance of short time contributions to the integral in Eq. (3.11),

$$R = \frac{\int_0^{\tau_{min}} d\tau \frac{1}{\tau}\frac{1}{\ln^2(\tau)}}{\int_0^{0.1} d\tau \frac{1}{\tau}\frac{1}{\ln^2(\tau)}} \,, \tag{3.12}$$

with the time $\tau_{min} < 0.1$. If we set $\tau_{min} = 10^{-100}$, $R = 0.01$, which means that there is still a significant contribution to the integral in Eq. (3.11) from such small times. To have no loss of accuracy when storing these times on a computer, we sample and keep track of the logarithm of the times. Choosing the probability density $W_1(\tau) \propto \frac{1}{\tau}\frac{1}{\ln^2(\varepsilon_B \tau)}$ allows us to sample the desired times. Sampling a new time $\tau_{new} < \tau_0$ from $W_1(\tau)$ can be done via

$$r = \frac{\int_0^{\tau_{new}} d\tau W_1(\tau)}{\int_0^{\tau_0} d\tau W_1(\tau)} \,, \tag{3.13}$$

$$\ln(\tau_{new}) = \frac{\ln(\varepsilon_B)(1-r) + \ln(\tau_0)}{r} \,, \tag{3.14}$$

with r a random number between 0 and 1. The upper limit τ_0 should be chosen in such a way that $\tau_0 < \frac{1}{\varepsilon_B}$.

We observed that the tail for $\Gamma^0(\mathbf{p},\tau)$ for large times has an exponential decay: $\Gamma^0(\mathbf{p},\tau) \overset{\tau\to\infty}{\sim} e^{-a(\mathbf{p})\tau}$. The coefficients $a(\mathbf{p})$ are determined before we start the similation. To include sampling in the range $[\tau_0, \infty[$ we add a second probability density $W_2(\tau)$. We choose:

$$W_2(\tau) = a(\mathbf{p}) e^{-a(\mathbf{p})\tau} \qquad \text{for } \tau > 0 \,. \tag{3.15}$$

To change the momentum of a forward spin-up propagator we use the following probability density: $W^p(|\mathbf{q}| = q, \phi) = W^p(q)/(2\pi)$, with (q,ϕ) polar coordinates, and

$$W^p(q) \propto q e^{-\frac{\tau}{2m}q^2} \,. \tag{3.16}$$

Notice that $W^p(q,\phi) \propto G^0_\uparrow$ for $q > k_F$, and should therefore be a good proposal function. In the case we want to change the momentum of a forward spin-up propagator, we sample a new momentum $q_{new} > k_F$:

$$r = \frac{\int_{k_F}^{q_{new}} dq W^p(q)}{\int_{k_F}^{\infty} dq W^p(q)} , \tag{3.17}$$

$$q_{new} = \sqrt{\frac{\frac{\tau}{2m}k_F^2 - \ln(1-r)}{\frac{\tau}{2m}}} , \tag{3.18}$$

with r a random number in the range $[0,1]$. If we have a backward spin-up propagator, we propose to change the momentum via

$$W^h(q) \propto q e^{\frac{\tau}{2m}q^2} , \tag{3.19}$$

which is $\propto G^0_\uparrow$ for $q < k_F$. Note that we again use the convention that $\tau > 0$, even for a hole propagator (see Eq. (2.60)). A new $q_{new} < k_F$ is given by:

$$r = \frac{\int_0^{q_{new}} dq W^h(q)}{\int_0^{k_F} dq W^h(q)} , \tag{3.20}$$

$$q_{new} = \sqrt{\frac{\ln(re^{\frac{\tau}{2m}k_F^2} - r + 1)}{\frac{\tau}{2m}}} . \tag{3.21}$$

The angle ϕ is sampled uniformly between 0 and 2π.

3.3 Diagrammatic Monte Carlo Study of the Fermi polaron in two dimensions

This section contains the published results of the 2D Fermi polaron [31]. For the 3D Fermi polaron, a favorable cancellation between the higher-order diagrams was observed. Therefore, the lowest-order approximation already provides a good approximation to the ground-state energy and the Z-factor. Here we will investigate whether this also holds in two dimensions. We will discuss the cancellation of higher-order diagrams for the 2D Fermi polaron in detail and we will point out the differences and similarities with the 3D case.

In Sec. 2.2 we noticed that disconnected diagrams in the Feynman-Dyson perturbation series for the 3D Fermi polaron are absent. Since the topology of the diagrams will not change if we lower the dimension for the Fermi-polaron system, this statement will also hold for the 2D case. We will use this property to establish a direct link between a n-ph variational approach and a DiagMC calculation with a selected class of diagrams. This will enable us to investigate the accurateness of a n-ph variational treatment.

Diagrammatic Monte Carlo study of the Fermi polaron in two dimensions

Jonas Vlietinck[1], Jan Ryckebusch[1], and Kris Van Houcke[1,2]

[1] *Department of Physics and Astronomy, Ghent University, Proeftuinstraat 86, 9000 Gent, Belgium*
[2] *Laboratoire de Physique Statistique, Ecole Normale Supérieure, UPMC, Université Paris Diderot, CNRS, 24 rue Lhomond, 75231 Paris Cedex 05, France*

Abstract

We study the properties of the two-dimensional Fermi polaron model in which an impurity attractively interacts with a Fermi sea of particles in the zero-range limit. We use a diagrammatic Monte Carlo (DiagMC) method which allows us to sample a Feynman diagrammatic series to very high order. The convergence properties of the series and the role of multiple particle-hole excitations are discussed. We study the polaron and molecule energy as a function of the coupling strength, revealing a transition from a polaron to a molecule in the ground state. We find a value for the critical interaction strength which complies with the experimentally measured one and predictions from variational methods. For all considered interaction strengths, the polaron Z factor from the full diagrammatic series almost coincides with the one-particle-hole result. We also formally link the DiagMC and the variational approaches for the polaron problem at hand.

1 Introduction

Experiments with ultracold gases are a powerful tool to investigate the (thermo)-dynamics of quantum many-body systems under controlled circumstances. With Feshbach resonances [1][1], for example, one has the ability to tune the interaction strength. Optical potentials [2] can be exploited to modify the dimensionality of the studied systems. The properties of a single impurity that interacts strongly with a background gas, for example, can be addressed with ultracold atoms.

The so-called Fermi polaron problem refers to a single spin-down impurity that is coupled to a non-interacting spin-up Fermi sea (FS). This problem corresponds to the extreme limit of spin imbalance in a two-component Fermi gas [3, 4, 5] and has implications on the phase diagram of the strongly spin-polarized Fermi gas [6, 34, 8]. At weak attraction, one expects a "polaron" state [9], in which the impurity is dressed with density fluctuations of the spin-up Fermi gas. Recent experiments have observed indications of a transition from this polaronic state to a molecular state (a two-body bound state of the impurity and an

[1] The references of the citations in this text are located at the end of this chapter

atom of the sea) upon increasing the attraction strength in three dimensions (3D) [10] and in two dimensions (2D) [11]. Experimentally, the 2D regime can be accomplished by means of a transverse trapping potential $V(z) = \frac{1}{2}m\omega_z^2 z^2$ (here, ω_z is the frequency and z is the transverse direction) that fulfills the condition $k_B T \ll \epsilon_F \ll \hbar\omega_z$ (T is the temperature and ϵ_F is the Fermi energy of the FS). When excitations in the z dimension are possible, one reaches the so-called quasi-2D regime [13, 12]. The purely 2D limit is reached for $\epsilon_F/\hbar\omega_z \to 0$ and will be the subject of this paper.

The existence of a polaron-molecule transition in 3D has been predicted with the aid of the diagrammatic Monte Carlo (DiagMC) method [14, 15, 16] and of variational methods [9, 17, 18, 19]. For the latter, the maximum number of particle-hole (p-h) excitations of the FS is limited to one or two [9, 17, 18, 19]. One might naively expect that the role of quantum fluctuations increases in importance with decreasing dimensionality and that high-order p-h excitations could become more important in one and two dimensions. For the one-dimensional (1D) Fermi polaron the known analytical solution displays no polaron-molecule transition [20]. Like for the 3D polaron, the approximate method in which the truncated Hilbert space contains one p-h and two p-h excitations of the FS gives results for the 1D polaron approaching the exact solution [21, 22]. In 2D, the Fermi polaron properties have been studied with variational wave functions [23, 24, 25]. To observe a polaron-molecule transition in 2D it is crucial to include particle-hole excitations in both the polaron and molecule wave functions [24]. In the limit of weak interactions, the 1p-h and 2p-h variational Ansätze for the polaron branch provide similar results. Surprisingly, this is also the situation for strong correlations [25].

In this work we focus on the 2D Fermi polaron for attractive interactions and study the role of multiple particle-hole (mp-h) excitations for the ground-state properties of the system. The quasiparticle properties of the polaron are computed with the DiagMC method. This technique evaluates stochastically to high order a series of Feynman diagrams for the one-particle and two-particle self-energies. For the details of the DiagMC method and the adopted method for determining the ground-state energies from the computed self-energies, we refer to Refs. [16, 15]. In this work we present DiagMC predictions for the interaction-strength dependence of the polaronic and molecular ground-state properties in 2D. We first briefly discuss the model and the diagrammatic method. We then discuss the results of the simulations, with particular emphasis on the role of the mp-h excitations. We also discuss how variational results for the polaron problem can be obtained within the DiagMC formalism.

2 Formalism

We consider a two-component Fermi gas confined to 2D at temperature $T = 0$. Even though we will consider the zero-range interaction in continuous space, we start from a lattice model to avoid ultraviolet divergences from the onset. The corresponding Hamiltonian reads

$$\hat{H} = \sum_{\mathbf{k}\in\mathcal{B},\sigma=\uparrow\downarrow} \epsilon_{\mathbf{k}\sigma}\ \hat{c}^\dagger_{\mathbf{k}\sigma}\hat{c}_{\mathbf{k}\sigma} + g_0 \sum_{\mathbf{r}} b^2\ \hat{\Psi}^\dagger_\uparrow(\mathbf{r})\hat{\Psi}^\dagger_\downarrow(\mathbf{r})\hat{\Psi}_\downarrow(\mathbf{r})\hat{\Psi}_\uparrow(\mathbf{r})\ , \tag{1}$$

with $\hat{\Psi}_\sigma(\mathbf{r})$ and $\hat{c}_{\mathbf{k},\sigma}$ being the operators for annihilating a spin-σ fermion with mass m_σ and dispersion $\epsilon_{\mathbf{k}\sigma} = k^2/2m_\sigma$ in position and momentum space. The components of the position vector $\mathbf{r}$ are integer multiples of the finite lattice spacing b. Further, g_0 is the bare interaction strength. The wave vectors $\mathbf{k}$ are in the first Brillouin zone $\mathcal{B} =]-\pi/b, \pi/b]$. The continuum limit is reached for $b \to 0$. We adopt the convention $\hbar = 1$ and consider the mass-balanced case $m_\uparrow = m_\downarrow = m$. We make use of the T matrix [26] for a single spin-$\uparrow$ and spin-$\downarrow$ fermion in vacuum,

$$-\frac{1}{g_0} = \frac{1}{\mathcal{V}} \sum_{\mathbf{k}\in\mathcal{B}} \frac{1}{\varepsilon_B + \epsilon_{\mathbf{k}\uparrow} + \epsilon_{\mathbf{k}\downarrow}} , \tag{2}$$

where $\mathcal{V}$ is the area of the system and ε_B is the two-body binding energy [which depends on m, g_0, and b and $\varepsilon_B(m, g, b) > 0$] of a weakly bound state. Such a state always exists for an attractive interaction in 2D. With the above relation we eliminate the bare interaction strength g_0 in favor of the quantity ε_B. Moreover, the diagrammatic approach allows us to take the continuum limit $b \to 0$ and $g_0 \to 0^-$ while keeping ε_B fixed. Summing all ladder diagrams gives a partially dressed interaction vertex Γ^0:

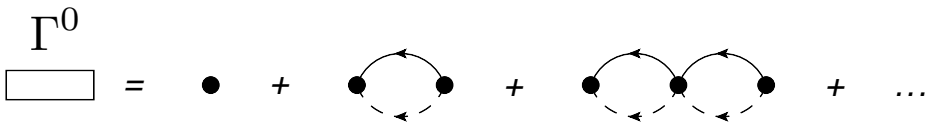

, (3)

where the dot represents the bare interaction vertex g_0 and the lines represent bare-particle propagators for the spin-down impurity (dashed lines) and the spin-up Fermi sea (solid lines). In momentum-imaginary frequency this graphical representation corresponds to

$$[\Gamma^0(p, i\Omega)]^{-1} = g_0^{-1} - \Pi^0(p, i\Omega) , \tag{4}$$

with

$$\Pi^0(p, i\Omega) = \frac{1}{\mathcal{V}} \sum_{\mathbf{k}\in\mathcal{B}} \frac{\theta(|\frac{\mathbf{p}}{2} + \mathbf{k}| - k_F)}{i\Omega - \epsilon_{\frac{\mathbf{p}}{2}-\mathbf{k}\downarrow} - \epsilon_{\frac{\mathbf{p}}{2}+\mathbf{k}\uparrow} + \mu + \varepsilon_F} , \tag{5}$$

with $\theta(x)$ being the Heaviside step function and $\mu < 0$ being a free parameter representing an energy offset of the impurity dispersion. Further, k_F and $\varepsilon_F = \frac{k_F^2}{2m}$ are the Fermi momentum and the Fermi energy of the spin-up sea. The combination of Eqs. (2) and (4) gives

$$\frac{1}{\Gamma^0(p, i\Omega)} = -\frac{1}{\mathcal{V}} \sum_{\mathbf{k}\in\mathcal{B}} \left[\frac{1}{\varepsilon_B + \epsilon_{\mathbf{k}\uparrow} + \epsilon_{\mathbf{k}\downarrow}} + \frac{\theta(|\frac{\mathbf{p}}{2} + \mathbf{k}| - k_F)}{i\Omega - \epsilon_{\frac{\mathbf{p}}{2}-\mathbf{k}\downarrow} - \epsilon_{\frac{\mathbf{p}}{2}+\mathbf{k}\uparrow} + \mu + \varepsilon_F} \right] . \tag{6}$$

The relevant parameter that characterizes the interaction in Eq. (6) is ϵ_B. Equation (6) is well defined in the thermodynamic and $b \to 0$ limits. One finds

$$\frac{1}{\Gamma^0(p, i\Omega)} = \frac{m}{4\pi} \ln\left[\frac{2\varepsilon_B}{-z + \sqrt{(z - \epsilon_{\mathbf{p}})^2 - 4\varepsilon_F \epsilon_{\mathbf{p}}}} \right] , \tag{7}$$

with $z \equiv i\Omega + \mu - \varepsilon_F$. In deriving the above expression for $\Gamma^0(p, i\Omega)$ we have taken $\mu < -\varepsilon_F$. Since Feynman diagrams for the self-energy will be evaluated in the momentum-imaginary-time representation (p, τ), we need to evaluate the Fourier transform

$$\Gamma^0(p,\tau) = \frac{1}{2\pi}\int_{-\infty}^{+\infty} d\Omega\; e^{-i\Omega\tau}\; \Gamma^0(p, i\Omega)\;. \tag{8}$$

In order to determine the leading behavior of $\Gamma^0(p,\tau)$ for small τ, we introduce the vertex function $\tilde{\Gamma}^0$, which differs from Γ^0 by ignoring the Fermi surface when integrating out the internal momenta. This amounts to ignoring the Heaviside function in Eq. (5). We obtain

$$\frac{1}{\tilde{\Gamma}^0(p, i\Omega)} = \frac{m}{4\pi}\;\ln\left[-\frac{\varepsilon_B}{i\Omega + \mu + \varepsilon_F - \frac{\epsilon_{\mathbf{p}}}{2}}\right]. \tag{9}$$

In the $(p, i\Omega)$-representation,

$$\frac{1}{\Gamma^0} - \frac{1}{\tilde{\Gamma}^0} = \frac{m}{4\pi}\ln\left[\frac{-2(z+2\varepsilon_F)+\epsilon_{\mathbf{p}}}{-z+\sqrt{(z-\epsilon_{\mathbf{p}})^2 - 4\varepsilon_F\epsilon_{\mathbf{p}}}}\right]. \tag{10}$$

The (p,τ) representation of $\tilde{\Gamma}^0$ is

$$\begin{aligned}\tilde{\Gamma}^0(p,\tau) \;\;=\;\; & -\frac{4\pi\varepsilon_B}{m}e^{-(\frac{\epsilon_{\mathbf{p}}}{2}-\varepsilon_F-\mu)\tau}\;\left[\int_0^{+\infty} dx \frac{e^{-x\varepsilon_B\tau}}{\pi^2+\ln^2(x)}\right. \\ & \left. +\; e^{\varepsilon_B\tau}\theta(\frac{\epsilon_{\mathbf{p}}}{2}-\varepsilon_F-\varepsilon_B-\mu)\right]\;\theta(\tau)\end{aligned} \tag{11}$$

for $\mu < -\varepsilon_F - \varepsilon_B$, ensuring that only $\tau > 0$ contributes for all momenta p. The integral in Eq. (11) can be computed numerically, but converges poorly for $\tau \to 0^+$. Under those conditions we make use of the asymptotic behavior:

$$\int_0^{+\infty} dx \frac{e^{-x\varepsilon_B\tau}}{\pi^2+\ln^2(x)} \underset{\tau\to 0}{\sim} \frac{1}{\varepsilon_B\tau}\frac{1}{\ln^2(\varepsilon_B\tau)}\;. \tag{12}$$

To obtain $\Gamma^0(p,\tau)$ we computed numerically the following Fourier transform:

$$\Gamma^0(p,\tau) - \tilde{\Gamma}^0(p,\tau) = \frac{1}{2\pi}\int_{-\infty}^{+\infty} d\Omega\; e^{-i\Omega\tau}\left[\Gamma^0(p,i\Omega) - \tilde{\Gamma}^0(p,i\Omega)\right]\;. \tag{13}$$

The left-hand side of Eq. (13) can be computed more easily than $\tilde{\Gamma}^0(p,\tau)$ as it contains no singularities. Next, the function $\Gamma^0(p,\tau)$ is obtained as $\tilde{\Gamma}^0(p,\tau) + \left[\Gamma^0(p,\tau) - \tilde{\Gamma}^0(p,\tau)\right]$. Although the functions $\tilde{\Gamma}^0(p,\tau)$ and $\Gamma^0(p,\tau)$ are extremely sharp and divergent for $\tau \to 0$, they are integrable. Special care should be taken when using these functions in the Monte Carlo code. It is important to correctly sample very short times, and one needs to make sure there is no loss of accuracy when keeping track of imaginary time differences of the Γ^0 lines in the diagrams. Just like for the 3D polaron problem [14, 15, 16], we consider a diagrammatic series for the self-energy built from the free one-body propagators for the impurity and the spin-up Fermi sea and from the renormalized interaction Γ^0. We refer to this series as the

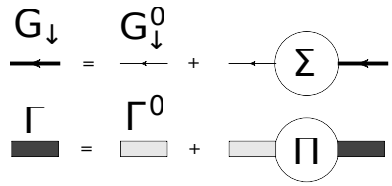

Figure 1 – Graphical representation of the Dyson equation. The free (dressed) one-body impurity propagator is denoted by $G^0_\downarrow$ ($G_\downarrow$). Σ and Π are the one-body and two-body self-energies, respectively. Γ is the fully dressed interaction, whereas Γ^0 is the partially dressed interaction as shown in Eq. (3).

bare series, which we evaluate with the DiagMC method. The diagram topologies in 2D and 3D are exactly the same. The major differences between the diagrammatic-series evaluations in 2D and 3D are the renormalized interaction $\Gamma^0(p,\tau)$ and the phase-space volume elements. The one and two-body self-energies are related to the one-particle propagator G and the fully dressed interaction Γ by means of a Dyson equation, as illustrated schematically in Fig. 1. From the poles of G and Γ we can extract the polaron and the molecule energy, respectively. The fully dressed interaction is closely related to the two-particle propagator [16].

For the 3D Fermi polaron problem there are two dominant diagrams at each given order that emerge next to many diagrams with a much smaller contribution [16]. These dominant diagrams contribute almost equally but have opposite sign. In 2D, however, the numerical calculations indicate that at a given order the very same two diagrams dominate, but to a lesser extent; that is, the nondominant diagrams have a larger weight in the final 2D result. By *weight* of a given diagram we mean the absolute value of its contribution to the self-energy. We note that the sign of a single diagram at fixed internal and external variables depends only on its topology and not on the values of the internal and external variables. We stress that this is not true for a Fermi system with two interacting components with finite density [27, 28]. In 2D the total weight of a given order (i.e., the sum of the absolute values of the contributions of diagrams) is distributed over more diagrams than in 3D. Because the sign alternation occurs over a broader distribution of the weights, we get more statistical noise in sampling the self-energy in 2D compared to 3D. In 3D we can evaluate the diagrammatic series for the one-body self-energy accurately up to order 12, whereas in 2D we can reach order 8.

In principle, other choices for the propagators ("bare" versus "dressed" propagators) are possible, and this was discussed in detail for the 3D Fermi polaron in our previous paper [16]. Replacing the bare propagators by dressed ones reduces the number of diagrams at each given order. One may expect that this replacement could allow one to reach higher orders. For the 3D polaron, however, the most favorable conditions of cancellations between the contributions from the various diagrams were met in the bare scheme [16]. In the DiagMC framework a higher accuracy can be reached under conditions of strong cancellations between the various contributions. From numerical investigations with various propagators for the 2D Fermi polaron we could draw similar conclusions as in the 3D studies. Accordingly, all numerical results for the quasiparticle properties presented below are obtained for a series expansion with bare propagators.

To characterize the magnitude of the interaction strength we use the dimensionless parameter $\eta \equiv \ln[k_F a_{2D}] = \ln[2\varepsilon_F/\varepsilon_B]/2$. Here, $a_{2D} > 0$ is the 2D scattering length, related to the

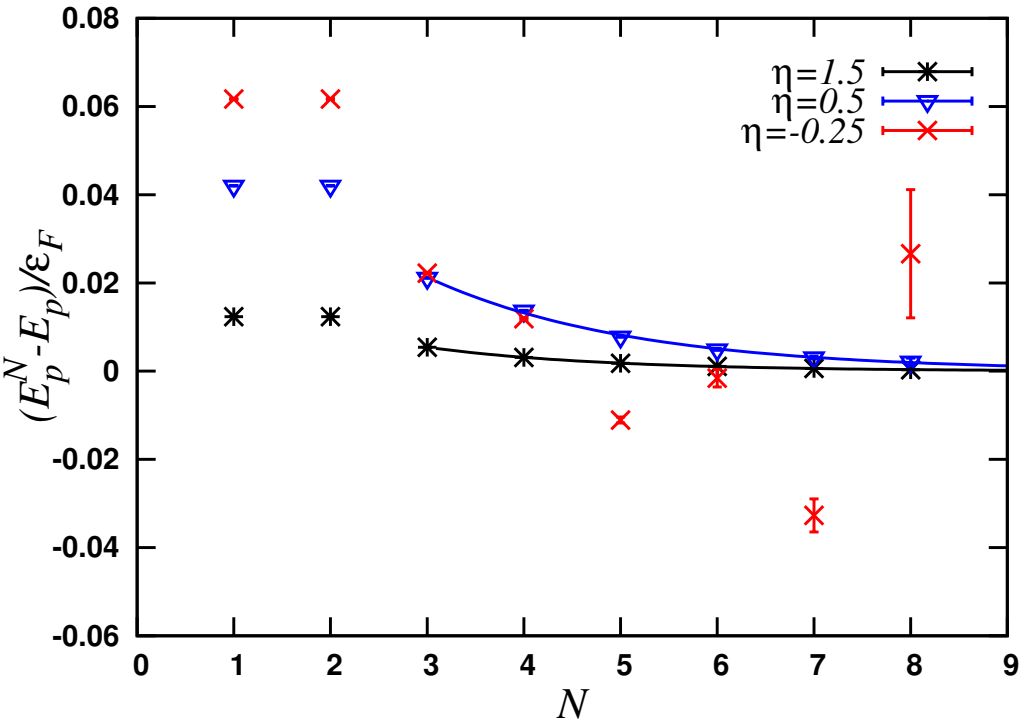

Figure 2 – Dependence of the polaron energy E_p^N on the cutoff diagram order N. E_p is the value obtained after extrapolation to $N \to +\infty$ (and resummation for $\eta = -0.25$). Results are shown for $\eta = -0.25, \eta = 0.5, \eta = 1.5$. The lines represent an exponential fit.

dimer binding energy by $\varepsilon_B = 1/(2m_r a_{2D}^2)$ with $m_r = m_\uparrow m_\downarrow/(m_\uparrow + m_\downarrow)$ being the reduced mass. The BCS regime corresponds to $\eta \gg 1$ while the Bose-Einstein condensate (BEC) regime corresponds to $\eta \ll -1$. The system is perturbative in the regimes $|\eta| \gg 1$, while the strongly correlated regime corresponds to $|\eta| \lesssim 1$. [29] In the weak-coupling regime [small interaction strengths g_0 in the Hamiltonian of Eq. (1) or large positive η in the zero-range limit], we find that the one-body and the two-body self-energy Σ and Π converge absolutely as a function of the maximum diagram order. This is demonstrated in Fig. 2 for $\eta = 1.5$, where the polaron energy E_p^N converges exponentially as a function of the cutoff diagram order N. Similar convergence is also found for the molecule energy. Under conditions of convergence with diagram order, extrapolation to order infinity can be done in a trivial way. Similar convergence is also seen for $\eta = 0.5$. In the strongly correlated regime the series starts oscillating with order when $\eta \lesssim 0$, and the oscillations get stronger the deeper we go into the BEC regime. The oscillations in the extracted polaron energy are illustrated in Fig. 2 for $\eta = -0.25$. To obtain meaningful results we rely on Abelian resummation techniques [16, 27]. We evaluate the series $\sigma_\epsilon = \sum_N \sigma^{(N)} e^{-\epsilon\lambda_N}$, with σ^N being the one-body self-energy for diagram order N and λ_N being a function that depends on the diagram order N. For each ϵ the polaron energy E_p is calculated from σ_ϵ and an extrapolation is done by taking the limit $\epsilon \to 0$. The whole procedure is illustrated in Fig. 3. To estimate the systematic error of the extrapolation procedure, different resummation functions λ_N are used. As becomes

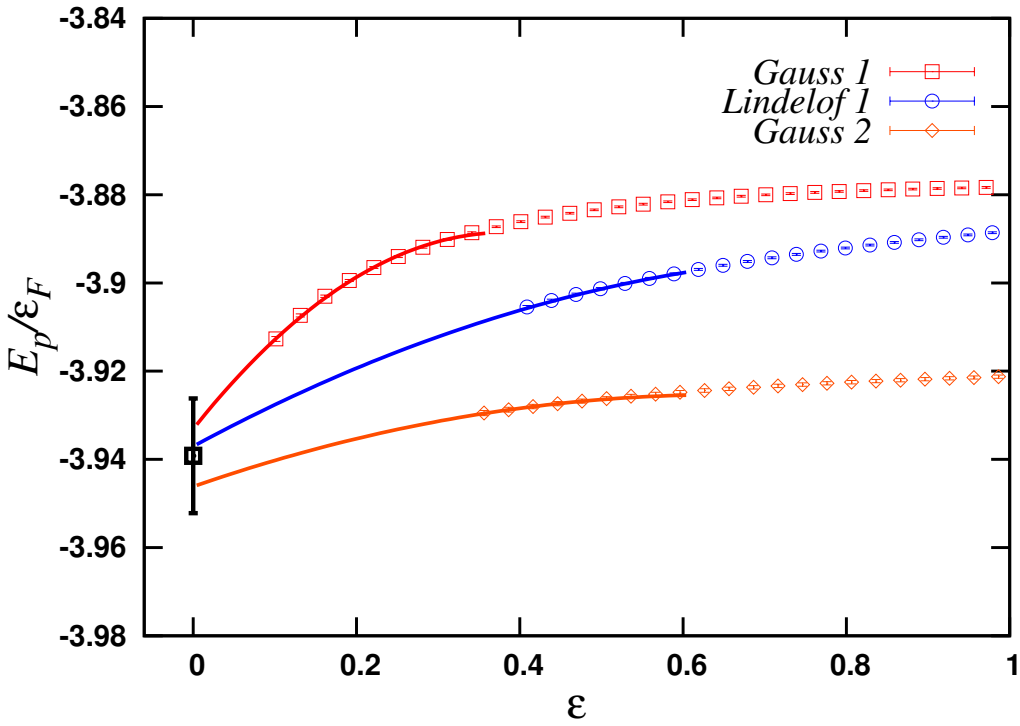

Figure 3 – Abelian resummation of the bare series for the one-body self-energy diagrams at $\eta = -0.25$. We evaluate $\sigma_\epsilon = \sum_N \sigma^{(N)} e^{-\epsilon\lambda_N}$, with σ^N being the one-body self-energy for diagram order N. We use the following functions λ_N : (i) Gauss 1: $\lambda_N = (N-1)^2$ for $N > 1$ and $\lambda_N = 0$ for $N = 1$, (ii) Lindelöf 1: $\lambda_N = (N-1)\log(N-1)$ for $N > 2$ and $\lambda_N = 0$ for $N \leq 2$, and (iii) Gauss 2: $\lambda_N = (N-3)^2$ for $N > 3$ and $\lambda_N = 0$ for $N \leq 3$. The polaron energy E_p/ϵ_F is extracted in the limit $\epsilon = 0^+$ for various choices of λ_N.

clear from Fig. 3 the whole resummation procedure is a stable one and induces uncertainties on the extracted energies of the order of a few percent. All the results of Fig. 4 are obtained with the Abelian resummation technique. The stronger the coupling constant is the larger the size of the error attributed to the resummation. An accurate extrapolation to infinite diagram order could be achieved for all values of η.

3 Results and discussion

In Fig. 4, polaron and molecule energies are displayed for a wide range of the parameter η. DiagMC results include all diagrams up to order 8 and extrapolation to the infinite diagram order. In the region $\eta \lesssim 0$ a small discrepancy (of the order of 0.1% of the ground-state energy) is found with the variational results [25] of Parish and Levinsen based on the wave-function Ansatz up to 2p-h excitations. Clearly, a phase transition appears at the critical value $\eta_c = -0.95 \pm 0.15$. A variational result which includes 2p-h excitations for the polaron

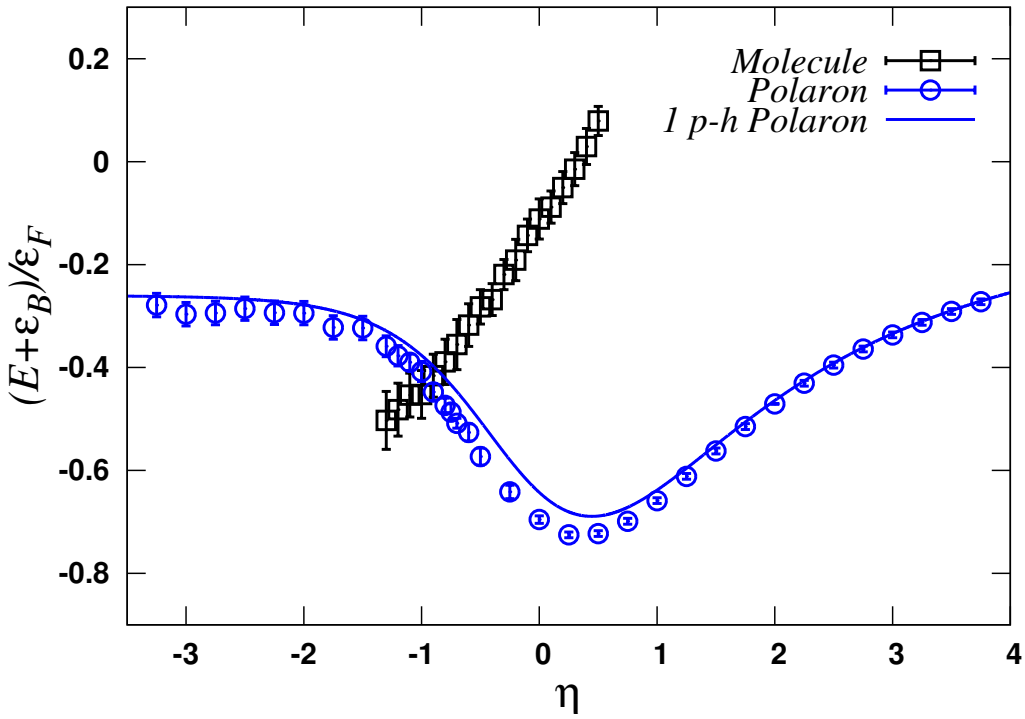

Figure 4 – Polaron and molecule ground-state energies E in units of the Fermi energy ε_F as a function of η. The momentum of the impurity is equal to zero. Energies are shifted by the two-body binding energy $\varepsilon_B/\varepsilon_F = 2e^{-2\eta}$ to magnify the details. The solid line is the DiagMC result for $N = 1$. The symbols are the result of the full DiagMC calculations (including diagrams up to order 8).

and 1p-h excitations for the molecule, gives $\eta = -0.97$. [25] Both mentioned calculations are in agreement with the experimental result $\eta = -0.88(0.20)$ [11].

The DiagMC method allows one to include a large number of particle-hole excitations that dress the impurity. Truncation of the Hilbert space to a maximum number of p-h pairs can nonetheless be achieved within the DiagMC approach. This allows one to arrive at the variational formulation. Previous variational studies using a wave function Ansatz up to 1p-h or 2p-h excitations showed that these truncations give remarkably accurate results [30].

To understand why the truncation is possible within a Feynman diagrammatic approach for the self-energy, we first remark that a variational approach is easily established within a path-integral formalism. Path integrals with continuous imaginary time, for example, are based on an expansion of the evolution operator,

$$e^{-\beta\hat{K}} = e^{-\beta\hat{K}_0}\big(1 - \int_0^\beta d\tau_1 K_1(\tau_1) + \int_0^\beta d\tau_1 \int_0^{\tau_1} d\tau_2\ \hat{K}_1(\tau_1)\hat{K}_1(\tau_2) - \dots\big)\ , \qquad (14)$$

where $\hat{K} = \hat{H} - \mu\hat{N} = \hat{K}_0 + \hat{K}_1 - \mu\hat{N}$, with $\left[\hat{K}_0, \hat{K}_1\right] \neq 0$. The operator $\hat{K}_1(\tau) = e^{\hat{K}_0\tau}\hat{K}_1 e^{-\hat{K}_0\tau}$, which defines the series expansion, is expressed in the interaction picture.

Further, $\beta = 1/k_B T$, with k_B being Boltzmann's constant and T being temperature, $\hat{H}$ is the Hamiltonian, $\hat{N}$ the number operator, and μ is the chemical potential. The imaginary-time evolution operator in Eq. (14) can be used as a ground-state projection operator: for sufficiently long imaginary time β the excited-state components of a trial state are exponentially suppressed. One typically evaluates all the terms in the expansion equation (14) in the eigenbasis of $\hat{K}_0$. This procedure forms the basis of path-integral Monte Carlo simulation of lattice models, where $\hat{K}_1$ is usually the kinetic energy term [31]. A discretized time version is used in path-integral Monte Carlo methods in continuous space [32, 33]. Either way, the contributions to the path integral have the direct physical interpretation of a time history of the many-particle system. At each instant of time, one can constrain the accessible states of the Hilbert space, in line with what is done in a variational approach. Within the standard Feynman diagrammatic formalism for Green's functions, however, this truncation of the Hilbert space is not easy to accomplish for an arbitrary system, as one expands in powers of the two-body interaction term of the Hamiltonian. This will be explained in the next paragraph.

It turns out to be formally easier to start from finite T and to take the $\beta \to \infty$ limit in the end. For a many-fermion system, the finite-temperature Green's function in position and imaginary-time representation $(\mathbf{x}, \tau)$ is defined as

$$G_{\alpha\sigma}(\mathbf{x}, \tau) = -\frac{\mathrm{Tr}[e^{-\beta \hat{K}} T_\tau \hat{\psi}_{H\alpha}(\mathbf{x}, \tau) \hat{\psi}^\dagger_{H\sigma}(\mathbf{x}, 0)]}{\mathrm{Tr}[e^{-\beta \hat{K}}]} \,, \tag{15}$$

with α and σ denoting an appropriate set of quantum numbers (such as spin) and T_τ being the time-ordering operator. The field operator in the Heisenberg picture $\hat{\psi}_{H\alpha}(\mathbf{x}, \tau) = e^{\hat{K}\tau} \hat{\psi}_\alpha(\mathbf{x}) e^{-\hat{K}\tau}$ annihilates a fermion in state α at position $\mathbf{x}$ and time τ. To arrive at the Feynman diagrammatic expansion, one makes a perturbative expansion for the evolution operator $e^{-\beta \hat{K}}$ in both the numerator *and* the denominator of Eq. (15) (the finite T ensures that both exist). The expansion of the partition function Z in the denominator can be represented graphically by the series of all fully closed diagrams (connected and disconnected). When β approaches $+\infty$, the denominator is proportional to $\langle \Psi_0 | \Psi_0 \rangle$ ($|\Psi_0\rangle$ is the ground state of the interacting many-body system), and the disconnected diagrams correspond to all possible vacuum fluctuations of the system at hand. The expansion in the numerator factorizes into an expansion of connected diagrams for $G_{\alpha\sigma}$ and disconnected diagrams for Z. So the sum of disconnected diagrams drops out, as expected for an intensive quantity like $G_{\alpha\sigma}(\mathbf{x}, \tau)$. It is exactly this factorization that prevents one from truncating the Hilbert space at any instant of time in the evolution. In other words, variational calculations based on Feynman diagrams for the self-energy are generally not feasible.

In the polaron problem vacuum fluctuations are absent since $|\Psi_0\rangle$ corresponds to the spin-down vacuum and a non-interacting spin-up Fermi sea. In other words, the vacuum cannot be polarized in the absence of an impurity. As a consequence, we face a situation similar to the path integral with a direct physical interpretation of the time history of the impurity. This peculiar feature allows one to restrict the Hilbert space at each given time. If we allow at most 1p-h excitations at each instant of time, only one diagram survives: the lowest-order self-energy diagram built from Γ^0 and the free spin-up single-particle propagator $G^0_\uparrow$. The equivalence between this diagram and the 1p-h variational approach had already been pointed out in Ref. [21]. An np-h variational approach is achieved by allowing at most n backward spin-up lines at each step in the imaginary-time evolution.

For large η it is obvious from Fig. 4 that the polaron energy from the full series expansion becomes equal to the 1p-h result. Even for stronger interactions (smaller η) the first-order results remain close to the full DiagMC one. Within the statistical accuracy of the numerical calculations, convergence for the one-body self-energy is already reached after inclusion of 2p-h excitations. Indeed, for all values of η, we find agreement between our 2p-h variational DiagMC approach and the full DiagMC approach within statistical error bars. For the molecular branch, we retrieve the result for the two-body self-energy from the full series expansion after including 1p-h excitations. For the 3D Fermi-polaron a similar conclusion was drawn. Also in 3D, the first-order result is a very good approximation [16]. Going up to 2p-h pairs gives a perfect agreement with full DiagMC results. From the above considerations it follows, however, that the diagrammatic truncations which provide good results for the polaron problem may not be appropriate for the more complex many-body problem with comparable densities for both components.

The quasiparticle residue or Z factor of the polaron gives the overlap of the noninteracting wave function and the fully interacting one. This overlap is very small for a molecular ground state of the fully interacting system [16]. The Z factor as a function of η is shown in Fig. 5. Note that the polaron Z factor does not vanish in the region $\eta \lesssim -1$ where the ground state is a molecule. The Z factor is, however, still meaningful since the polaron is a well-defined (metastable) excited state of the 2D system. Again, the first-order result gives a good approximation to the full result. The measured Z factor for the 3D situation has been reported in Ref. [34, 10]. The 2D experimental data are reported in Ref. [11], and the η dependence of the quasiparticle weight Z is presented in arbitrary units. We reproduce the observation that Z strongly increases between $\eta_c \lesssim \eta \lesssim 1$ and saturates to a certain value for $\eta > 1$.

4 Conclusion

Summarizing, we have developed a framework to study with the DiagMC method the ground-state properties of the 2D Fermi polaron for attractive interactions. We have shown that the framework allows one to select an arbitrary number of np-h excitations of the FS, thereby making a connection with typical variational approaches which are confined to n=1 and n=2. We have studied the quasiparticle properties of the ground state for a wide range of interaction strengths. A phase transition between the polaron and molecule states is found at interaction strengths compatible with experimental values and with variational predictions. To a remarkable degree, it is observed that for all interaction strengths the full DiagMC results (which include all np-h excitations) for the ground-state properties can be reasonably approximated by n=1 truncations. In a n=2 truncation scheme the full result is already reached within the error bars. This lends support for variational approaches to the low-dimensional polaron problem, for which one could have naively expected a large sensitivity to quantum fluctuations.

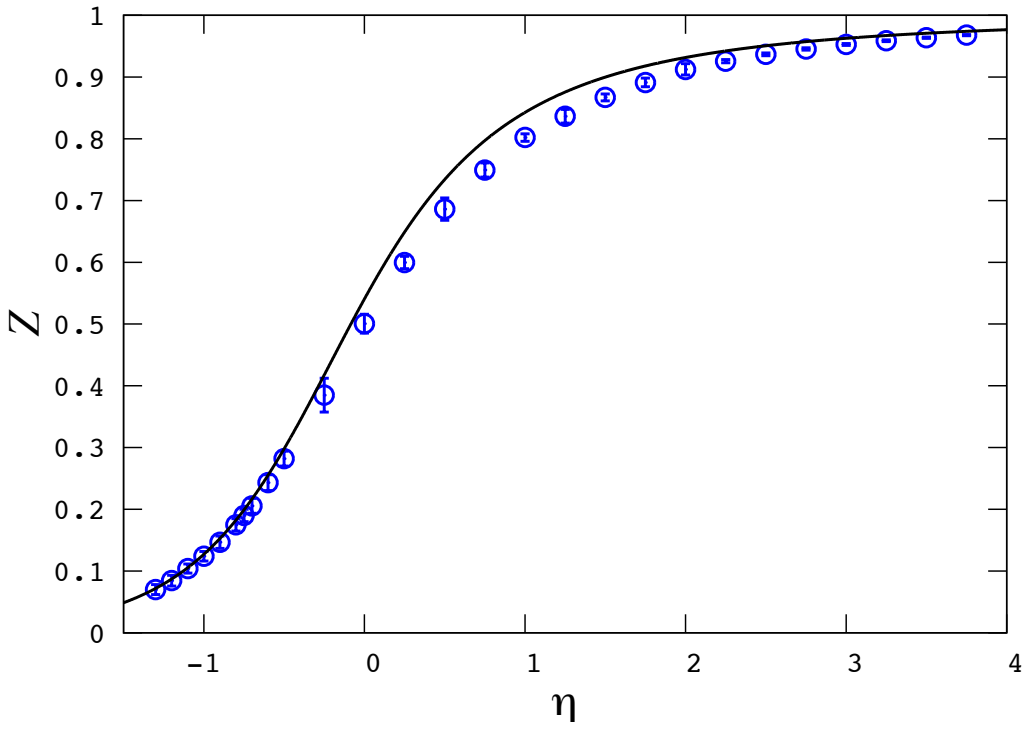

Figure 5 – The quasiparticle residue Z of the polaron as a function of η. The solid line represents the 1p-h result ($N = 1$ diagram).

Acknowledgments

This work is supported by the Fund for Scientific research - Flanders. We would like to thank C. Lobo, N. Prokof'ev, B. Svistunov, and F. Werner for helpful discussions and suggestions, and we thank J. Levinsen and M. Parish for sending us their data.

References

[1] C. Chin, R. Grimm, P. Julienne and E. Tiesinga, Rev. Mod. Phys. **82**, 1225 (2010).

[2] I. Bloch, Nat. Phys. **1**, 23 (2005).

[3] G.B. Partridge, W. Li, Y.A. Liao, R.G. Hulet, M. Haque and H.T.C. Stoof, Phys. Rev. Lett. **97**, 190407 (2006).

[4] Y. Shin, C.H. Schunck, A. Schirotzek and W. Ketterle, Nature (London)**451**, 689 (2008).

[5] S. Nascimbène, N. Navon, K.J. Jiang, L. Tarruell, M. Teichmann, J. McKeever, F. Chevy and C. Salomon, Phys. Rev. Lett. **103**, 170402 (2009).

[6] S. Pilati and S. Giorgini, Phys. Rev. Lett. **100**, 030401 (2008).

[7] P. Massignan, Z. Yu and G.M. Bruun, Phys. Rev. Lett. **110**, 230401 (2013).

[8] G. Bertaina and S. Giorgini, Phys. Rev. Lett. **106**, 110403 (2011).

[9] F. Chevy, Phys. Rev. A **74**, 063628 (2006).

[10] A. Schirotzek, C.-H. Wu, A. Sommer, and M. W. Zwierlein, Phys. Rev. Lett. **102**, 230402 (2009).

[11] M. Koschorreck, D. Pertot, E. Vogt, B. Fröhlich, M. Feld and M. Köhl, Nature (London) **485**, 619 (2012).

[12] P. Dyke ,E. D. Kuhnle, S. Whitlock, H. Hu ,M. Mark, S. Hoinka, M. Lingham, P. Hannaford and C.J. Vale, Phys. Rev. Lett.**106**, 105304 (2011).

[13] J. Levinsen and S. K. Baur, Phys. Rev. A **86**, 041602 (2012).

[14] N.V. Prokof'ev and B.V. Svistunov, Phys. Rev. B **77**, 020408 (2008).

[15] N.V. Prokof'ev and B.V. Svistunov, Phys. Rev. B **77**, 125101 (2008).

[16] J. Vlietinck, J. Ryckebusch and K. Van Houcke, Phys. Rev. B **87**, 115133 (2013).

[17] M. Punk, P.T. Dumitrescu and W. Zwerger, Phys. Rev. A **80**, 053605 (2009).

[18] R. Combescot, S. Giraud and X. Leyronas, EPL **88**, 60007 (2009).

[19] C. Mora and F. Chevy, Phys. Rev. A **80**, 033607 (2009).

[20] J.B. McGuire, J. Math. Phys. **7**, 123 (1966).

[21] R. Combescot, A. Recati, C. Lobo and F. Chevy, Phys. Rev. Lett. **98**, 180402 (2007).

[22] S. Giraud and R. Combescot, Phys. Rev. A **79**, 043615 (2009).

[23] S. Zöllner, G.M. Bruun and C.J. Pethick, Phys. Rev. A **83**, 021603(R) (2011).

[24] M.M. Parish, Phys. Rev. A **83**, 051603(R) (2011).

[25] M.M. Parish and J. Levinsen, Phys. Rev. A **87**, 033616 (2013).

[26] L.D. Landau and E.M. Lifshitz, *Statistical Physics* (Pergamon, New York, 1980), Vol.2.

[27] K. Van Houcke, F. Werner, E. Kozik, N. Prokof'ev, B. Svistunov, M.J.H. Ku, A.T. Sommer, L.W. Cheuk, A. Schirotzek and M.W. Zwierlein, Nat. Phys. **8**, 366 (2012).

[28] K. Van Houcke, F. Werner, N. Prokof'ev and B. Svistunov, arXiv:1305.3901.

[29] P. Bloom, Phys. Rev. B **12**, 125 (1975).

[30] R. Combescot and S. Giraud, Phys. Rev. Lett. **101**, 050404 (2008).

[31] N.V. Prokof'ev, B.V. Svistunov and I.S. Tupitsyn, J. Exp. Theor. Phys. **87**, 310 (1998).

[32] D.M. Ceperley, Rev. Mod. Phys. **67**, 279 (1995).

[33] M. Boninsegni, N. Prokof'ev and B. Svistunov, Phys. Rev. Lett. **96**, 070601 (2006).

[34] C. Kohstall, M. Zaccanti, M. Jag, A. Trenkwalder, P. Massignan, G.M. Bruun, F. Schreck, and R. Grimm, Nature (London) **485**, 615 (2012)

CHAPTER 4

Large Bose polarons

In Sec. 1.3.3 we introduced the BEC-polaron system and showed that it can be described by a Fröhlich type of Hamiltonian if the Bogoliubov approximation is valid. A polaron system which can be described by a Fröhlich type of Hamiltonian will be called a large polaron. To calculate the properties of this system, we again make use of a Feynman diagrammatic series. Before we start discussing the results of the BEC-polaron, we first present some properties for the series of the Fröhlich Hamiltonian. In Sec. 4.1 we show how diagrams are constructed. In Sec. 4.2 we give a short presentation of the DiagMC method to evaluate the diagrammatic series.

4.1 Feynman diagrams for large polarons

In Sec. 2.2 we considered a series of Feynman diagrams for the Fermi polaron. A similar strategy can be followed to set up a diagrammatic series for the Fröhlich Hamiltonian. Since $\hat{H}_{pol}^{IB}$ (see Eq. (1.6)) has a different structure than $\hat{H}_{\downarrow\uparrow}$ (see Eq. (1.25)), we expect here a different type of diagrams than in the Fermi polaron case. The Feynman-Dyson perturbation series for the one-particle Green's function $G(\mathbf{p}, \tau)$, with $\mathbf{p}$ the momentum of the impurity and τ the imaginary time, is given by:

$$\begin{aligned} G(\mathbf{p},\tau) = -\sum_{n=0}^{\infty}(-1)^n \frac{1}{n!}\int_0^\infty d\tau_1 \ldots \int_0^\infty d\tau_n \\ \langle\Phi_0|T\left[\hat{H}_{pol}^{IB}(\tau_1)\ldots\hat{H}_{pol}^{IB}(\tau_{i+1})\ldots\hat{H}_{pol}^{IB}(\tau_n)\hat{c}_{\mathbf{p}}(\tau)\hat{c}_{\mathbf{p}}^{\dagger}(0)\right]|\Phi_0\rangle\ , \end{aligned} \tag{4.1}$$

with $|\Phi_0\rangle$ the phonon vacuum state without impurity and the operators are given in the interaction picture. The free Green's function for the impurity is

$$\begin{aligned} G^0(\mathbf{p},\tau) &= -\theta(\tau)\langle\Phi_0|\hat{c}_{\mathbf{p}}(\tau)\hat{c}^\dagger_{\mathbf{p}}(0)|\Phi_0\rangle \\ &= -\theta(\tau)e^{-(\epsilon_{\mathbf{p}}-\mu)\tau} , \end{aligned} \tag{4.2}$$

with $\epsilon_{\mathbf{p}} = \frac{p^2}{2m_I}$ the dispersion of the impurity with mass m_I and μ a free parameter. The free Green's function for an elementary excitation (phonon) is given by:

$$\begin{aligned} D(\mathbf{q},\tau) &= -\theta(\tau)\langle\Phi_0|\hat{b}_{\mathbf{q}}(\tau)\hat{b}^\dagger_{\mathbf{q}}(0)|\Phi_0\rangle \\ &= -\theta(\tau)e^{-\omega(\mathbf{q})\tau} , \end{aligned} \tag{4.3}$$

with $\omega(\mathbf{q})$ the dispersion of the elementary excitations. The first non-zero contribution $\mathcal{D}_1$ (this happens when $n = 2$) in Eq. (4.1) gives:

$$\begin{aligned} \mathcal{D}_1 &= -\int_0^\tau d\tau_2 \int_0^{\tau_2} d\tau_1 \langle\Phi_0|T\left[\hat{H}^{IB}_{pol}(\tau_1)\hat{H}^{IB}_{pol}(\tau_2)\hat{c}_{\mathbf{p}}(\tau)\hat{c}^\dagger_{\mathbf{p}}(0)\right]|\Phi_0\rangle \\ &= -\int_0^\tau d\tau_2 \int_0^{\tau_2} d\tau_1 \int \frac{d\mathbf{q}}{(2\pi)^3} V^2(\mathbf{q})\langle\Phi_0|T\left[\hat{c}^\dagger_{\mathbf{p}-\mathbf{q}}(\tau_1)\hat{c}_{\mathbf{p}}(\tau_1)\left(\hat{b}^\dagger_{\mathbf{q}}(\tau_1)+\hat{b}_{-\mathbf{q}}(\tau_1)\right)\right. \\ &\qquad \left.\hat{c}^\dagger_{\mathbf{p}}(\tau_2)\hat{c}_{\mathbf{p}-\mathbf{q}}(\tau_2)\left(\hat{b}^\dagger_{-\mathbf{q}}(\tau_2)+\hat{b}_{\mathbf{q}}(\tau_2)\right)\hat{c}_{\mathbf{p}}(\tau)\hat{c}^\dagger_{\mathbf{p}}(0)\right]|\Phi_0\rangle . \end{aligned} \tag{4.4}$$

The time-ordered product can be worked out with Wick's theorem:

$$\begin{aligned} \mathcal{D}_1 = -\int_0^\tau d\tau_2 \int_0^{\tau_2} d\tau_1 \int \frac{d\mathbf{q}}{(2\pi)^3} \; V^2(\mathbf{q})\; \hat{c}^\dagger_{\mathbf{p}-\mathbf{q}}(\tau_1)^{\textbf{❶}}\hat{c}_{\mathbf{p}}(\tau_1)\;{}^{\textbf{❸}}\hat{b}^\dagger_{\mathbf{q}}(\tau_1)^{\textbf{❷}}\hat{c}^\dagger_{\mathbf{p}}(\tau_2)^{\textbf{❹}} \\ \hat{c}_{\mathbf{p}-\mathbf{q}}(\tau_2)^{\textbf{❶}}\hat{b}_{\mathbf{q}}(\tau_2)^{\textbf{❷}}\hat{c}_{\mathbf{p}}(\tau)^{\textbf{❹}}\hat{c}^\dagger_{\mathbf{p}}(0)^{\textbf{❸}} . \end{aligned} \tag{4.5}$$

The contraction between the impurity operators is given by:

$$\hat{c}^\dagger_{\mathbf{p}}(\tau_1)^{\textbf{❶}}\hat{c}_{\mathbf{p}'}(\tau_2)^{\textbf{❶}} = -G^0(\mathbf{p},\tau_2-\tau_1)\delta(\mathbf{p}-\mathbf{p}') , \tag{4.6}$$

and the contraction for the elementary-excitations operators is

$$\hat{b}^\dagger_{\mathbf{q}}(\tau_1)^{\textbf{❶}}\hat{b}_{\mathbf{q}'}(\tau_2)^{\textbf{❶}} = -D(\mathbf{q},\tau_2-\tau_1)\delta(\mathbf{q}-\mathbf{q}') . \tag{4.7}$$

The contribution $\mathcal{D}_1$ can now be written in terms of free Green's functions:

$$\mathcal{D}_1 = -\int_0^\tau d\tau_2 \int_0^{\tau_2} d\tau_1 \int \frac{d\mathbf{q}}{(2\pi)^3} V^2(\mathbf{q})G^0(\mathbf{p},\tau_1)G^0(\mathbf{p}-\mathbf{q},\tau_2-\tau_1)D(\mathbf{q},\tau_2-\tau_1)G^0(\mathbf{p},\tau-\tau_2) . \tag{4.8}$$

The Feynman diagram that represents $\mathcal{D}_1$ is shown in Fig. 4.1. It is clear that all the higher-order diagrams have the same sign, since all non-zero contractions give positive contributions. The matrix elements in Eq. (4.1) are non-zero only if n is even. We define the diagram order $N = n/2$.

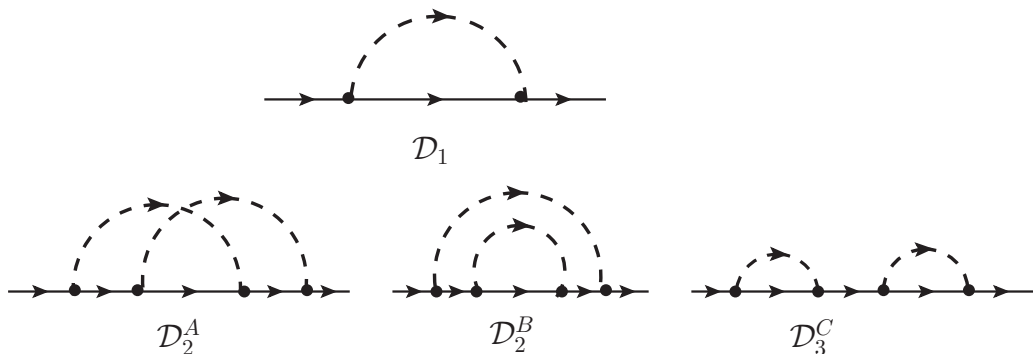

Figure 4.1 – The upper figure represents the first-order diagram $\mathcal{D}_1$. The lower figure shows the different topologies for the second-order diagrams. The diagrams $\mathcal{D}_1$, $\mathcal{D}_{2A}$ and $\mathcal{D}_{2B}$ are irreducible diagrams. A solid line represents a free-impurity propagator and a dashed line stands for an elementary excitation. The interaction vertices are denoted by dots. Imaginary time runs from left to right.

We show now how all topologies of order N can be created. First, one draws a BBL from 0 to τ with $2N$ vertices. This BBL consists out of $2N+1$ G^0-propagators. In the following step, we draw N lines above the BBL, going from one vertex to another vertex, in a way that each vertex has one incoming lines and two outgoing lines. In Fig. 4.1 the different topologies for order 2 are shown. One can check that for each order there exist $(2N-1)!!$ different topologies.

4.2 DiagMC for large polarons

In this section we give a short overview of the updates of the DiagMC method [32, 33] to evaluate diagrams for Bose polaron systems. To reduce the configuration space of diagrams, we prefer to consider only diagrams for the irreducible one-body self-energy $\Sigma(\mathbf{p},\tau)$. These diagrams contain no uncovered G^0-propagators. In the DiagMC simulation we sample $G^0\Sigma$-diagrams: these are irreducible Σ-diagrams with an (uncovered) G^0-propagator attached. We also use a cyclic representation of the diagrams.

To change the topology for a diagram at order N, we choose a nearest-neighbor pair of vertices and swap the two D-propagators ending in these vertices, see Fig. 4.2. The update is rejected if the new diagram is not a $G^0\Sigma$-diagram.

To change the times, we propose to change the time of a randomly chosen G^0-propagator and the above lying D-propagators. This update also changes the total time of a diagram.

To sample over all possible momenta, we include an update that changes the momentum of a randomly chosen D-propagator and the momentum of the piece of the BBL that lies below such that momentum conservation is restored.

To change the diagram order, we propose to add a D-propagator with time τ_D and momentum $\mathbf{q}$. We choose uniformly a time τ_1 on the BBL, which becomes the time of the left end of the new D-propagator, see Fig. 4.3. Then we need a probability density $W(\mathbf{q},\tau_D)$

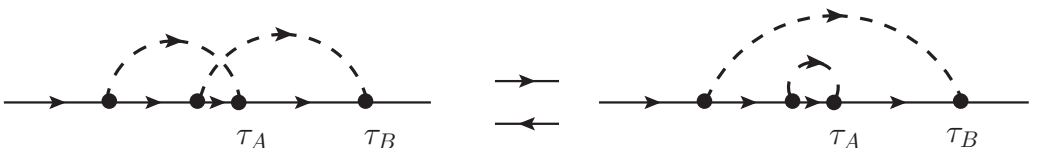

Figure 4.2 – Two irreducible $G^0\Sigma$-diagrams are shown. The ends of the two D-propagators at τ_A and τ_B are swapped.

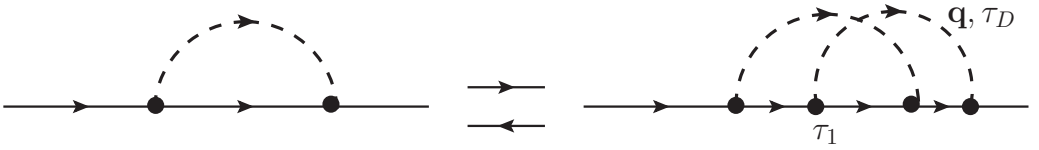

Figure 4.3 – Two irreducible $G^0\Sigma$-diagrams are shown. A D-propagator with momentum $\mathbf{q}$ and time τ_D is added to the left diagram at time τ_1 .

to propose a momentum and an imaginary time. A good choice for $W(\mathbf{q}, \tau_D)$ depends on the specific form of $V(\mathbf{q})$ and $\omega(\mathbf{q})$. For the acoustic and the BEC polaron, we use the following distribution for $W(\mathbf{q}, \tau_D)d\mathbf{q}d\tau_D$:

$$W(q, \theta, \phi, \tau_D)q^2 \sin(\theta)dqd\theta d\phi d\tau_D \propto q^2 \sin(\theta)V^2(q)e^{\omega(q)\tau_D}dqd\theta d\phi d\tau_D \ , \tag{4.9}$$

where we used spherical coordinates (q, θ, ϕ) for $\mathbf{q}$. We first sample a value for θ and ϕ. Then we sample a value for q and τ_D from $W'(q, \tau_D) \propto q^2V^2(q)e^{\omega(q)\tau_D}dqd\tau_D$. Since we cannot sample from $W'(q, \tau_D)$ directly, we tabulate the distribution first. The update is rejected if the new diagram is not a $G^0\Sigma$-diagram. In the delete-update we select at random a D-propagator to remove.

Collecting statistics

For each MC-step in the simulation we can collect statistics for the self-energy, which is stored in the histogram $\Sigma^{MC}(\tau_i)$ with τ_i the time of bin i. In the DiagMC simulation we keep the external momentum fixed. Since we are only interested in the Σ-part of a $G^0\Sigma$-diagram, the uncovered propagator can be seen as an extra weighting factor. If we sample a $G^0\Sigma$-diagram, where the Σ-part has time τ' and the uncovered G^0-propagator has time τ_0, we can update the histogram $\Sigma^{MC}(\tau_i)$ as follows:

$$\Sigma^{MC}(\tau_i') = \Sigma^{MC}(\tau_i') + \frac{1}{G^0(\mathbf{p}, \tau_0)} \ , \tag{4.10}$$

with τ_i' the time of the bin that contains the time τ'.

Since the diagrams have no alternating signs, we are able to obtain good statistics for very large diagram orders($\sim 10^4$). The normalization of the self-energy can be done in a similar way as was done for the Fermi polaron. In Eq. (2.84) we used the first order worm

diagram to normalize the collected statistics for the self-energy. Here, we can use the first order $G^0\Sigma$-diagram.

We will see in Sec. 4.3 that in some cases we need to reach very high diagram orders. In that case, it can take a long time for the simulation to go from the first order to the largest order and back. The reason is that the add/delete updates allow us to change only one order at a time. To overcome this issue, we first do a DiagMC run for low orders, for example from order 1 to order N_1 and we collect statistics for the one-body self-energy $\Sigma^{MC}_{1\to N_1}(\tau_i)$. The order N_1 is chosen such that the simulation can go fast from order 1 to N_1. From this run we know the number n_1 of times that a diagram at order N_1 is sampled. In a second step, we can do a new simulation from order N_1 to N_2 and collect statistics for the one-body self-energy $\Sigma^{MC}_{N_1\to N_2}(\tau_i)$. In this second run, we keep track of the number n_1' (n_2) that order N_1 (N_2) is sampled. In a third run we can collect statistics for $\Sigma^{MC}_{N_2\to N_3}(\tau_i)$ and count the number n_2' (n_3) that a diagram of order N_2 (N_3) is sampled. If needed, we can continue this way to reach the desired diagram orders. The final one-body self-energy $\Sigma^{MC}(\tau_i)$ that includes all diagram orders is now given by:

$$\Sigma^{MC}(\tau_i) = \Sigma^{MC}_{1\to N_1}(\tau_i) + \frac{n_1}{n_1'}\Sigma^{MC}_{N_1\to N_2}(\tau_i) + \frac{n_1}{n_1'}\frac{n_2}{n_2'}\Sigma^{MC}_{N_2\to N_3}(\tau_i) + \dots \,. \tag{4.11}$$

By using the first-order $G^0\Sigma$-diagram as the normalization diagram, we can obtain the normalized self-energy $\Sigma(\tau)$:

$$\Sigma(\tau) = \frac{\Sigma^{MC}(\tau_i)}{n_0\Delta_i}\int_0^\infty d\tau_2 \int_0^{\tau_2} d\tau_1 \int \frac{d\mathbf{q}}{(2\pi)^3} V(\mathbf{q})^2 G^0(\mathbf{p},\tau_1) G^0(\mathbf{p}-\mathbf{q},\tau_2-\tau_1) D(\mathbf{q},\tau_2-\tau_1)\,, \tag{4.12}$$

with n_0 the number of times that the first-order diagram was sampled. The time τ is contained in bin i with binsize Δ_i and time τ_i.

4.3 DiagMC study of the acoustic and the BEC polaron

This section contains the results of two large polaron systems: the BEC polaron and the acoustic polaron [34]. First, we show how to regularize the ultraviolet divergence for the BEC polaron. Second, we calculate the ground-state energies of these systems and perform a detailed comparison with a Feynman variational method. We also investigate whether some class of dominant diagrams can be found.

Diagrammatic Monte Carlo study of the acoustic and the BEC polaron

Jonas Vlietinck[1], Wim Casteels[3], Kris Van Houcke[1,2], Jacques Tempere[3,4], Jan Ryckebusch[1], and Jozef T. Devreese[3]

[1] *Department of Physics and Astronomy, Ghent University, Proeftuinstraat 86, 9000 Gent, Belgium*
[2] *Laboratoire de Physique Statistique, Ecole Normale Supérieure, UPMC, Université Paris Diderot, CNRS, 24 rue Lhomond, 75231 Paris Cedex 05, France*
[3] *TQC, Universiteit Antwerpen, Universiteitsplein 1, 2610 Wilrijk, Belgium*
[4] *Lyman Laboratory of Physics, Harvard University, Cambridge, Massachusetts 02138, USA*

Abstract

We consider two large polaron systems that are described by a Fröhlich type of Hamiltonian, namely the Bose-Einstein condensate (BEC) polaron in the continuum and the acoustic polaron in a solid. We present ground-state energies of these two systems calculated with the Diagrammatic Monte Carlo (DiagMC) method and with a Feynman all-coupling approach. The DiagMC method evaluates up to very high order a diagrammatic series for the polaron Green's function. The Feynman all-coupling approach is a variational method that has been used for a wide range of polaronic problems. For the acoustic and BEC polaron both methods provide remarkably similar non-renormalized ground-state energies that are obtained after introducing a finite momentum cutoff. For the renormalized ground-state energies of the BEC polaron, there are relatively large discrepancies between the DiagMC and the Feynman predictions. These differences can be attributed to the renormalization procedure for the contact interaction.

1 Introduction

By virtue of the Coulomb interaction the presence of a charge carrier in a charged lattice induces a polarization. This effect is well-known from the description of an electron or a hole in a polar or ionic semiconductor. The term polaron was coined by Landau in 1933 [1][1] to denote the quasiparticle comprised of a charged particle coupled to a surrounding polarized lattice. For lattice-deformation sizes of the order of the lattice parameter, one refers to the system as a small or Holstein polaron [2, 3]. For lattice-deformation sizes that are large compared to the lattice parameter, the lattice can be treated as a continuum. This system is

[1] The references of the citations in this text are located at the end of this chapter

known as a large polaron for which Fröhlich proposed the model Hamiltonian [4]

$$\hat{H}_{pol} = \sum_{\mathbf{k}} \frac{\hbar^2 \mathbf{k}^2}{2m} \hat{c}^\dagger_{\mathbf{k}} \hat{c}_{\mathbf{k}} + \sum_{\mathbf{k}} \hbar\omega(\mathbf{k}) \hat{b}^\dagger_{\mathbf{k}} \hat{b}_{\mathbf{k}} + \sum_{\mathbf{k},\mathbf{q}} V(\mathbf{q})\ \hat{c}^\dagger_{\mathbf{k}+\mathbf{q}} \hat{c}_{\mathbf{k}} \hat{b}^\dagger_{-\mathbf{q}} + \text{h.c.} \quad . \tag{1}$$

Here, the $\hat{c}^\dagger_{\mathbf{k}}$ ($\hat{c}_{\mathbf{k}}$) are the creation (annihilation) operators of the charge carriers with band mass m and momentum $\mathbf{k}$. The second term in the above Hamiltonian gives the energy of the phonons which carry the polarization. Thereby, the operator $\hat{b}^\dagger_{\mathbf{k}}$ ($\hat{b}_{\mathbf{k}}$) creates (annihilates) a phonon with wave vector $\mathbf{k}$ and energy $\hbar\omega(\mathbf{k})$. The last term in eq. (1) denotes the interaction between the charge carrier and the phonons. A plethora of physical phenomena can be described by the above Fröhlich type of Hamiltonian by varying the dispersion $\omega(\mathbf{k})$ and the interaction strength $V(\mathbf{q})$. Fröhlich considered the special situation of longitudinal optical (LO) phonons which are dispersionless $\omega(\mathbf{k}) = \omega_{LO}$. In the LO limit, the interaction amplitude $V(\mathbf{q})$ in Eq. (1) adopts the form

$$V_{LO}(\mathbf{q}) = -i \frac{\hbar\omega_{LO}}{q} \left(\frac{4\pi\alpha_{LO}}{\mathcal{V}} \right)^{1/2} \left(\frac{\hbar}{2m\omega_{LO}} \right)^{1/4} . \tag{2}$$

Here, $\mathcal{V}$ is the volume of the crystal and α_{LO} the dimensionless coupling parameter:

$$\alpha_{LO} = \frac{e^2}{\hbar} \sqrt{\frac{m}{2\hbar\omega_{LO}}} \left(\frac{1}{\varepsilon_\infty} - \frac{1}{\varepsilon_0} \right) , \tag{3}$$

with ε_∞ (ε_0) the electronic (static) dielectric constants of the crystal and e the charge of the electron. The Fröhlich polaron which is defined by the Eqs. (1)-(2) and the dispersion $\omega(\mathbf{k}) = \omega_{LO}$, has no analytical solution.

More generally, solutions to the Eq. (1) describe a quasiparticle interacting with a bath of non-interacting bosons with energies $\hbar\omega(\mathbf{k})$ through the mediation of the interaction $V(\mathbf{q})$. One example is the acoustic polaron which corresponds to the interaction of a charge carrier with acoustic phonons [5]. Another example is the BEC polaron consisting of an impurity atom interacting with the Bogoliubov excitations of an atomic Bose-Einstein condensate (BEC) [6, 7, 8]. Other examples are an electron on a helium film ("ripplopolaron") [9, 10, 11] and a charge carrier in a piezoelectric semiconductor ("piezopolaron") [12].

Due to the relative simplicity of the model Hamiltonian of eq. (1) it is an ideal testing ground for conducting comparative studies with various many-body techniques (see for example Refs. [13, 14] for an overview). The weak coupling regime (small α_{LO}) was described by Fröhlich with second-order perturbation theory [4] which is equivalent to the Lee-Low-Pines scheme using a canonical transformation [15]. For the strong coupling regime (large α_{LO}) Landau and Pekar developed a variational technique which predicts the formation of a bound state of the charge carrier in his self-induced potential [16, 17]. Feynman developed a superior all-coupling approach [18, 19] which captures all the coupling regimes.

A numerical solution of the Fröhlich Hamiltonian of Eq. (1) with the interaction of Eq. (2) has been proposed in Refs. [20, 21]. Thereby, a series expansion for the polaron Green's function was evaluated with the aid of a Diagrammatic Monte Carlo (DiagMC) method. The method is "exact" in the sense that the series expansion is convergent and sign-definite and therefore it can be stochastically evaluated with a controllable error. The polaron's energy is extracted from the asymptotic behavior of its Green's function.

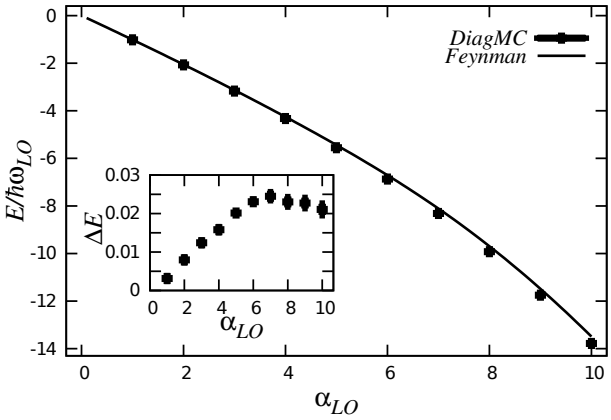

Figure 1 – Ground-state energies for the Fröhlich polaron are shown as a function of the coupling strength α_{LO} of Eq. (3). The inset shows the relative difference $\Delta E = \frac{E^{MC}-E^{F}}{E^{MC}}$, with E^{F} (E^{MC}) the computed energy from the Feynman (DiagMC) approach.

Polaron systems are ideal for comparative studies of many-body techniques. Examples of such studies for the Fermi polaron are reported in Refs. [22, 23, 24]. For the Fermi polaron, a comparison has been made between the DiagMC method and the variational technique which includes a limited number of particle-hole excitations. It was demonstrated that a variational one particle-hole calculation is already a good approximation, even for strong interactions between the impurity and the particles in the Fermi sea [23, 24]. Recently a comparative study of the neutron polaron has been conducted with quantum Monte Carlo and effective field theories [25]. For the ground-state energy of the Fröhlich polaron of Eqs. (1) and (2) it has been shown in Ref. [20] that Feynman's approach reproduces the DiagMC results to a remarkable accuracy. We have reproduced those numerical results. As can be appreciated from fig. 1 the deviations between the variational Feynman and DiagMC predictions for the ground-state energies of the Fröhlich polaron, are of the order of a few percent, even for the large coupling strengths. It is not clear, however, how accurate the Feynman technique is for polaron systems described by a Hamiltonian of the type of Eq. (1) with alternate dispersions $\omega(\mathbf{k})$ and interaction amplitudes $V(\mathbf{q})$. Indeed, Feynman's approach is based on a variational action functional that models the coupling to the phonons by a single phononic degree of freedom with a variationally determined mass and harmonic coupling to the electron. This is a rather natural choice for LO phonons, which are dispersionless. However, it seems intuitively less suitable in situations that the phonons' energies cover a finite range of values. Thornber [26] has argued that in those situations, Feynman's model is unlikely to yield accurate results for the system's dynamical properties, but that the system's ground-state energy can still be captured accurately. To our knowledge, this assertion has not yet been sufficiently confirmed. In order to remedy this situation, in this work we compare polaron ground-state energies calculated with the Feynman variational approach against DiagMC results. This will allow us to test the robustness of the Feynman approach. The two prototypical polaron problems considered in this work are the BEC polaron and the acoustic polaron. These problems have been selected because they highlight complementary aspects. The effect of broadening the range of phonon energies is captured by the acoustic

polaron. The BEC polaron problem allows one to additionally cover the issues related to renormalizing $V(\mathbf{q})$.

The structure of this manuscript is as follows. In section 2 the Hamiltonians for the BEC and acoustic polaron are introduced. In Sects. 3.1 and 3.2 the adopted many-body methods for obtaining the ground-state energies of those Hamiltonians are sketched. Results of the two techniques for the ground-state energies of the BEC and acoustic polaron are contained in Sec. 4.

2 Large polaron models

2.1 BEC polaron

The Hamiltonian of an impurity immersed in a bath of interacting bosons [8] is given by a sum of two terms $\hat{H} = \hat{H}_B + \hat{H}_I$ with,

$$\begin{aligned} \hat{H}_B &= \sum_{\mathbf{k}} \epsilon_{\mathbf{k}}\ \hat{a}^\dagger_{\mathbf{k}}\hat{a}_{\mathbf{k}} + \frac{1}{2\mathcal{V}} \sum_{\mathbf{k},\mathbf{k}',\mathbf{q}} V_{BB}(\mathbf{q})\ \hat{a}^\dagger_{\mathbf{k}'-\mathbf{q}}\hat{a}^\dagger_{\mathbf{k}+\mathbf{q}}\hat{a}_{\mathbf{k}}\hat{a}_{\mathbf{k}'}\ , \\ \hat{H}_I &= \sum_{\mathbf{k}} \frac{\hbar^2\mathbf{k}^2}{2m_I}\ \hat{c}^\dagger_{\mathbf{k}}\hat{c}_{\mathbf{k}} + \frac{1}{\mathcal{V}} \sum_{\mathbf{k},\mathbf{k}',\mathbf{q}} V_{IB}(\mathbf{q})\ \hat{c}^\dagger_{\mathbf{k}+\mathbf{q}}\hat{c}_{\mathbf{k}}\hat{a}^\dagger_{\mathbf{k}'-\mathbf{q}}\hat{a}_{\mathbf{k}'}\ . \end{aligned} \tag{4}$$

The operators $\hat{a}^\dagger_{\mathbf{k}}(\hat{a}_{\mathbf{k}})$ create (annihilate) bosons with momentum $\mathbf{k}$, mass m and energy $\epsilon_{\mathbf{k}} = \hbar^2\mathbf{k}^2/2m$. Further, $\mathcal{V}$ is the volume of the system. The operators $\hat{c}^\dagger_{\mathbf{k}}(\hat{c}_{\mathbf{k}})$ create (annihilate) the impurity with momentum $\mathbf{k}$ and mass m_I. The boson-boson and impurity-boson interactions in momentum space are $V_{BB}(\mathbf{q})$ and $V_{IB}(\mathbf{q})$. These potentials are replaced by the pseudopotentials g_{BB} and g_{IB}. These constants are chosen such that the two-body scattering properties in vacuum are correctly reproduced. The sum of all vacuum ladder diagrams, given by the T-matrix, represents all possible ways in which two particles can scatter in vacuum. For zero momentum and frequency the T-matrix is given by $T(0)$:

$$T(0) = g_{IB} - g_{IB} \sum_k \frac{2m_r}{\hbar^2 k^2} T(0)\ , \tag{5}$$

with $m_r = (1/m_I + 1/m)^{-1}$ the reduced mass. For low-energy collisions the first-order Born approximation can be applied to model the boson-boson and boson-impurity collisions. As a result, $g_{IB} = \frac{2\pi a_{IB}\hbar^2}{m_r}$, with a_{IB} the boson-impurity scattering length and $g_{BB} = \frac{4\pi a_{BB}\hbar^2}{m}$, with a_{BB} the boson-boson scattering length.

In the Bogoliubov approximation [27], the Hamiltonian $\hat{H}_B$ of eq. (4) is written in the diagonal form

$$\hat{H}_B \approx E_0 + \sum_{\mathbf{k}\neq 0} \hbar\omega(\mathbf{k})\hat{b}^\dagger_{\mathbf{k}}\hat{b}_{\mathbf{k}}\ , \tag{6}$$

where the operators $\hat{b}^\dagger_{\mathbf{k}}(\hat{b}_{\mathbf{k}})$ create (annihilate) Bogoliubov quasi-particles. The quasi-particle vacuum energy is

$$E_0 = \frac{\mathcal{V}}{2} n^2 g_{BB} + \frac{1}{2} \sum_{\mathbf{k}\neq 0} \left(\hbar\omega(\mathbf{k}) - \epsilon_{\mathbf{k}} - n_0 g_{BB} \right) , \tag{7}$$

with $n = N/\mathcal{V}$ the total density and $n_0 = N_0/\mathcal{V}$ the density of the condensed bosons. The average total particle number $N = \langle \hat{N} \rangle$ is fixed, with

$$\hat{N} = N_0 + \sum_{\mathbf{k}\neq 0} \hat{a}^\dagger_{\mathbf{k}} \hat{a}_{\mathbf{k}} , \tag{8}$$

and N_0 the number of bosons in the condensate. The collective Bogoliubov excitations obey the dispersion relation

$$\hbar\omega(\mathbf{k}) = \sqrt{(\epsilon_{\mathbf{k}} + n_0 g_{BB})^2 - (n_0 g_{BB})^2} . \tag{9}$$

At long wavelengths, the spectrum becomes $\omega(\mathbf{k}) = |\mathbf{k}|c$, which is characteristic of a sound wave with velocity $c = \sqrt{n_0 g_{BB}/m}$. The excitation spectrum is conveniently written in the form

$$\omega(\mathbf{k}) = kc\sqrt{1 + \frac{(k\xi)^2}{2}} , \tag{10}$$

with $k = |\mathbf{k}|$ and $\xi = 1/\sqrt{2mn_0 g_{BB}}$ the healing length of the Bose condensate.

Application of the Bogoliubov transformation to the impurity part $\hat{H}_I$ of eq. (4) gives [6, 7, 8]

$$\hat{H}_I \approx \sum_{\mathbf{k}} \frac{\hbar^2\mathbf{k}^2}{2m_I} \hat{c}^\dagger_{\mathbf{k}} \hat{c}_{\mathbf{k}} + n_0 g_{IB} + \sum_{\mathbf{q}\neq 0,\mathbf{k}} V_{BP}(\mathbf{q}) \, \hat{c}^\dagger_{\mathbf{k}+\mathbf{q}} \hat{c}_{\mathbf{k}} \left(\hat{b}^\dagger_{-\mathbf{q}} + \hat{b}_{\mathbf{q}} \right) , \tag{11}$$

in which we have defined

$$V_{BP}(\mathbf{q}) = \frac{g_{IB}}{\mathcal{V}} \sqrt{\frac{N_0 \epsilon_{\mathbf{q}}}{\omega(\mathbf{q})}} = \frac{g_{IB}\sqrt{N_0}}{\mathcal{V}} \left(\frac{(\xi q)^2}{(\xi q)^2 + 2} \right)^{1/4} . \tag{12}$$

For $g_{IB} = \frac{2\pi a_{IB}\hbar^2}{m_r}$ a dimensionless coupling constant α_{IB} can be defined [8]

$$\alpha_{IB} = \frac{a_{IB}^2}{a_{BB}\xi} . \tag{13}$$

The final expression for the Hamiltonian for the BEC polaron is given by

$$\hat{H}_{BP} = E_0 + n_0 g_{IB} + \sum_{\mathbf{k}} \frac{\hbar^2\mathbf{k}^2}{2m_I} \hat{c}^\dagger_{\mathbf{k}} \hat{c}_{\mathbf{k}} + \sum_{\mathbf{k}\neq 0} \hbar\omega(\mathbf{k}) \hat{b}^\dagger_{\mathbf{k}} \hat{b}_{\mathbf{k}} + \sum_{\mathbf{q}\neq 0,\mathbf{k}} V_{BP}(\mathbf{q}) \, \hat{c}^\dagger_{\mathbf{k}+\mathbf{q}} \hat{c}_{\mathbf{k}} \left(\hat{b}^\dagger_{-\mathbf{q}} + \hat{b}_{\mathbf{q}} \right) . \tag{14}$$

Obviously, the $\hat{H}_{BP}$ has the format of a Fröhlich-type of Hamiltonian defined in Eq. (1). When presenting numerical results for the BEC polaron, lengths will be expressed in units of ξ, energies in units of $\frac{\hbar^2}{m\xi^2}$ and phonon wave vectors in units of $1/\xi$. In this way, all quoted variables are dimensionless. In the numerical calculations, we consider an ^{6}Li impurity in a Na condensate for which $m_I/m_B = 0.263158$ [8].

2.2 Acoustic polaron

In a crystal with two or more atoms per primitive cell, the dispersion relation $\omega(\mathbf{k})$ for the phonons develops acoustic as well as optical branches. The acoustic polaron comprises a charge carrier interacting with the longitudinal acoustic phonons and can be described by the Fröhlich type of Hamiltonian of Eq. (1) with the dispersion $\omega(\mathbf{k}) = sk$, with s the sound velocity [5]. For the acoustic polaron, the interaction $V_{AC}(\mathbf{q})$ in the Fröhlich Hamilonian adopts the form [5]:

$$V_{AC}(\mathbf{q}) = \left(\frac{4\pi\alpha_{AC}}{\mathcal{V}}\right)^{1/2} \frac{\hbar^2}{m}\sqrt{q}\ , \tag{15}$$

with $\mathcal{V}$ the volume of the crystal and α_{AC} a dimensionless coupling parameter. When discussing results concerning the acoustic polaron, lengths will be expressed in units of $\hbar/(ms)$, energies in units of ms^2 and phonon wave vectors in units of $ms/\hbar$. The summations over the phonon momenta $|\ \mathbf{k}\ |$ have a natural cut-off at the boundary k_0 of the first Brillouin zone. At strong coupling, the Feynman approach to the acoustic polaron predicts the emergence of a self-induced binding potential for the impurity ("self-trapped state"). For a system with both Fröhlich and acoustic phonons, the Feynman approach predicts that the dominant mechanism for this transition is the interaction with the acoustic phonons [28]. Only considering the acoustic phonons results in a transition of the first order for $k_0 > 18$ and a critical point at $k_0 \approx 18$ and $\alpha_{AC} \approx 0.151$ [5]. This transition was also predicted by the path integral Monte Carlo method [29].

3 Numerical methods

3.1 Feynman variational path integral

The Feynman approach is based on the Jensen-Feynman inequality for the free energy $\mathcal{F}$ of a system with action $\mathcal{S}$ [19]:

$$\mathcal{F} \leq \mathcal{F}_0 + \frac{1}{\hbar\beta}\left\langle \mathcal{S} - \mathcal{S}_0 \right\rangle_{\mathcal{S}_0}\ . \tag{16}$$

Here, $\mathcal{F}_0$ is the free energy of a trial system with action $\mathcal{S}_0$, $\langle ... \rangle_{\mathcal{S}_0}$ denotes the expectation value with respect to the trial system and $\beta = (k_B T)^{-1}$ is the inverse temperature. Feynman proposed a variational trial system of a charge carrier harmonically coupled with spring frequency W to a fictitious particle with mass M. For $T = 0$ the Jensen-Feynman inequality of eq. (16) applied to this system produces an upper bound E_p^F for the polaronic ground-state energy [18, 19]:

$$E_p \leq \frac{3\hbar\Omega}{4}\frac{\left(\sqrt{(1+M/m_I)}-1\right)^2}{1+M/m_I} + \sum_{\mathbf{k}}\frac{|V_{\mathbf{k}}|^2}{\hbar}\int_0^\infty du\mathcal{D}\left(\mathbf{k},u\right)\mathcal{M}\left(\mathbf{k},u\right)\ , \tag{17}$$

with $\Omega = W\sqrt{1+M/m}$. The function $\mathcal{D}\left(\mathbf{k},u\right)$ is the phonon Green's function in momentum-imaginary-time representation $(\mathbf{k},\tau)$

$$\mathcal{D}\left(\mathbf{k},\tau\right) = -\theta\left(\tau\right)\exp\left[-\omega(\mathbf{k})\tau\right]\ , \tag{18}$$

where $\theta(\tau)$ is the Heaviside function. The memory function $\mathcal{M}(\mathbf{k}, u)$ is:

$$\mathcal{M}(\mathbf{k}, u) = \exp\left[-\frac{\hbar k^2}{2(m_I + M)}\left(u + \frac{M}{m_I}\frac{1 - \exp[-\Omega u]}{\Omega}\right)\right] . \tag{19}$$

The u-integral in eq. (17) is of the following form:

$$\int_0^\infty du \exp\left[-au + be^{-u}\right] = -(-b)^{-a}\,\Gamma(a, -b, 0) , \tag{20}$$

with $\Gamma(a, z_0, z_1) = \int_{z_0}^{z_1} t^{a-1}e^{-t}dt$ the generalized incomplete gamma function. The parameters M and Ω are used to minimize the upper bound for the ground state energy of eq. (17). This approach captures the different coupling regimes.

3.2 One-body propagator and DiagMC

The Green's function of the polaron in the $(\mathbf{k}, \tau)$ representation is defined as:

$$G(\mathbf{k}, \tau) = -\theta(\tau)\langle \mathrm{vac}|\hat{c}_{\mathbf{k}}(\tau)\hat{c}^\dagger_{\mathbf{k}}(0)|\mathrm{vac}\rangle, \tag{21}$$

with

$$\hat{c}_{\mathbf{k}}(\tau) = e^{\hat{H}\tau}\hat{c}_{\mathbf{k}}e^{-\hat{H}\tau}, \tag{22}$$

the annihilation operator in the Heisenberg representation and $|\mathrm{vac}\rangle$ the vacuum state. The BEC polaron Hamiltonian $\hat{H}_{BP}$ of Eq. (14) contains a vacuum energy $E_0 + n_0 g_{IB}$ which we choose as the zero of the energy scale. Accordingly, $\hat{H}_{BP}|\mathrm{vac}\rangle = 0$. We define $\{|\nu(\mathbf{k})\rangle\}$ as those eigenfunctions of $\hat{H}_{BP}$ with energy eigenvalue $E_\nu(\mathbf{k})$ and with one impurity with momentum $\mathbf{k}$. Inserting a complete set of eigenstates in Eq. (21) gives

$$G(\mathbf{k}, \tau) = -\theta(\tau)\sum_\nu |\langle \nu(\mathbf{k})|\hat{c}^\dagger_{\mathbf{k}}|\mathrm{vac}\rangle|^2 e^{-E_\nu(\mathbf{k})\tau} . \tag{23}$$

Under the conditions that the polaron is a stable quasi-particle in the ground state (in the sense that it appears as a δ-function peak in the spectral function), one can extract its energy $E_p(\mathbf{k})$ and Z-factor Z_0 by studying the long imaginary time behavior of the polaron's Green's function:

$$G(\mathbf{k}, \tau, \mu) \equiv G(\mathbf{k}, \tau)\; e^{\mu\tau} \overset{\tau\to+\infty}{\sim} -Z_0(\mathbf{k})\; e^{-(E_p(\mathbf{k})-\mu)\tau}, \tag{24}$$

where

$$Z_0(\mathbf{k}) = |\langle \Psi(\mathbf{k})|\hat{c}^\dagger_{\mathbf{k}}|\mathrm{vac}\rangle|^2, \tag{25}$$

with $\Psi(\mathbf{k})$ the fully interacting ground state. The unphysical parameter μ is introduced to control the exponential tail of G in imaginary time, and to ensure that it is always descending. The particular choice of μ has no impact on the final results. The asymptotic behavior of eq. (24) is associated with a pole singularity for the Green's function in imaginary-frequency representation. For $(E_p(\mathbf{k}) - \mu) > 0$ one has

$$G(\mathbf{k}, \omega, \mu) = \int_0^{+\infty} d\tau\; e^{i\omega\tau}\; G(\mathbf{k}, \tau, \mu) = \frac{Z_0(\mathbf{k})}{i\omega + \mu - E_p(\mathbf{k})} + \text{ regular part} . \tag{26}$$

The one-body self-energy $\Sigma(\mathbf{k},\omega,\mu)$ is related to the Green's function by means of the Dyson equation

$$G(\mathbf{k},\omega,\mu) = \frac{1}{\frac{1}{G^0(\mathbf{k},\omega,\mu)} - \Sigma(\mathbf{k},\omega,\mu)} \,, \tag{27}$$

with $G^0(\mathbf{k},\omega,\mu)$ the free impurity Green's function (see Eq. (29)). Since the Eqs. (26) and (27) possess the same pole structure, the following expression for the polaronic ground-state energy $E_p = E_p(\mathbf{k}=\mathbf{0})$ can be obtained [20]:

$$\begin{aligned} E_p &= \Sigma(\mathbf{k}=0,\omega=0,\mu=E_p) \\ &= \int_0^\infty d\tau\ \Sigma(\tau,\mu)\ e^{(E_p-\mu)\tau} \,, \end{aligned} \tag{28}$$

with $\Sigma(\tau,\mu) \equiv \Sigma(\mathbf{0},\tau,\mu)$. Calculating the Green's function boils down to summing a series of Feynman diagrams over all topologies and orders, thereby integrating over all internal variables (like momentum and imaginary time). It is shown in [20] that DiagMC is very suitable to accurately compute the Green's function through a series expansion.

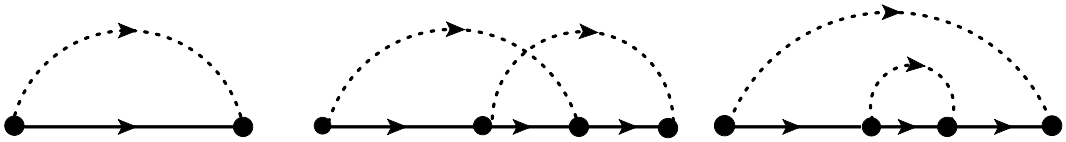

Figure 2 – Irreducible diagrams for the polaron's self-energy $\Sigma(\mathbf{k},\tau,\mu)$. Imaginary time runs from left to right. A solid line represents a free-impurity propagator and a dashed line stands for an elementary excitation. The interaction vertices are denoted by dots.

In fig. 2 some Feynman diagrams for Σ are shown. The algebraic expression for these diagrams is given in terms of free propagators and interaction vertices:

(i) The free-impurity propagator in imaginary time is determined by

$$G^0(\mathbf{k},\tau,\mu) = -\theta(\tau) e^{-(\epsilon_k-\mu)\tau} \,. \tag{29}$$

(ii) The propagator for an elementary phonon excitation, either of the Bogoliubov type for the BEC polaron, or acoustic phonons for the acoustic polaron is defined in Eq. (18).

(iii) A vertex factor $V(\mathbf{q})$ whenever an elementary excitation carrying momentum $\mathbf{q}$ is created or annihilated.

We consider irreducible diagrams and evaluate a large number of diagrams D in order to numerically compute the $\Sigma(\mathbf{k},\tau,\mu)$

$$\begin{aligned} \Sigma(\mathbf{k},\tau,\mu) = \sum_{n=1}^{\infty} \sum_{\xi_n} \sum_{\mathbf{q_i}=\mathbf{1},\ldots,\mathbf{n}} \int\int\int_{0<\tau_1<\ldots<\tau_i<\ldots<\tau_{2n-2}<\tau} d\tau_1 \ldots d\tau_i \ldots d\tau_{2n-2} \\ \times D(\xi_n,\mathbf{k},\tau,\mu,\tau_1,\ldots,\tau_i,\ldots,\tau_{2n-2},\mathbf{q_1},\ldots,\mathbf{q_i},\ldots,\mathbf{q_n}) \,, \end{aligned} \tag{30}$$

where ξ_n represents the topology, n the diagram order, $\mathbf{q_i}$ are the independent internal momenta and τ_i is the internal imaginary times. We define the diagram order by counting

the number of elementary excitations (the number of dashed propagators in Fig. (2)). The DiagMC technique allows one to sample over all topologies, all orders and all values of the internal variables, and thus to determine Σ.

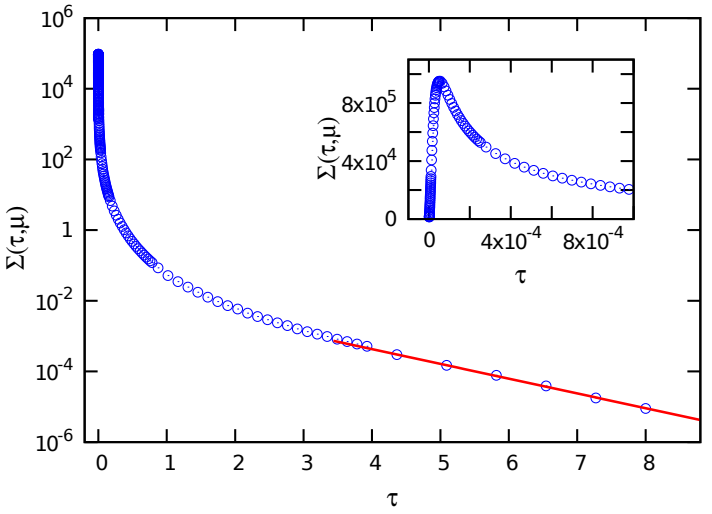

Figure 3 – The one-body self-energy $\Sigma(\tau, \mu)$ for $\mu = -790$ for the BEC polaron plotted as a function of imaginary time τ. Results are obtained for $\alpha_{IB} = 5$ and $q_c = 200$ and exclude the first-order contribution to $\Sigma(\tau, \mu)$ which can be easily computed analytically. The inset shows $\Sigma(\tau, \mu)$ for small imaginary times.

4 Results and discussion

4.1 BEC polaron

For the Fröhlich polaron for which the ground-state energies are displayed in Fig. 1, the one-body self-energy $\Sigma(\tau, \mu)$ can be computed by means of the procedure sketched in Sec. 3.2. For the BEC polaron, on the other hand, one encounters ultraviolet divergences when evaluating $\Sigma(\tau, \mu)$ and its energy cannot be extracted. Renormalization/regularization of the impurity-boson pseudopotential is required to obtain physically relevant results for the energies. As a first step in the renormalization procedure, we introduce a momentum cutoff q_c upon replacing the momentum summations in Eq. (14) by integrals:

$$\sum_{\mathbf{k}} \to \frac{\mathcal{V}}{(2\pi)^3} \int_{|\mathbf{k}|<q_c} d\mathbf{k} \, . \tag{31}$$

This allows us to calculate $\Sigma(\tau, \mu)$ and the accompanying ground-state energy E_p^{MC}. From now on we will make the distinction between the polaron energy calculated by DiagMC (E_p^{MC}) and calculated by the Feynman approach (E_p^F). Obviously, $E_p^{MC,F}$ depends on q_c and in order to stress this dependence we use the notation $E_p^{MC,F}(q_c)$. In fig. 3 we show an

example of the time dependence of the one-body self-energy $\Sigma(\tau, \mu)$ for the BEC polaron for $q_c = 200$. As can be noticed, after introducing a momentum cutoff q_c, the τ dependence is well behaved and the asymptotic regime of $\Sigma(\tau, \mu)$ can be identified. The $\sum_{n=0}^{\infty}$ in eq. (30) implies a summation over an infinite number of diagram orders. In practice, we set a cutoff $N_{\max}$ for n in evaluating $\Sigma(\tau, \mu)$. For each $N_{\max}$ we can find a corresponding imaginary time $\tau_{\max}$ for which we observe that $\Sigma_{n=0}^{N_{\max}} \Sigma^{(n)}(\tau < \tau_{\max}, \mu) = \Sigma_{n=0}^{\infty} \Sigma^{(n)}(\tau < \tau_{\max}, \mu)$ within the numerical noise. Hereby, $\Sigma^{(n)}(\tau, \mu)$ is the contribution from the n-th order diagrams to the self-energy. Upon increasing $N_{\max}$ the value of $\tau_{\max}$ increases accordingly. An optimal $N_{\max}$ is reached when we can find a $\tau_{\max}$ in the asymtotic regime that allows us to fit the tail of $\Sigma(\tau, \mu)$. In this way we make an extrapolation for $\tau \to \infty$ which determines the value $N_{\max}$. Typical values of $N_{\max}$ are of the order 10^4 for large values of α_{IB}. With the aid of the Eq. (28), $E_p^{MC}(q_c)$ can be extracted from the computed $\Sigma(\tau, \mu)$. The error on $E_p^{MC}(q_c)$ contains a statistical error and a systematic error stemming from the fitting procedure. As can be appreciated from fig. 3, the grid in imaginary time has to be chosen carefully, since the short-time behavior of $\Sigma(\tau, \mu)$ is strongly peaked. The $\Sigma(p, \tau, \mu)$ for these short times delivers a large contribution to the energy.

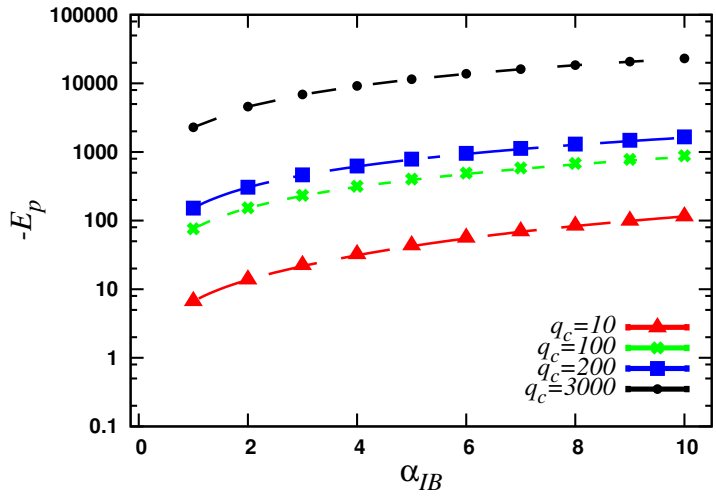

Figure 4 – The non-renormalized BEC-polaron energy E_p as a function of the coupling strength α_{IB} as computed with the DiagMC (symbols) and with the Feynman (lines) approaches. Results are shown for four values of the cutoff momentum.

In fig. 4, results for the non-renormalized energies $E_p^F(q_c)$ and $E_p^{\mathrm{MC}}(q_c)$ are presented as a function of the dimensionless coupling parameter α_{IB} defined in eq. (13). The α_{IB} and q_c dependence of the DiagMC energies is remarkably similar to those of the Feynman energies. We observe that $E_p^{\mathrm{MC}}(q_c)$ lies a few percent below $E_p^F(q_c)$ for all combinations of α_{IB} and q_c considered.

In Ref. [8] a renormalization procedure to eliminate the q_c dependence of the computed polaron energy is outlined. When determinig the T-matrix of Eq. (5) up to second order, the following relation between the scattering length a_{IB} and the coupling strength g_{IB} is

obtained:

$$\frac{2\pi a_{IB}\hbar^2}{m_r} = g_{IB} - \frac{g_{IB}^2}{(2\pi)^3}\int_{|\mathbf{q}|<q_c} d\mathbf{q}\frac{2m_r}{\hbar^2 q^2}\ . \tag{32}$$

Using this expression, the $n_0 g_{IB}$ term in eq. (14) can be replaced by :

$$n_0 g_{IB} \to \frac{2\pi a_{IB} n_0 \hbar^2}{m_r} + E_{\rm ren}(q_c)\ , \tag{33}$$

whereby we have defined $E_{\rm ren}(q_c)$:

$$E_{\rm ren}(q_c) = \frac{n_0 g_{IB}^2}{(2\pi)^3}\int_{|\mathbf{q}|<q_c} d\mathbf{q}\frac{2m_r}{\hbar^2 q^2}\ . \tag{34}$$

This renormalization procedure was developed in the context of the Feynman approach [8]. The same procedure can also be applied in the DiagMC framework. In both frameworks, the renormalized polaron ground-state energy can be found by evaluating the sum

$$E_p^{MC,F} = E_p^{MC,F}(q_c \to \infty) + E_{\rm ren}(q_c \to \infty)\ . \tag{35}$$

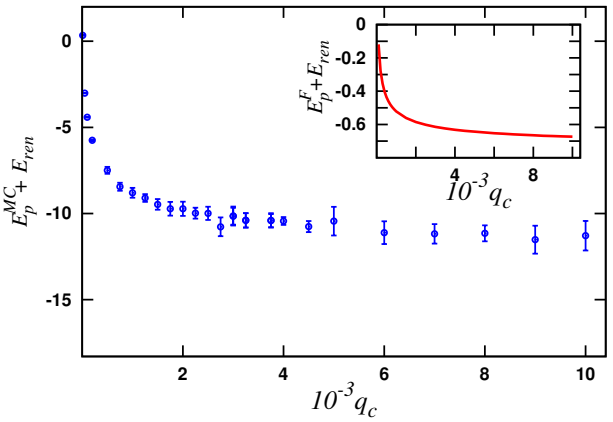

Figure 5 – The renormalized BEC-polaron energies $[E_p^{MC}(q_c) + E_{\rm ren}(q_c)]$ at $\alpha_{IB} = 3$ are given as a function of the momentum cutoff q_c. The inset figure shows $[E_p^{F}(q_c) + E_{\rm ren}(q_c)]$ as a function of q_c.

In order to illustrate the convergence of the Eq. (35) in both approaches, in fig. 5 the energies $[E_p^{MC}(q_c) + E_{\rm ren}(q_c)]$ and $[E_p^{F}(q_c) + E_{\rm ren}(q_c)]$ are plotted as a function of q_c for a representative value $\alpha_{IB} = 3$ of the coupling strength. We notice that the DiagMC and the Feynman approach display an analogous q_c dependence. Convergence is reached for $q_c \gtrsim 3000$. Fig. 6 shows that the Feynman path-integral predictions for the BEC-polaron ground-state energies overshoot the DiagMC ones. The relative difference between the two predictions increases with growing values of q_c. The very good agreement between the two methods that was found in fig. 4 for the non-renormalized energies, is no longer observed for the renormalized energies. Indeed, the latter are obtained with eq. (35), which amounts to substracting two numbers of almost equal magnitude. Accordingly, the final result for the renormalized BEC-polaron ground-state energy is highly sensitive to the adopted many-body

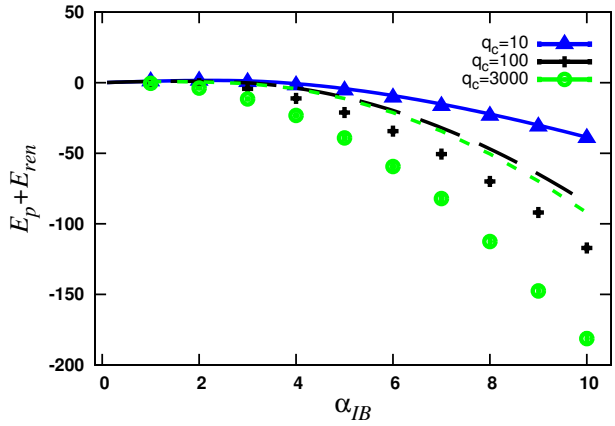

Figure 6 – The renormalized BEC-polaron energies $[E_p(q_c) + E_{\rm ren}(q_c)]$ as a function of α_{IB} for different values of the momentum cutoff q_c. Lines are the Feynman path-integral and symbols are the DiagMC results.

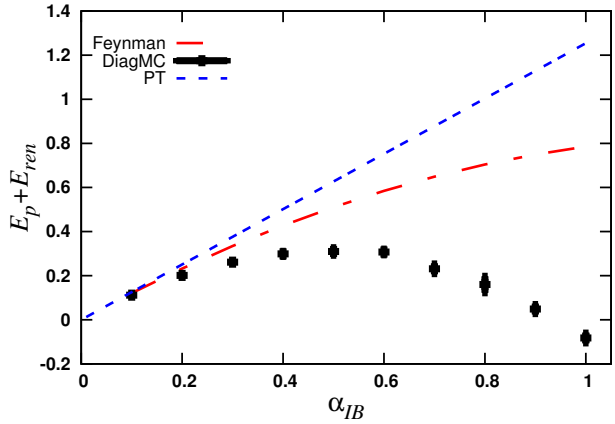

Figure 7 – The renormalized BEC-polaron energies $[E_p(q_c) + E_{\rm ren}(q_c)]$ at small values of α_{IB} at $q_c = 2000$. The dot-dashed line is the Feynman path-integral result, symbols represent the DiagMC results, while the short dashed line is the prediction from second-order perturbation theory (PT).

technique and renormalization procedure. Fig. 7 illustrates that for small α_{IB} both methods reproduce the result from second-order perturbation theory.

The DiagMC method samples diagrams according to their weight and it can be recorded how many times a specific diagram is sampled. In this way, one can identify those diagrams with the largest weight in the self-energy $\Sigma(\tau, \mu)$. At fixed diagram order, we have observed that the number of first-order subdiagrams–the definition of which is explained in the caption of fig. 8–plays a crucial role in the weight of the diagram. Our studies indicate that for $q_c > 50$ the most important diagram is the one with the highest number of first-order subdiagrams. We have considered many combinations of α_{IB} and q_c and could draw this conclusions in

all those situations. The dominance of this diagram becomes more explicit with increasing values of q_c.

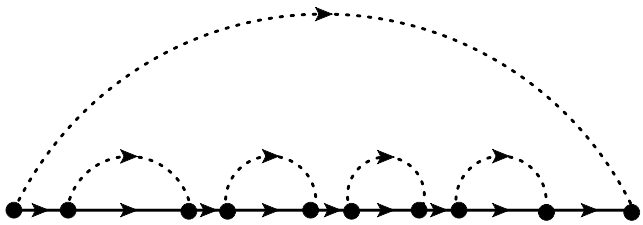

Figure 8 – A diagram of order five for the one-body self-energy. Line conventions as in Fig. 2. Imaginary time runs from left to right. A first-order subdiagram occurs whenever a first-order diagram drops out from the full diagram by cutting the solid line at two selected times. For example, the considered diagram contains four first-order subdiagrams.

4.2 Acoustic polaron

We now discuss the numerical results for the ground-state energy of the acoustic polaron introduced in Sec. 2.2. In Figs. 9 and 10 we show a selection of the predictions E_p^F from the Feynman upper-bound method of Eq. (17) together with the DiagMC results E_p^{MC} which are computed with the aid of Eq. (28). For the cut-off $k_0 = 10$ and $k_0 = 50$ an excellent agreement between E_p^F and E_p^{MC} is found. From the relative difference $\Delta E = \frac{E_p^{MC} - E_p^F}{E_p^{MC}}$, a value α_{AC} can be found where ΔE is largest in the considered region of α_{AC}. For $k_0 = 10$ we find $\alpha_{AC}^{k_0=10} = 0.28 \pm 0.04$ and for $k_0 = 50$, $\alpha_{AC}^{k_0=50} = 0.052 \pm 0.001$. For $\alpha < \alpha_c$, ΔE increases with α_{AC} and for $\alpha > \alpha_c$ ΔE decreases with increasing α_{AC}. We remark that $\alpha_c^{k_0=10}$ and $\alpha_c^{k_0=50}$ coincides with the coupling strength for the transition [28] as computed with the Feynman approach.

From a detailed analysis of the DiagMC results for $k_0 = 50$ we find that the class of diagrams of the type sketched in fig. 8 plays a dominant role for $\alpha_{AC} < \alpha_c$. For $\alpha_{AC} > \alpha_c$ we observe a dramatic change in the importance of those diagrams, and we can no longer identify a class of a diagrams that provides the major contribution to the self-energy $\Sigma(\tau, \mu)$.

The knowledge of a certain class of dominant diagrams can be exploited to develop approximate schemes. Indeed, one can set up a self-consistent scheme thereby summing over an important class of diagrams, including the observed dominant ones. In practice, the procedure can be realized by introducing bold (or dressed) propagators

$$\Sigma^{(i-1)}(\mathbf{p}, \omega, \mu) = \int d\omega' \int \frac{d\mathbf{q}}{(2\pi)^3} G^{(i-1)}(\mathbf{p} - \mathbf{q}, \omega - \omega', \mu) \mathcal{D}(\mathbf{q}, \omega')$$

$$G^{(i)}(\mathbf{p}, \omega, \mu) = \frac{1}{{G^0}^{-1}(\mathbf{p}, \omega, \mu) - \Sigma^{(i-1)}(\mathbf{p}, \omega, \mu)} \quad ,$$

with ω and ω' the imaginary frequencies. The self-energy $\Sigma^{(i-1)}$ and the dressed Green's function $G^{(i)}(\mathbf{p}, \omega, \mu)$ are calculated for subsequent values of i, starting from $i = 1$, until

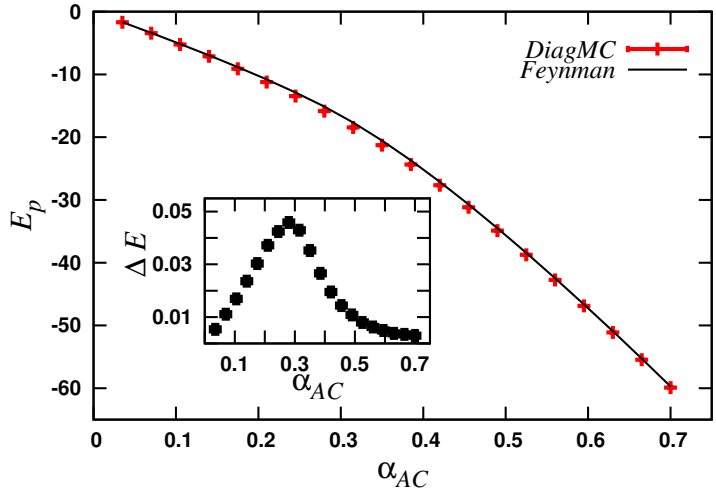

Figure 9 – Non-renormalized ground-state energies E_p^F and E_p^{MC} for the acoustic polaron as a function of α_{AC} for $k_0 = 10$. The inset shows $\Delta E = \frac{E_p^{MC} - E_p^F}{E_p^{MC}}$ as a function of α_{AC}.

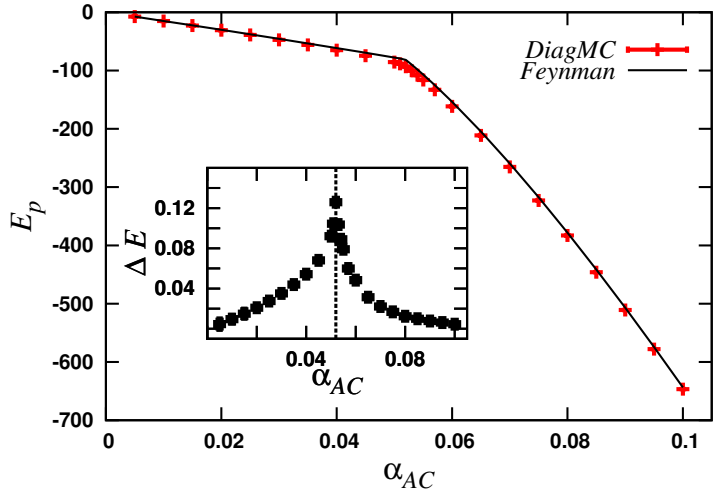

Figure 10 – As in Fig. 9 but for $k_0 = 50$. The vertical dashed line denotes the coupling strength $\alpha_{AC} = 0.052$ corresponding with the transition as computed in Ref. [5].

$G^{(i)}(\mathbf{p}, \omega, \mu)$ is converged. In this way $\Sigma^{(i)}(\mathbf{p}, \omega, \mu)$ will contain all diagrams for which the lines of the phonon propagators do not cross.

5 Conclusions

We have studied the ground-state energies of the BEC polaron and the acoustic polaron, two large polaron systems that can be described by a Fröhlich type of Hamiltonian. When calculating energies for the BEC polaron with the DiagMC and the Feynman variational technique, we encounter similar ultraviolet divergences. For the acoustic polaron, the ultraviolet regularization is achieved by a hard momentum cutoff which is naturally set at the edge of the first Brillouin zone. In this case, the DiagMC and Feynman predictions for the ground-state energies agree within a few percent. The largest deviation between the predictions of both methods, was found at a coupling strength that marks the transition between a quasifree and a self-trapped state. For the BEC polaron, a more involving two-step renormalization procedure is required. The first step is the introduction of a hard momentum cutoff. In line with the results for the acoustic polaron, the DiagMC and Feynman non-renormalized ground-state energies of the BEC polaron which are produced in this step are remarkably similar. Therefore, one can infer that the Feynman variational method reproduces the "exact" DiagMC non-renormalized polaron ground-state energies at a finite momentum cutoff.

In order to obtain the physical, or renormalized, BEC-polaron energies from the non-renormalized ones, an additional procedure is required. Thereby, the contact interaction is renormalized with the aid of the lowest-order correction obtained from the Lippmann-Schwinger equation (34). Despite the fact that the absolute difference between the Feynman and DiagMC BEC-polaron energies remains unaffected by this procedure, the final result for the physical energies displays a large relative difference.

Acknowledgments

This work is supported by the Flemish Research Foundation (FWO Vlaanderen) through project numbers G.0119.12N and G.0115.12N. Discussions with S.N. Klimin and L.A. Pena-Ardila are gratefully acknowledged. The computational resources (Stevin Supercomputer Infrastructure) and services used in this work were provided by Ghent University, the Hercules Foundation, and the Flemish Government.

References

[1] L. D. Landau, Phys. Z. Sowjetunion **3**, 664 (1933)

[2] G. Wellein, H. Röder, and H. Fehske, Phys. Rev. B **53**, 9666 (1996)

[3] D. J. J. Marchand and M. Berciu, Phys. Rev. B **88**, 060301 (2013)

[4] H. Fröhlich, Adv. Phys. **3**, 325 (1954)

[5] F. M. Peeters and J. T. Devreese, Phys. Rev. B **32**, 3515 (1985)

[6] F. M. Cucchietti and E. Timmermans, Phys. Rev. Lett. **96**, 210401 (2006)

[7] K. Sacha and E. Timmermans, Phys. Rev. A **73**, 063604 (2006)

[8] J. Tempere, W. Casteels, M. K. Oberthaler, S. Knoop, E. Timmermans, and J. T. Devreese, Phys. Rev. B **80**, 184504 (2009)

[9] V. Shikin and Y. Monarkha, J. Low Temp. Phys. **16**, 193 (1974)

[10] S. A. Jackson and P. M. Platzman, Phys. Rev. B **24**, 499 (1981)

[11] G. E. Marques and N. Studart, Phys. Rev. B **39**, 4133 (1989)

[12] G. D. Mahan and J. J. Hopfield, Phys. Rev. Lett. **12**, 241 (1964)

[13] J. T. Devreese and A. S. Alexandrov, *Advances In Polaron Physics*, Vol. 159 (Springer-Verlag Berlin, 2010)

[14] J. T. Devreese, ArXiv: 1012.4576(2010)

[15] T. D. Lee, F. E. Low, and D. Pines, Phys. Rev. **90**, 297 (1953)

[16] L. D. Landau and S. I. Pekar, Zh. Eksp. Teor. Fiz. **16**, 341 (1946)

[17] S. I. Pekar , Berlin, Akademie Verslag (1951)

[18] R. P. Feynman, Phys. Rev. **97**, 660 (1955)

[19] R. P. Feynman, *Statistical mechanics: A set of lectures* (Addison-Wesley Publ. Co., Reading, MA, 1990)

[20] N. V. Prokof'ev and B. V. Svistunov, Phys. Rev. Lett. **81**, 2514 (1998)

[21] A. S. Mishchenko, N. V. Prokof'ev, A. Sakamoto, and B. V. Svistunov, Phys. Rev. B **62**, 6317 (2000)

[22] P. Massignan, M. Zaccanti, and G. M. Bruun, Rep. Prog. Phys. **77**, 034401 (2014)

[23] J. Vlietinck, J. Ryckebusch, and K. Van Houcke, Phys. Rev. B **87**, 115133 (2013)

[24] J. Vlietinck, J. Ryckebusch, and K. Van Houcke, Phys. Rev. B **89**, 085119 (2014)

[25] M. M. Forbes, A. Gezerlis, K. Hebeler, T. Lesinski, and A. Schwenk, Phys. Rev. C **89**, 041301 (2014)

[26] K. K. Thornber, Phys. Rev. B **9**, 3489 (1974)

[27] L. Pitaevskii and S. Stringari, *Bose-Einstein Condensation*, 1st ed. (Oxford University Press, 2003)

[28] A. Sumi and Y. Toyozawa, J. Phys. Soc. Japan **35**, 137 (1973)

[29] R. Fantoni, Phys. Rev. B **86**, 144304 (2012)

CHAPTER 5

Summary

In recent years, the research field of ultracold atoms has provided an exciting framework for studying polaronic effects. The key idea is that models designed for describing the rich and non-trivial structure of the solid state, can be emulated in a clean and controllable manner with ultracold atoms. The ongoing experimental developments have sparked off the search for improved numerical methods to obtain a good quantitative understanding of polaronic effects. In this work, we have performed a systematic study of three distinct polaronic systems: the Fermi polaron in three dimensions, the Fermi polaron in two dimensions and the large Bose polaron in three dimensions. In all three situations, we have used the Diagrammatic Monte-Carlo (DiagMC) method to sample a very large number of diagrams and extract the system's "exact" ground-state properties as a function of the interaction strength between the impurity and the bath in the system.

Fermi polaron in three dimensions

We have studied the Fermi-polaron system, in which a single spin-down impurity is strongly coupled to a non-interacting Fermi sea of spin-up particles. To calculate its ground-state properties we have used the Green's function formalism and a series expansion for the physical quantities in terms of Feynman diagrams. The effective interaction between the impurity and spin-up particles has been modeled with a contact potential. This choice leads to ultraviolet divergences when approaching the continuum limit. To overcome this difficulty, a sum over an infinite number of Feynman ladder diagrams has been introduced. This procedure results in a renormalized interaction for which a diagrammatic expansion can be performed in the continuum limit. The first-order diagram of this series and the corresponding ground-state energy can be computed with generally used numerical integration methods. A remarkable property is that the first-order prediction for the energy is identical to the energy obtained

with a one particle-hole (1 p-h) variational calculation.

The evaluation of higher-order contributions to the energy do not necessarily improve the quality of the prediction of the system's energy. The underlying reason for this observation is that the diagrammatic series for a system of strongly interacting fermions does not necessarily converge. In order to obtain reliable results for the system's energy, one has to numerically compute the contribution of high-order diagrams and check explicitly whether an extrapolation to order infinity becomes possible. The evaluation of high-order diagrams can be done with DiagMC. This method is based on the stochastic evaluation of a large series of Feynman diagrams. In order to extract the ground-state properties from the simulations, one has to overcome a factorial complexity connected with the increase of the number of diagrams as one increases the order. Nonetheless, extrapolation to infinite diagram order becomes possible when the diagrams cancel each other better than the factorial increase of the number of diagrams. At the interaction strength $1/(k_F a) = 0$ (with a the scattering length and k_F the Fermi momentum), we observe a situation of perfect cancellations within statistical errors. On the BEC side, the series built with bare propagators gives rise to oscillations with diagram order. As a consequence, a controlled extrapolation to the infinite diagram order is not directly feasible. We have followed two strategies to overcome this complication. First, a reformulation of the problem based on a skeleton series with dressed propagators. Second, the use of resummation techniques. The series expansion with dressed propagators can sometimes be evaluated to higher orders. In some cases, however, the dressing of the propagators destroys a favorable cancellation of diagrams. For all interaction strengths we have observed that the series of the one-body and two-body self-energy is resummable by means of Abelian resummation. We can conclude that the bare series, the skeleton series and resummed series lead to the same result within the error bars.

We have identified classes of dominant diagrams for the one-body and two-body self-energy in the crossover region of strong correlations. The dominant diagrams turn out to be the leading processes of the strong-coupling limit: scattering between a dimer and a spin-up fermion, which is diagrammatically represented by the three-body T-matrix diagrams. Including just these dominant diagrams gives a quantitatively good correction to the lowest order result, even away from the strong-coupling limit.

Our numerical results indicate that for weak to strong attractions, the "exact" polaron and molecule energies agree very well with those from a variational ansatz. A similar observation is made for the polaron's residue or Z-factor. This agreement could be attributed to a strong cancellation of diagrams. Explicit convergence for the bare series is only observed for the $1/(k_F a) = 0$ situation. A full explanation for the success of the variational ansatz is still missing, and it is therefore unclear in which other cases the ansatz is appropriate.

Fermi polaron in two dimensions.

Since the behavior of a quantum system can change drastically by lowering the dimension, we have investigated the properties of a 2D Fermi-polaron system with the DiagMC method. Using a contact potential to model the interaction between the impurity and a spin-up particle, we have faced divergences in the applied formalism. Those divergences can be

removed by introducing a renormalized interaction. Thereby, the two-body binding energy is the relevant parameter to characterize the interaction strength. From our studies it emerges that in 2D the total weight of a given diagram order (i.e. the sum of the absolute values of the contributions of diagrams) is distributed over more types of diagrams than in 3D. Because the sign alternation occurs over a broader distribution of the weights, the statistical noise in sampling the self-energy is significantly larger in 2D compared to 3D. Nevertheless, we succeeded in performing a reliable and accurate extrapolation to infinite diagram order.

The DiagMC method allows one to include a large number of particle-hole excitations that dress the impurity. Truncation of the Hilbert space to a maximum number n of p-h pairs can nonetheless be achieved within the DiagMC approach. This allows us to make a connection with typical variational approaches which are confined to $n = 1$ and $n = 2$.

The quasiparticle properties of the ground state can be studied for a wide range of interaction strengths. A phase transition between the polaron and molecule states is found at interaction strengths compatible with experimental values and with variational predictions. To a remarkable degree, it is observed that for all interaction strengths the full DiagMC results (which include all np-h excitations) for the ground-state properties can be reasonably approximated by $n = 1$ truncations. For the 2D Fermi polaron, the "exact" results are almost equal to the one obtained in a $n = 2$ truncation scheme, although one could have naively expected a large sensitivity to quantum fluctuations.

Large Bose polaron

The BEC polaron and the acoustic polaron are two large polaron systems that can be described by a Fröhlich type of Hamiltonian. The diagrammatic expansion of the Green's function for large polarons can also be evaluated with the DiagMC method. Since all the diagrams have the same sign, we are able to reach a large diagram order (typically $\sim 10^4$). The evaluation of the diagrammatic series up to high orders facilitates the extrapolation to order infinity.

Upon calculating the ground-state energies for the BEC polaron with the DiagMC and the Feynman variational technique, one comes accross ultraviolet divergences. For the acoustic polaron, the ultraviolet regularization is achieved by a hard momentum cutoff which is naturally set at the edge of the first Brillouin zone. In this case, the DiagMC and Feynman predictions for the ground-state energies agree within a few percent. The largest deviation between the predictions of both methods, was found at a coupling strength that marks the transition between a quasi-free and a self-trapped state. For the BEC polaron, a more involving two-step renormalization procedure is required. The first step is the introduction of a hard momentum cutoff. In line with the results for the acoustic polaron, the DiagMC and Feynman non-renormalized ground-state energies of the BEC polaron which are produced in this step are remarkably similar. Therefore, one can infer that the Feynman variational method reproduces the "exact" DiagMC non-renormalized polaron ground-state energies at a finite momentum cutoff.

In order to obtain the physical, or renormalized, BEC-polaron energies from the non-renormalized ones, an additional procedure is required. Thereby, the contact interaction

is renormalized with the aid of the lowest-order correction obtained from the Lippmann-Schwinger equation. Despite the fact that the absolute difference between the Feynman and DiagMC BEC-polaron energies remains unaffected by this procedure, the final result for the physical energies displays a relatively large discrepancy.

Outlook

The first-order result of the bare series for the Fermi polaron is a good approximation for the real ground-state energy. This was due to strong cancellations of higher-order diagrams. Since we have considered equal masses for the impurity and the spin-up fermions, it is not clear that this strong cancellation should also holds for the mass-imbalanced Fermi-polaron. Therefore, further research is needed to inspect the accuracy of the first-order result for mass-imbalanced systems.

We have identified a class of dominant diagrams for the Fermi polaron, the BEC and the acoustic polaron. Taking into account only these diagrams gave in some cases already very good results. The knowledge of dominant diagrams can thus be of great value in the development of approximate schemes.

APPENDIX A

Canonical transformation

Consider the Hamiltonian given in Eq. (1.29):

$$\begin{aligned}\hat{H}_{BP} = &\sum_{\mathbf{p}} \frac{p^2}{2m_I}\hat{c}^\dagger_{\mathbf{p}}\hat{c}_{\mathbf{p}} + n_0 V_{IB}(0) + \frac{1}{2}\mathcal{V}n^2 V_{BB}(0) + \sum_{\mathbf{k}\neq 0}\epsilon_{\mathbf{k}}\hat{a}^\dagger_{\mathbf{k}}\hat{a}_{\mathbf{k}} \\ &+ \frac{n_0}{2}\sum_{\mathbf{k}\neq 0} V_{BB}(\mathbf{k})(\hat{a}^\dagger_{\mathbf{k}}\hat{a}^\dagger_{-\mathbf{k}} + \hat{a}_{\mathbf{k}}\hat{a}_{-\mathbf{k}}) + \sum_{\mathbf{k}\neq 0} n_0(2V_{BB}(\mathbf{k}) - V_{BB}(\mathbf{0}))\hat{a}^\dagger_{\mathbf{k}}\hat{a}_{\mathbf{k}} \\ &+ \frac{\sqrt{N_0}}{\mathcal{V}}\sum_{\mathbf{k}\neq 0,\mathbf{p}} V_{IB}(\mathbf{k})\hat{c}^\dagger_{\mathbf{p}+\mathbf{k}}\hat{c}_{\mathbf{p}}(\hat{a}^\dagger_{-\mathbf{k}} + \hat{a}_{\mathbf{k}}) \,,\end{aligned} \tag{A.1}$$

where we introduced the condensate density $n_0 = N_0/\mathcal{V}$ and the average total density $n = \langle\hat{N}\rangle/\mathcal{V}$. We can diagonalize the bosonic part in Eq. (A.1) by performing the following canonical Bogoliubov transformation:

$$\hat{a}_{\mathbf{k}} = (u_k\hat{b}_{\mathbf{k}} - v_k\hat{b}^\dagger_{-\mathbf{k}}) \tag{A.2}$$

$$\hat{a}^\dagger_{\mathbf{k}} = (u_k\hat{b}^\dagger_{\mathbf{k}} - v_k\hat{b}_{-\mathbf{k}}) \,. \tag{A.3}$$

The coefficients u_k and v_k can be chosen to be real and spherically symmetric. The new operators $\hat{b}_{\mathbf{k}}$ and $\hat{b}^\dagger_{\mathbf{k}}$ fulfill the commutation relations:

$$[\hat{b}_{\mathbf{k}}, \hat{b}^\dagger_{\mathbf{k}'}] = \delta_{\mathbf{k},\mathbf{k}'} \quad \text{and} \quad [\hat{b}_{\mathbf{k}}, \hat{b}_{\mathbf{k}'}] = [\hat{b}^\dagger_{\mathbf{k}}, \hat{b}^\dagger_{\mathbf{k}'}] = 0 \,, \tag{A.4}$$

under the condition that

$$u_k^2 - v_k^2 = 1 \,. \tag{A.5}$$

Substituting the operators given in Eq. (A.2) and (A.3) into (A.1) gives:

$$\begin{aligned}\hat{H}_{BP} = &\sum_{\mathbf{p}} \frac{p^2}{2m_I}\hat{c}^\dagger_{\mathbf{p}}\hat{c}_{\mathbf{p}} + \frac{\mathcal{V}}{2}n^2 g_{BB} + \sum_{\mathbf{k}\neq 0}\left((\epsilon_{\mathbf{k}} + n_0 g_{BB})v_k^2 - n_0 g_{BB}u_k v_k\right) \\ &+ \sum_{\mathbf{k}\neq 0}\left((\epsilon_{\mathbf{k}} + n_0 g_{BB})(u_k^2 + v_k^2) - 2u_k v_k n_0 g_{BB}\right)(\hat{b}^\dagger_{\mathbf{k}}\hat{b}_{\mathbf{k}}) \\ &+ \frac{1}{2}\sum_{\mathbf{k}\neq 0}\left(n_0 g_{BB}(u_k^2 + v_k^2) - (\epsilon_{\mathbf{k}} + n_0 g_{BB})2u_k v_k\right)(\hat{b}^\dagger_{\mathbf{k}}\hat{b}^\dagger_{-\mathbf{k}} + \hat{b}_{\mathbf{k}}\hat{b}_{-\mathbf{k}}) \\ &+ \frac{\sqrt{N_0}g_{IB}}{\mathcal{V}}\sum_{\mathbf{k}\neq 0,\mathbf{p}}\hat{c}^\dagger_{\mathbf{p}+\mathbf{k}}\hat{c}_{\mathbf{p}}(u_k - v_k)(\hat{b}^\dagger_{-\mathbf{k}} + \hat{b}_{\mathbf{k}}) + n_0 g_{IB}\ .\end{aligned} \tag{A.6}$$

We use following pseudo-potentials: $V_{BB}(\mathbf{k}) = g_{BB}$ and $V_{IB}(\mathbf{k}) = g_{IB}$. The bosonic part of Eq. (A.6) is diagonal if

$$n_0 g_{BB}(u_k^2 + v_k^2) - (\epsilon_{\mathbf{k}} + n_0 g_{BB})2u_k v_k = 0\ . \tag{A.7}$$

To solve Eqs. (A.5) and (A.7) for u_k and v_k, we make use of hyperbolic functions,

$$u_k = \cosh(\phi_k) \tag{A.8}$$
$$v_k = \sinh(\phi_k)\ . \tag{A.9}$$

This implies that the following set of equations should be solved:

$$u_k^2 + v_k^2 = \cosh(2\phi_k) \tag{A.10}$$
$$2u_k v_k = \sinh(2\phi_k) \tag{A.11}$$
$$\tanh 2\phi_k = \frac{a}{b}\ . \tag{A.12}$$

with $a = n_0 g_{BB}$ and $b = \epsilon_{\mathbf{k}} + n_0 g_{BB}$. Solving Eq. (A.12) to ϕ_k gives:

$$\phi_k = \frac{1}{2}\text{arctanh}(\gamma)\ , \tag{A.13}$$

with $\gamma = a/b$. Substitute (A.13) in (A.10) and (A.11) and rewrite $\cosh(\text{arctanh}(\gamma))$ as follows:

$$\begin{aligned}\cosh\left(\text{arctanh}(\gamma)\right) &= \frac{1}{2}\left(\sqrt{\frac{1+\gamma}{1-\gamma}} + \frac{1}{\sqrt{\frac{1+\gamma}{1-\gamma}}}\right) \\ &= \left(\frac{1+\gamma}{1-\gamma} + 1\right)\sqrt{\frac{1-\gamma}{1+\gamma}} \\ &= \sqrt{\frac{1}{1-\gamma^2}} \\ &= \cosh 2\phi_k = \frac{b}{\sqrt{b^2 - a^2}}\ .\end{aligned} \tag{A.14}$$

The following relations for hyperbolic functions were used:

$$\operatorname{arctanh}(\gamma) = \frac{1}{2}\ln\left(\frac{1+\gamma}{1-\gamma}\right) \tag{A.15}$$

$$\cosh(\phi_k) = \frac{e^{\phi_k} + e^{-\phi_k}}{2} \,. \tag{A.16}$$

In a similar way we can show that

$$\sinh(2\phi_k) = \sinh(\operatorname{arctanh}(a/b)) = \frac{a}{\sqrt{b^2 - a^2}} \,. \tag{A.17}$$

So we get the following set of equations:

$$u_k^2 + v_k^2 = \frac{b}{\sqrt{b^2 - a^2}} \tag{A.18}$$

$$2u_k v_k = \frac{a}{\sqrt{b^2 - a^2}} \,, \tag{A.19}$$

which can now be solved for the coefficients u_k and v_k:

$$u_k^2 = \frac{1}{2}\left(\frac{b}{\sqrt{b^2 - a^2}} + 1\right) = \frac{1}{2}\left(\frac{\epsilon_{\mathbf{k}} + n_0 g_{BB}}{\omega(\mathbf{k})} + 1\right) \tag{A.20}$$

$$v_k^2 = \frac{1}{2}\left(\frac{b}{\sqrt{b^2 - a^2}} - 1\right) = \frac{1}{2}\left(\frac{\epsilon_{\mathbf{k}} + n_0 g_{BB}}{\omega(\mathbf{k})} - 1\right) \,, \tag{A.21}$$

with $\omega(\mathbf{k}) = \sqrt{(\epsilon_{\mathbf{k}} + n_0 g_{BB})^2 - (n_0 g_{BB})^2}$. The coefficient of the operator part $\hat{b}_{\mathbf{k}}^\dagger \hat{b}_{\mathbf{k}}$ of Eq. (A.6) is

$$\frac{(\epsilon_{\mathbf{k}} + n_0 g_{BB})^2}{\omega(\mathbf{k})} - \frac{(n_0 g_{BB})^2}{\omega(\mathbf{k})} = \omega(\mathbf{k}) \,. \tag{A.22}$$

The coefficient of the boson-impurity operator part becomes:

$$\begin{aligned} \frac{\sqrt{N_0} g_{IB}}{\mathcal{V}}(u_k - v_k) &= \sqrt{N_0} g_{IB} \sqrt{u_k^2 + v_k^2 - 2u_k v_k} \\ &= \frac{\sqrt{N_0} g_{IB}}{\mathcal{V}} \sqrt{\frac{b}{\sqrt{b^2 - a^2}} - \frac{a}{\sqrt{b^2 - a^2}}} \\ &= \frac{\sqrt{N_0} g_{IB}}{\mathcal{V}} \sqrt{\frac{\epsilon_{\mathbf{k}}}{\omega(\mathbf{k})}} \,. \end{aligned} \tag{A.23}$$

With Eqs. (A.18), (A.19) and (A.23), we get for Eq. (A.6)

$$\begin{aligned} \hat{H}_{BP} = &\sum_{\mathbf{p}} \frac{p^2}{2m_I} \hat{c}_{\mathbf{p}}^\dagger \hat{c}_{\mathbf{p}} + \frac{\mathcal{V}}{2} n^2 g_{BB} + \frac{1}{2} \sum_{\mathbf{k} \neq 0} (\omega(\mathbf{k}) - \epsilon_{\mathbf{k}} - n_0 g_{BB}) + \sum_{\mathbf{k} \neq 0} \omega(\mathbf{k}) \hat{b}_{\mathbf{k}}^\dagger \hat{b}_{\mathbf{k}} \\ &+ \frac{\sqrt{N_0} g_{IB}}{\mathcal{V}} \sum_{\mathbf{k} \neq 0, \mathbf{p}} \sqrt{\frac{\epsilon_{\mathbf{k}}}{\omega(\mathbf{k})}} \hat{c}_{\mathbf{p}+\mathbf{k}}^\dagger \hat{c}_{\mathbf{p}} (\hat{b}_{-\mathbf{k}}^\dagger + \hat{b}_{\mathbf{k}}) + n_0 g_{IB} \,. \end{aligned} \tag{A.24}$$

The dispersion $\omega(\mathbf{k})$ can be rewritten with the aid of Eq. (1.31)

$$\begin{aligned}\omega(\mathbf{k}) &= \sqrt{\epsilon_{\mathbf{k}}^2 + 2n_0 g_{BB}\epsilon_{\mathbf{k}}} \\ &= \frac{\sqrt{k^2 4\pi n_0 a_{BB}}}{m_B}\sqrt{\frac{k^2}{2(8\pi n_0 a_{BB})} + 1}\,,\end{aligned} \tag{A.25}$$

with $k = |\mathbf{k}|$. By introducing the healing length of the condensate $\xi = \frac{1}{\sqrt{8\pi n_0 a_{BB}}}$ and the speed of sound in the condensate $c = \frac{\sqrt{4\pi n_0 a_{BB}}}{m_B}$, we get:

$$\omega(\mathbf{k}) = ck\sqrt{1 + (\xi k)^2/2}\,, \tag{A.26}$$

and

$$\begin{aligned}\sqrt{\frac{\epsilon_{\mathbf{k}}}{\omega(\mathbf{k})}} &= \sqrt{\frac{\frac{k^2}{2m_B}}{\sqrt{\left(\frac{k^2}{2m_B}\right)^2 + \frac{2n_0 4\pi a_{BB} k^2}{2m_B^2}}}} \\ &= \sqrt{\frac{\frac{k^2}{2m_B}}{\frac{k}{2m_B\xi}\sqrt{(k\xi)^2 + 2}}} \\ &= \left(\frac{(\xi k)^2}{(\xi k)^2 + 2}\right)^{1/4}.\end{aligned} \tag{A.27}$$

The Hamiltonian $\hat{H}_{BP}$ finally becomes

$$\begin{aligned}\hat{H}_{BP} =& E_0 + n_0 g_{IB} + \sum_{\mathbf{p}} \frac{p^2}{2m_I}\hat{c}_{\mathbf{p}}^\dagger \hat{c}_{\mathbf{p}} + \sum_{\mathbf{k}\neq 0} ck\sqrt{1 + \frac{(\xi k)^2}{2}}\hat{b}_{\mathbf{k}}^\dagger \hat{b}_{\mathbf{k}} \\ &+ \frac{g_{IB}\sqrt{N_0}}{\mathcal{V}} \sum_{\mathbf{k}\neq 0,\mathbf{p}} \left(\frac{(\xi k)^2}{(\xi k)^2 + 2}\right)^{1/4} \hat{c}_{\mathbf{p}+\mathbf{k}}^\dagger \hat{c}_{\mathbf{p}}(\hat{b}_{-\mathbf{k}}^\dagger + \hat{b}_{\mathbf{k}})\,,\end{aligned} \tag{A.28}$$

with

$$E_0 = \frac{\mathcal{V}}{2} n^2 g_{BB} + \frac{1}{2}\sum_{\mathbf{k}\neq 0}(\omega(\mathbf{k}) - \epsilon_{\mathbf{k}} - n_0 g_{BB})\,. \tag{A.29}$$

APPENDIX B

Fourier transform of $\Gamma^0(\mathbf{p}, \Omega)$

- $\int_{-\infty}^{+\infty} \frac{e^{-i\Omega\tau}}{d-\sqrt{-i\Omega+a}} d\Omega$, with $a > 0$ and $\tau > 0$

We consider the integral $\oint_{\mathcal{C}} f(z)dz$, with $\mathcal{C}$ the contour shown in Fig. B.1 with $z_0 = -ia$, and $f(z)$ given by:

$$f(z) = \frac{e^{-iz\tau}}{d - \sqrt{-iz + a}} \,. \tag{B.1}$$

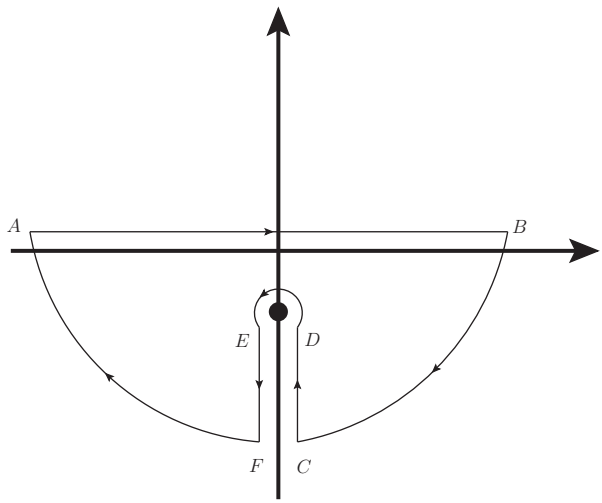

Figure B.1 – The contour $\mathcal{C}$ in the complex plane. The dot represents the point z_0 (see text).

According to the residue theorem, the following relation can be written:

$$\begin{aligned}\oint_{\mathcal{C}} f(z)dz &= \int_A^B f(z)dz + \int_B^C f(z)dz + \int_C^D f(z)dz + \int_D^E f(z)dz \\ &+ \int_E^F f(z)dz + \int_F^A f(z)dz \\ &= -2\pi i \mathrm{Res}\left\{f, z_p\right\} \ ,\end{aligned} \tag{B.2}$$

where $\mathrm{Res}\left\{f, z_p\right\}$ denotes the residue of f at the pole $z_p = i(d^2 - a)$. If $d < 0$ there is no pole. The pole lies in the contour if $d^2 < a$. With the Lemma of Jordan one can show that $\int_B^C f(z)dz = \int_F^A f(z)dz = 0$. It can easily be shown that $\int_D^E f(z)dz = 0$. The expression in Eq. (B.2) can be written as follows:

$$\begin{aligned}\oint_{\mathcal{C}} f(z)dz &= \int_A^B f(z)dz + \int_C^D f(z)dz + \int_E^F f(z)dz \\ &= \int_{-\infty}^{+\infty} f(z)dz + \int_{-i\infty+\eta}^{-ia+\eta} \frac{e^{-iz\tau}}{d - \sqrt{-iz + a}}dz + \int_{-ia-\eta}^{-i\infty-\eta} \frac{e^{-iz\tau}}{d - \sqrt{-iz + a}}dz \ .\end{aligned} \tag{B.3}$$

We substitute $y = iz - i\eta - a$ ($y = iz + i\eta - a$) with η small, in the second (third) integral on the right-hand side of Eq. (B.3),

$$\begin{aligned}&\int_{-i\infty+\eta}^{-ia+\eta} \frac{e^{-iz\tau}}{d - \sqrt{-iz + a}}dz + \int_{-ia-\eta}^{-i\infty-\eta} \frac{e^{-iz\tau}}{d - \sqrt{-iz + a}}dz \\ &= \frac{1}{i}\int_{+\infty}^{0} \frac{e^{(-y-i\eta-a)\tau}}{d - \sqrt{-y - i\eta}}dy + \frac{1}{i}\int_0^{+\infty} \frac{e^{(-y+i\eta-a)\tau}}{d - \sqrt{-y + i\eta}}dy \ .\end{aligned} \tag{B.4}$$

Replacing $-y - i\eta = ue^{-i\pi}$ ($-y + i\eta = ue^{+i\pi}$) in the first (second) term on the right-hand side of Eq. (B.4) yields:

$$\frac{1}{i}\int_{+\infty}^{0} \frac{e^{(-y-i\eta-a)\tau}}{d - \sqrt{-y - i\eta}}dy + \frac{1}{i}\int_0^{+\infty} \frac{e^{(-y+i\eta-a)\tau}}{d - \sqrt{-y + i\eta}}dy = 2e^{-a\tau}\int_0^{+\infty} \frac{\sqrt{u}e^{-u\tau}}{d^2 + u}du \ . \tag{B.5}$$

This integral can be found for example in [35]:

$$2e^{-a\tau}\int_0^{\infty} \frac{\sqrt{u}e^{-u\tau}}{d^2 + u}du = 2\pi e^{-a\tau}\left(\frac{1}{\sqrt{\pi\tau}} + de^{d^2\tau}\left(-1 + \mathrm{erf}(d\sqrt{\tau})\right)\right) \ , \tag{B.6}$$

where erf is the error function. The residue $\mathrm{Res}\left\{f, z_p\right\}$ is given by:

$$\mathrm{Res}\left\{f, z_p\right\} = \lim_{z \to z_p}(z - z_p)f(z) = \begin{cases} \frac{2d}{i}e^{d^2\tau}e^{-a\tau} & \text{if } d^2 < a \text{ and } d > 0 \\ 0 & \text{elsewhere} \end{cases} \ . \tag{B.7}$$

From Eqs. (B.2), (B.6) and (B.7) it follows that:

$$\int_{-\infty}^{+\infty} \frac{e^{-i\Omega\tau}}{d - \sqrt{-i\Omega + a}}d\Omega = -2\pi e^{-a\tau}\left(\frac{1}{\sqrt{\pi\tau}} + de^{d^2\tau}(\mathrm{erfc}(-d\sqrt{\tau}))\right) \ , \tag{B.8}$$

with erfc the complementary error function.

- $\int_{-\infty}^{+\infty} \frac{e^{-i\Omega\tau}}{a-\ln(-i\Omega+b)} d\Omega$, with $b>0$ and $\tau>0$

We consider the integral $\oint_{\mathcal{C}} f(z)dz$, with $\mathcal{C}$ the contour shown in Fig. B.1 with $z_0=-ib$, and $f(z)$ given by:

$$f(z)=\frac{e^{-iz\tau}}{a-\ln(-iz+b)}\ . \tag{B.9}$$

According to the residue theorem, the following relation can be written:

$$\begin{aligned}\oint_{\mathcal{C}} f(z)dz &= \int_A^B f(z)dz+\int_B^C f(z)dz+\int_C^D f(z)dz+\int_D^E f(z)dz\\ &\quad+\int_E^F f(z)dz+\int_F^A f(z)dz\\ &= -2\pi i \mathrm{Res}\left\{f,z_p\right\}\ ,\end{aligned} \tag{B.10}$$

where $\mathrm{Res}\left\{f,z_p\right\}$ denotes the residue at the pole $z_p=i(e^a-b)$. The pole lies in the contour if $e^a<b$. With the Lemma of Jordan one can show that $\int_B^C f(z)dz=\int_F^A f(z)dz=0$. It can easily be shown that $\int_D^E f(z)dz=0$. The expression in Eq. (B.10) can be written as follows:

$$\begin{aligned}\oint_{\mathcal{C}} f(z)dz &= \int_A^B f(z)dz+\int_C^D f(z)dz+\int_E^F f(z)dz\\ &= \int_{-\infty}^{+\infty} f(z)dz+\int_{-i\infty+\eta}^{-ib+\eta}\frac{e^{-iz\tau}}{a-\ln(-iz+b)}dz+\int_{-ib-\eta}^{-i\infty-\eta}\frac{e^{-iz\tau}}{a-\ln(-iz+b)}dz\ .\end{aligned} \tag{B.11}$$

We substitute $y=iz-i\eta-b$ ($y=iz+i\eta-b$) in the second (third) integral on the right-hand side of Eq. (B.11),

$$\begin{aligned}&\int_{-i\infty+\eta}^{-ib+\eta}\frac{e^{-iz\tau}}{a-\ln(-iz+b)}dz+\int_{-ib-\eta}^{-i\infty-\eta}\frac{e^{-iz\tau}}{a-\ln(-iz+b)}dz\\ &=\frac{1}{i}\int_{+\infty}^{0}\frac{e^{(-y-i\eta-b)\tau}}{a-\ln(-y-i\eta)}dy+\frac{1}{i}\int_0^{+\infty}\frac{e^{(-y+i\eta-b)\tau}}{a-\ln(-y+i\eta)}dy\ .\end{aligned} \tag{B.12}$$

Replacing $-y-i\eta=ue^{-i\pi}$ ($-y+i\eta=ue^{+i\pi}$) in the first (second) term on the right-hand side of Eq. (B.12) yields:

$$\frac{1}{i}\int_{+\infty}^{0}\frac{e^{(-y-i\eta-b)\tau}}{a-\ln(-y-i\eta)}dy+\frac{1}{i}\int_0^{+\infty}\frac{e^{(-y+i\eta-b)\tau}}{a-\ln(-y+i\eta)}dy=2\pi e^{-b\tau}\int_0^{+\infty}\frac{e^{-u\tau}}{(a-\ln u)^2+\pi^2}du\ . \tag{B.13}$$

$$\mathrm{Res}\left\{f,z_p\right\}=\lim_{z\to z_p}(z-z_p)f(z)=\begin{cases}-ie^a e^{e^a\tau}e^{-b\tau} & \text{if } e^a<b\\ 0 & \text{elsewhere}\end{cases}\ . \tag{B.14}$$

From Eqs. (B.10), (B.13) and (B.14) it follows that

$$\int_{-\infty}^{+\infty}\frac{e^{-i\Omega\tau}}{a-\ln(-i\Omega+b)}d\Omega=-2\pi e^{-b\tau}\left(\int_0^{+\infty}\frac{e^{-u\tau}}{(a-\ln u)^2+\pi^2}du+e^a e^{e^a\tau}\theta(b-e^a)\right)\ . \tag{B.15}$$

Samenvatting

De laatste jaren is gebleken dat ultrakoude gassen uitermate geschikt zijn om polaron systemen te bestuderen. Modellen die gebruikt worden om de complexe structuur van vaste stoffen te beschrijven kunnen nu ook getest worden in ultrakoude gassen. Deze ultrakoude systemen bieden het voordeel dat ze een hoge mate van flexibiliteit vertonen en ons toelaten een theoretisch model in de meest ideale omstandigheden te testen. Dit stimuleerde de ontwikkeling van steeds betere en nauwkeuriger numerieke methoden. In deze thesis hebben we een systematische theoretische studie gedaan van 3 verschillende polaron systemen: het Fermi polaron in 3 dimensies, het Fermi polaron in 2 dimensies en het grote Bose polaron in drie dimensies. In elk van deze situaties hebben we de diagrammatische Monte Carlo (DiagMC) techniek gebruikt. Deze numerieke techniek laat ons toe om een groot aantal Feynman diagrammen op een stochastische manier te evalueren. Daaruit kunnen dan "exacte" resultaten voor de grondtoestand verkregen worden.

Fermi polaron in drie dimensies

Het Fermi-polaron systeem bestaat uit een onzuiverheidsatoom met een neerwaartse spin dat sterk gekoppeld is aan een Fermi zee van atomen met een opwaartse spin. Om de grondtoestandseigenschappen te berekenen hebben we gebruik gemaakt van het Greense functie formalisme en de bijhorende reeksontwikking van Feynman diagrammen. Om de effectieve interactie te modelleren hebben we gebruik gemaakt van een contact potentiaal. Deze keuze leidt echter tot ultraviolette (UV) divergenties wanneer we de continuümlimiet nemen. Door een oneindige reeks van ladder diagrammen te sommeren kunnen we deze UV divergentie elimineren. Dit leidt tot een gerenormaliseerde interactie en laat ons toe een diagrammatische reeks in de continuümlimiet op te stellen. Het eerste orde diagram en de bijhorende grondtoestandsenergie kan berekend worden met gebruikelijke integratiemethoden. Een merkwaardige eigenschap is dat deze eerste-orde grondtoestandsenergie gelijk is aan de energie komende van een variationele berekening met 1 deeltje-gat excitaties.

In tegenstelling tot wat men zou verwachten, gaan methodes die ook de bijdragen van hogere ordes in rekening brengen niet noodzakelijk leiden tot een betere voorspelling van de energie. De reden is dat de diagrammatische reeks van een systeem van sterk interagerende fermionen niet noodzakelijk convergeert. Betrouwbare waarden voor de energie kunnen echter

wel verkregen worden door deze hogere orde contributies te extrapoleren naar orde oneindig. De DiagMC techniek laat toe om Feynman diagrammen tot op hoge orde uit te rekenen. Een extrapolatie naar orde oneindig wordt mogelijk als diagrammen met een wisselend teken elkaar in grote mate gaan opheffen, ondanks het feit dat het aantal diagrammen stijgt als een faculteit. Voor de interactiesterkte $1/(k_F a) = 0$ (hier bij is k_F het Fermi momentum en a de verstrooiingslengte) nemen we binnen de ruis geen signaal meer waar als we diagrammen met een wisselend teken sommeren bij hoge orde. Aan de BEC zijde nemen we oscillaties met de orde waar in de reeks met niet-aangeklede propagatoren. Hierdoor is een extrapolatie naar oneindige diagram ordes niet vanzelfsprekend. In eerste instantie hebben we dit probleem opgelost door de propagatoren aan te kleden. Omdat dit niet altijd leidde tot convergentie, hebben we aangetoond hoe hersommatie methodes aangewend worden om de reeks te sommeren. De reeks met aangeklede propagatoren heeft het voordeel dat we soms hogere ordes kunnen bereiken. Een nadeel van deze reeks is dat in sommige gevallen diagrammen met een wisselend teken elkaar minder gaan opheffen. De reeks van de één-deeltjes en de twee-deeltjes zelf-energie is hersommeerbaar met behulp van abelse hersommatie methodes voor alle interactiesterktes. Waar de extrapolatie naar orde oneindig controleerbaar is, hebben we aangetoond dat de niet-aangeklede reeks, de skelet reeks en de gehersommeerde reeks allen betrouwbare resultaten geven.

Voor de één-deeltjes en twee-deeltjes zelf-energie hebben we voor sterke interacties een klasse van dominante diagrammen gevonden. Deze dominante diagrammen maken deel uit van de drie-deeltjes T-matrix. Hieruit leiden we af dat in het gebied van sterke koppeling de verstrooiing van een molecule aan een fermion met opwaartse spin een belangrijk fysisch proces is. Wanneer men enkel deze dominante diagrammen in rekening brengt, krijgt men al een goede schatting van het eerste orde resultaat.

Onze numerieke resultaten voor de polaron en molecule energie, voor zwakke en sterke interacties, vertonen een opvallende overeenkomst met resultaten die bekomen werden uit variationele berekeningen. Voor het residue van het polaron vinden we eveneens een goede overeenkomst. Mogelijks komt dit door het feit dat diagrammen met een wisselend teken elkaar gaan opheffen. Volledige convergentie voor de niet-aangeklede reeks zien we enkel bij $1/(k_F a) = 0$. Een volledige verklaring voor het succes van deze variationele methode kan voorlopig nog niet gegeven worden. Het is daardoor ook niet mogelijk om te voorspellen in welke situaties deze variationele methode goede resultaten zal geven.

Fermi polaron in twee dimensies

Het gedrag van een kwantum systeem is sterk afhankelijk van de dimensie. Dit maakt het interessant om het Fermi polaron in twee dimensies te bestuderen met de DiagMC methode. Om de interactie tussen de onzuiverheid en een fermion met opwaartse spin te modelleren hebben we gebruik gemaakt van een contact potentiaal. Deze keuze leidt echter tot divergenties. Door het introduceren van een gerenormaliseerde interactie kunnen we deze divergenties wegwerken. De twee-deeltjes bindingsenergie is nu de relevante parameter die de interactiesterkte beschrijft. Uit onze studie blijkt dat in twee dimensies het totale gewicht van alle diagrammen van een bepaalde orde (dus de som van de absolute bijdragen van de

diagrammen) over meer verschillende types van diagrammen verdeeld is dan in drie dimensies. Dit leidt ertoe dat we meer diagrammen die een bijna zelfde gewicht en een wisselend teken hebben, gaan sommeren. Hierdoor zien we dat de statistische ruis in 2D groter is dan in 3D. Desondanks, is het nog steeds mogelijk om een betrouwbare extrapolatie naar orde oneindig te maken.

De DiagMC methode laat toe om een groot aantal deeltje-gat excitaties in rekening te brengen. De Hilbert ruimte kan met DiagMC ook beperkt worden tot een maximum van n deeltje-gat excitaties. Dit laat ons toe om een connectie te maken met een variationele berekening voor $n = 1$ of $n = 2$ deeltje-gat excitaties.

We hebben de eigenschappen van de grondtoestand voor het Fermi polaron bestudeerd voor verschillende interactiesterktes. We vinden dat de faseovergang plaatsvindt bij een interactiesterkte die vergelijkbaar is met experimentele waarden en met variationele voorspellingen. Een merkwaardige vaststelling is dat een $n = 1$ benadering voor alle interactiesterktes reeds een goed resultaat geeft. Voor het 2D Fermi polaron liggen de "exacte" resultaten zeer dicht bij de resultaten van een $n = 2$ benadering. Dit is merkwaardig, men kan verwachten dat er in 2 dimensies door de toename van kwantum fluctuaties, een groter aantal deeltje-gat excitaties in rekening moet gebracht worden.

Groot Bose polaron

Het BEC polaron en het akoestisch polaron zijn twee grote polaron systemen die door een Fröhlich type van Hamiltoniaan kunnen beschreven worden. Voor grote polaronen kunnen we ook een diagrammatische reeks voor de Greense functie opstellen. Doordat alle diagrammen hetzelfde teken hebben kunnen we met de DiagMC techniek heel hoge ordes bereiken (typische ordes zijn $\sim 10^4$). Bij het berekenen van de energie van de grondtoestand van het BEC polaron stoten we op UV divergenties. Voor het akoestisch polaron kunnen deze divergenties geregulariseerd worden door een bovenlimiet voor de impuls in te voeren. Deze bovenlimiet komt overeen met de rand van de eerste Brillouin zone. Voor dit systeem zien we dat de DiagMC resultaten maar een paar procent verschillen van de Feynman resultaten. De grootste afwijking was gevonden voor de koppeling sterkte waarbij het systeem een transitie tussen een quasi-vrije toestand en een zelf-gevangen toestand ondergaat.

Onze renormalisatie procedure voor het BEC polaron gebeurt in twee stappen. De eerste stap is het opleggen van een bovenlimiet voor de impulsen. De DiagMC resultaten die hierna bekomen worden, vertonen eveneens een grote gelijkenis met de Feynman resultaten. In deze fase kunnen we besluiten dat de Feynman variationele methode bijna de "exacte" niet-gerenormaliseerde DiagMC energie van de grondtoestand produceert.

In de tweede stap berekenen we de fysische of gerenormaliseerde BEC polaron energieën uit de niet-gerenormaliseerde. Hiertoe wordt de contact interactie gerenormaliseerd met behulp van de laagste orde correctie uit de Lippmann-Schwinger vergelijking. Ondanks het feit dat het absolute verschil tussen de Feynman en de DiagMC resultaten hierdoor niet verandert, vertoont het finale resultaat van beide methoden een vrij groot vershil.

Bibliography

[1] R. D. Mattuck, *A guide to Feynman diagrams in the many-body problem.* Dover Publications; 2 edition, (1992).

[2] E. Lifshitz and L. P. Pitaevskii, *Statistical physics Part 2.* Course of Theoretical Physics Vol. 9 (Book 2). Butterworth-Heinemann, 1980.

[3] A. Abrikosov, L. Gorkov, and I. Dzyaloshinski, *Methods of quantum field theory in statistical physics.* Dover, New York, N.Y., 1963.

[4] A. L. Fetter, J. D. Walecka, and Physics, *Quantum Theory of Many-Particle Systems (Dover Books on Physics).* Dover Publications, 2003.

[5] C. Kittel, *Introduction to Solid State Physics.* John Wiley & Sons, Inc., New York, 6th ed., 1986.

[6] C. Lobo, A. Recati, S. Giorgini, and S. Stringari, *Normal State of a Polarized Fermi Gas at Unitarity.* *Phys. Rev. Lett.* **97** (2006) 200403.

[7] S. Pilati and S. Giorgini, *Phase Separation in a Polarized Fermi Gas at Zero Temperature.* *Phys. Rev. Lett.* **100** (2008) 030401.

[8] H. Fröhlich, *Electrons in lattice fields.* *Advances in Physics* **3** (1954) 325–361.

[9] J. Devreese, *Polarons.* *Encycl. Appl. Phys.* **14** (1996) 383–409.

[10] M. H. Anderson, J. R. Ensher, M. R. Matthews, C. E. Wieman, and E. A. Cornell, *Observation of Bose-Einstein Condensation in a Dilute Atomic Vapor.* *Science* **269** (1995) 198–201.

[11] K. B. Davis, M. O. Mewes, M. R. Andrews, N. J. van Druten, D. S. Durfee, D. M. Kurn, and W. Ketterle, *Bose-Einstein Condensation in a Gas of Sodium Atoms.* *Phys. Rev. Lett.* **75** (1995) 3969–3973.

[12] C. C. Bradley, C. A. Sackett, J. J. Tollett, and R. G. Hulet, *Evidence of Bose-Einstein Condensation in an Atomic Gas with Attractive Interactions*. *Phys. Rev. Lett.* **75** (1995) 1687–1690.

[13] I. Bloch, J. Dalibard, and S. Nascimbène, *Quantum simulations with ultracold quantum gases*. *Nature Physics* **8** (2012) 267–276.

[14] C. Chin, R. Grimm, P. Julienne, and E. Tiesinga, *Feshbach resonances in ultracold gases*. *Rev. Mod. Phys.* **82** (2010) 1225–1286.

[15] W. Zwerger, *The BCS-BEC crossover and the unitary Fermi gas*, vol. 836. Springer, 2011.

[16] A. Schirotzek, C.-H. Wu, A. Sommer, and M. W. Zwierlein, *Observation of Fermi Polarons in a Tunable Fermi Liquid of Ultracold Atoms*. *Phys. Rev. Lett.* **102** (2009) 230402.

[17] J. J. Sakurai, *Modern Quantum Mechanics (Revised Edition)*. Addison Wesley, 1 ed., 1993.

[18] Y. Castin, *Simple theoretical tools for low dimension Bose gases*. *J. Phys. IV France* **116** (2004) 89–132.

[19] C. Pethick and H. Smith, *Bose-Einstein Condensation in Dilute Gases*. Cambridge University Press, 2008.

[20] B. DeMarco, J. L. Bohn, J. P. Burke, M. Holland, and D. S. Jin, *Measurement of p-Wave Threshold Law Using Evaporatively Cooled Fermionic Atoms*. *Phys. Rev. Lett.* **82** (1999) 4208–4211.

[21] W. H. Dickhoff and D. Van Neck, *Many-body theory exposed!* World Scientific, 2008.

[22] N. V. Prokof'ev and B. V. Svistunov, *Bold diagrammatic Monte Carlo: A generic sign-problem tolerant technique for polaron models and possibly interacting many-body problems*. *Phys. Rev. B* **77** (2008) 125101.

[23] F. Chevy, *Universal phase diagram of a strongly interacting Fermi gas with unbalanced spin populations*. *Phys. Rev. A* **74** (2006) 063628.

[24] R. Combescot, A. Recati, C. Lobo, and F. Chevy, *Normal State of Highly Polarized Fermi Gases: Simple Many-Body Approaches*. *Phys. Rev. Lett.* **98** (2007) 180402.

[25] J. Thijssen, *Computational Physics*. Cambridge University Press, 2 ed., 2007.

[26] N. Prokof'ev and B. Svistunov, *Fermi-polaron problem: Diagrammatic Monte Carlo method for divergent sign-alternating series*. *Phys. Rev. B* **77** (2008) 020408.

[27] D. Landau and K. Binder, *A Guide to Monte Carlo Simulations in Statistical Physics*. Cambridge University Press, Cambridge, 2005.

[28] J. Vlietinck, J. Ryckebusch, and K. Van Houcke, *Quasiparticle properties of an impurity in a Fermi gas*. *Phys. Rev. B* **87** (2013) 115133.

[29] E. V. H. Doggen and J. J. Kinnunen, *Energy and Contact of the One-Dimensional Fermi Polaron at Zero and Finite Temperature*. *Phys. Rev. Lett.* **111** (2013) 025302.

[30] J. McGuire, *Interacting fermions in one dimension. II. Attractive potential*. *Journal of Mathematical Physics* **7** (1966) 123–132.

[31] J. Vlietinck, J. Ryckebusch, and K. Van Houcke, *Diagrammatic Monte Carlo study of the Fermi polaron in two dimensions*. *Phys. Rev. B* **89** (2014) 085119.

[32] A. S. Mishchenko, N. V. Prokof'ev, A. Sakamoto, and B. V. Svistunov, *Diagrammatic quantum Monte Carlo study of the Fröhlich polaron*. *Phys. Rev. B* **62** (2000) 6317–6336.

[33] N. V. Prokof'ev and B. V. Svistunov, *Polaron Problem by Diagrammatic Quantum Monte Carlo*. *Phys. Rev. Lett.* **81** (1998) 2514–2517.

[34] J. Vlietinck, W. Casteels, K. Van Houcke, J. Tempere, J. Ryckebusch, and J. T. Devreese, *Diagrammatic Monte Carlo study of the acoustic and the BEC polaron*. arXiv:1406.6506.

[35] I. S. Gradshteyn and I. M. Ryzhik, *Table of Integrals, Series, and Products, Fifth Edition*. Academic Press, 5th ed., 1994.